ADVANCED SUBSTRATE DESIGN FOR LABEL-FREE DETECTION OF TRACE ORGANIC AND BIOLOGICAL MOLECULES

A Dissertation
Presented to
The Academic Faculty

by

Zachary Allen Combs

In Partial Fulfillment
of the Requirements for the Degree
Doctor of Philosophy in the
School of Materials Science and Engineering

Georgia Institute of Technology
December 2013

ADVANCED SUBSTRATE DESIGN FOR LABEL-FREE DETECTION OF TRACE ORGANIC AND BIOLOGICAL MOLECULES

Approved by:

Dr. Vladimir V. Tsukruk, Advisor
School of Materials Science and Engineering
Georgia Institute of Technology

Dr. Dong Qin
School of Materials Science and Engineering
Georgia Institute of Technology

Dr. Zhiqun Lin
School of Materials Science and Engineering
Georgia Institute of Technology

Dr. Mostafa A. El-Sayed
School of Chemistry and Biochemistry
Georgia Institute of Technology

Dr. Valeria Milam
School of Materials Science and Engineering
Georgia Institute of Technology

Date Approved: October 28, 2013

Dedicated to my loving family

ACKNOWLEDGEMENTS

Prof. Vladimir Tsukruk gave me the valuable opportunity to join his research group in the field of surface engineering and I cannot thank him enough for being compassionate and generous throughout these years. He nurtured curiosity, inspired creativity, and fostered the desire in me towards achieving my goal. His advice and influence allowed me to win the prestigious National Defense Science and Engineering Fellowship and every day since has been a learning experience and I will cherish these memories for the rest of my life. I would also like to thank Prof. Mostafa El-Sayed, Prof. Zhiqun Lin, Prof. Dong Qin, and Prof. Valeria Milam for their helpful feedback, suggestions, and kind willingness to be a part of my dissertation committee.

Our collaborators played a critical role in this work through insight from external disciplines. In particular, I would like to thank Dr. Mahmoud Mahmoud and Prof. Mostafa El-Sayed for their significant contribution in nanostructure synthesis. Also, I would like thank Dr. Jorge Chávez and Dr. Nancy Kelley-Loughnane for their expertise in biochemistry. Finally, much appreciation is given to Dr. Theodoros Papadopoulos, Dr. Hong Li, Prof. Jean-Luc Brédas, Dr. Jian Wang, and Dr. Richard Brown for their help in electromagnetic and chemical simulations.

It is only because of the supportive nature of the SEMA lab members that my PhD tenure has been a memorable one. Particularly, I would like to thank Dr. Sehoon Chang, Dr. Dhaval Kulkarni, and Dr. Rajesh Kodiyath for their constant support and guidance. I would like to especially thank Dr. Sehoon Chang for his support and guidance during the initial years of my PhD. I would also like to thank current and former SEMA lab members, Dr. Ikjun Choi, Dr. Tobias König, Dr. Kyle Anderson, Sidney Malak, and Richard Davis for their support.

TABLE OF CONTENTS

LIST OF TABLES

LIST OF FIGURES

SUMMARY

To truly realize and exploit the extremely powerful information given from surface-enhanced Raman scattering (SERS) spectroscopy, it is critical to develop an understanding of how to design highly sensitive and selective substrates, produce specific and label-free spectra of target analytes, and fabricate long-lasting and in-the-field ready platforms for trace detection applications. The study presented in this dissertation investigated the application of two- and three-dimensional substrates composed of highly-ordered metal nanostructures. These systems were designed to specifically detect target analytes that would enable the trace, label-free, and real-time detection of chemicals and biomolecules. This study was also designed to provide details regarding the interactions of such molecules at the interfaces of nanostructure assemblies which will help in improving the reliability, understanding, and possible future application of Raman spectroscopy in the fields of chemical, environmental, and biological sensing. Specifically, the uniqueness of this study can be summarized through the following novel findings, fabrication processes, and characterization techniques:

- New insight into the required properties for maximizing electromagnetic Raman enhancement in three-dimensional porous alumina substrates by designing metal nanostructure shape, density, aggregated state, and most importantly aligning the substrate pore size with the excitation wavelength used for plasmonic enhancement.

- Development of design principles of noble metal nanostructures such as composition, exposed facets, and capping agents and how these characteristics can affect chemical enhancement in three-dimensional Raman substrates and can lead to record enhancement factors.

- A new micropatterned silver nanoparticle substrate fabricated via soft lithography with specific functionalization which allows the simultaneous analyte and background detection for trace concentrations of the target biomolecule, immunoglobulin G.

- A novel functionalized SERS hot spot fabrication technique which utilizes highly specific aptamers as both the mediator for electrostatic assembly of gold nanoframe dimers as well as the biorecognition element for the target, riboflavin, to properly locate the tethered biomolecule within the enhanced region for trace detection.

We suggest that the understanding of SERS phenomena that occur at the interface of nanostructures and target molecules combined with the active functionalization and organization of metal nanostructures and trace detection of analytes discussed in this study can provide important insight for addressing some of the challenges facing the field of SERS sensor design such as high sensitivity and selectivity, reliable and repeatable label-free identification of spectral peaks, and the well-controlled assembly of functional metal nanostructures. This research will have a direct impact on the future application of SERS sensors for the trace detection of target species in chemical, environmental, and biomedical fields through the development of specific design criteria and fabrication processes.

CHAPTER 1

INTRODUCTION

1.1 Background

Developments in sensing devices and methods have grown widely and quickly over the past few decades as a result of advances in technologies across many fields. One of the most progressive and important areas of advance has been in biological detection systems. Advances in the detection accuracy and quantity are needed for the early detection of biomarkers related to both long-term disease monitoring and in-the-field detection scenarios where fast and accurate detection is required. The demand for a robust method of fast, selective, sensitive, and multiplexed detection of biomarkers has become extremely high to meet the needs of the fast growing field of biosensing for health and bioenvironmental monitoring.[1] Many different techniques have been developed and are currently being used to detect biological species which include fluorescence-, mass-, and colorimetric-based assays. Common biological detection methods such as enzyme-linked immunosorbent assays (ELISA), surface plasmon resonance (SPR) techniques, or fluorescence resonance energy transfer (FRET) often require complicated and time-consuming sample preparation such as labeling and provide only indirect qualitative measurements of the bioanalyte of interest.[2] On the other hand, there are very few detection methods that can provide a unique chemical signature for the target biomolecule that will allow for its specific and trace detection. Raman spectroscopy in its enhancement mode, shows promises as a tool for the label-free detection of biomolecules in minute quantities.[3,4]

In particular, Raman spectroscopy may be useful for sensitive, miniature, *in-vitro*, and multiplexing bio-hybrid microsensor arrays that are of considerable interest for the next generation of intelligence, reconnaissance, and surveillance devices. Raman spectroscopy may also provide a pathway for rapid, continuous, real-time monitoring of the cognitive function, state of fatigue, and environmental exposure of individuals in harzardous or stressful conditions, such as warfighters, pilots, and air traffic controllers, who are required to make sound decisions under pressure. The important transition between need and design is the in-depth understanding of fundamental concepts related to the nanoscale chemical and physical phenomena utilized in the biodetection mechanism. Therefore, the investigation of the ***fundamental principles and issues*** related to developing effective biomolecular sensors utilizing Raman spectroscopy as the detection mechanism, in particular those utilizing selective molecules for the targeted detection of biomarkers, are of primary importance.

1.1.1 Common methods for molecular sensing

Molecular detection and identification is a critically important issue for the fields of analytical chemistry, polymer chemistry, and medicine and there have been a myriad of techniques developed in these fields. For the direct identification of chemical functional groups and elemental composition of solution-based molecular samples (polymers, small organic species, biomolecules) techniques such as nuclear magnetic resonance (NMR) spectroscopy, mass spectroscopy, and FTIR are typically used.

Nuclear magnetic resonance is one of the most powerful techniques for determining the composition and stereochemical configuration of macromolecules including polymers and biomolecules.[5] In fact, in the field of biology, NMR has been the dominant method for determining protein structure and function because it allows the three-dimensional determination of the protein structure in solution as it would behave in a physiological environment.[6,7] Mass spectroscopy is another powerful tool for molecular identification through the determination of ions in the gas phase formed through ionization or fragmentation and has found broader applications in more advanced modes such as matrix-assisted laser desorption ionization (MALDI) which can transfer larger molecular ions with less fragmentation.[5,8] In the field of proteomics, mass spectroscopy has been used to study signaling pathways, protein and nucleic acid interactions, and substrate interactions, as well as basic biomolecule identification.[9]

Fourier transform infrared spectroscopy (FTIR) spectra are obtained by monitoring the absorption of electromagnetic radiation (infrared) and the subsequent conversion of this absorbed radiation into specific molecular motions that are determined by the functional group and binding state of the chemical species.[5] FTIR has also been used quite extensively in the field of biology for protein identification and secondary structure determination; however, great care must be taken to ensure the results are physiologically relevant.[10,11] The related vibrational spectroscopic technique, Raman spectroscopy, is the key characterization tool used in this work and is discussed separately in greater detail in following sections.

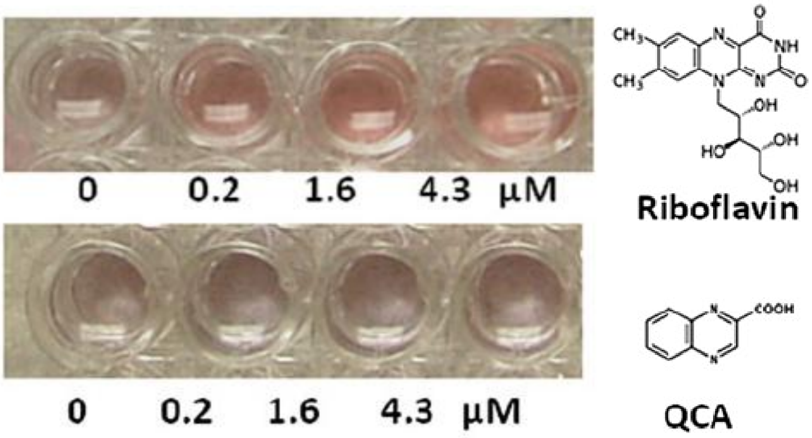

Figure 1.1 Visual colorimetric assay for the detection multiple analytes using functionalized gold nanoparticles.[15]

These approaches allow for a lab-based identification of molecules, but for more simplified and clinical-type applications, colorimetric and fluorescent based sensors are more commonly used. These approaches provide a simple readout that can be quantitative or qualitative for ease of interpretation and therefore these sensing platforms have found a great deal of application in biosensors.[12] In fact, many colorimetric assays utilize gold and silver nanoparticles as the color changing mechanism.[13,14] One example is the detection of the biomolecule riboflavin using aptamer-functionalized gold nanoparticles in solution.[15] Depending on the aptamer length and the binding condition of the analyte, the color as read by the eye or quantitatively using a spectrophotometer will change due to aggregation of the gold nanoparticles (Figure 1.1). Fluorescent immunoassays are also commonly used for the detection of biomolecules as has been demonstrated with neuropeptides as well as DNA detection.[16,17] These techniques will be described in more detail in subsequent sections. Although colorimetric and fluorescent based methods provide a simple readout, they rely on the secondary reaction of a reporter molecule or nanostructure leading to the higher possibility of false positives and inaccurate concentration readings.

1.1.2 Surface-enhanced Raman scattering

Raman spectroscopy has been shown to be an extremely useful technique for bioanalyte detection.[18] Although normal Raman spectroscopy offers a wealth of information, it has generally been disregarded as a trace-detection analytical tool due to the very low scattering cross-section.[19] Without the presence of resonances, the differential Raman cross-sections are less than 10^{-29} cm^2 sr^{-1}, i.e., more than 10 orders of magnitude lower than that of ordinary fluorescence. In order to overcome this deficiency in signal intensity, surface-enhanced Raman scattering (SERS) is utilized because it can provide up to 14 orders of magnitude in signal enhancement.[20] Since its discovery in the late

1970s, SERS has emerged as a powerful tool for sensitive chemical analysis down to the single-molecule level.[20,21,22]

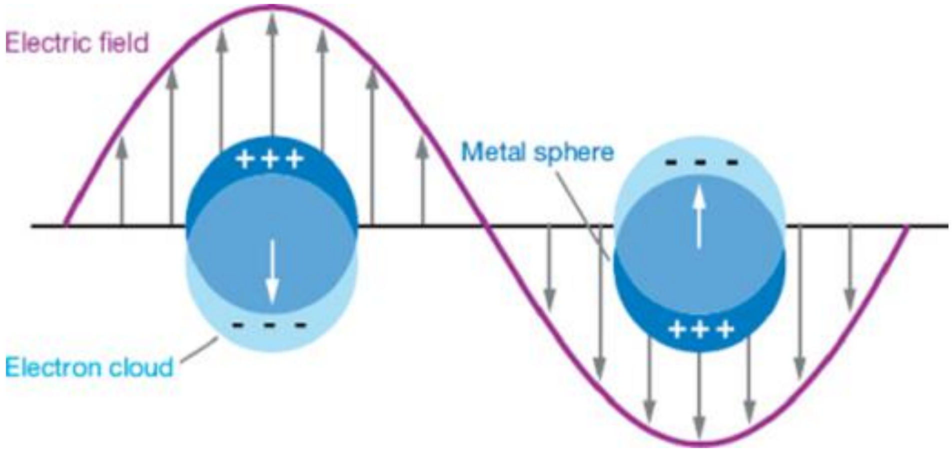

Figure 1.2 Localized surface plasmons of metal spheres with displacement of the electron charge cloud relative to the nuclei.[23]

The SERS enhancement phenomenon is a result of contributions from electromagnetic and chemical enhancments. As known, when metallic nanostructures are exposed to an electromagnetic field, several excitation events can occur such as dipole plasmons, multipole excitaitons, and interband transitions. Dipole plasmon excitation, caused by the oscilating conductive electrons resulting from the ac electric field of the incident light source, is the dominant source of excitation in metal nanoparticles (Figure 1.2).[23,24,25] There are several factors that influence the plasmon resonance of metal nanostructures and subsequently the electromagnetic portion of the overall SERS enhancement including the density of electrons, interactions with other nanoparticles and their shape, and the dielectric ambient.[26] The surface plasmon enhancement effect is a highly localized phenomenon that occurs when the analyte is within 2-5 nm of the particle and then diminishes quickly with increased distance.[27]

The optimal size for metal nanoparticles to exhibit "near-field" enhancement is 10-80 nm and this effect decays over a distance on the order of the size of the nanoparticle.[28,29,30,31,32] It is possible to tune the surface plasmon resonance of the nanoparticles by adjusting their size, shape, and composition in order to achieve maximum interaction with the excitation source.[33,34] For nanoparticle aggregates, plasmon coupling produces a further increased electromagnetic field at longer wavelengths at particle junctions ("hot spots"). It has been shown that up to 50% of overall Raman enhancement is the result of only 1% of total analyte concentration when that small fraction of analyte is located at hot spot junctions using substrates containing silver nanostructures.[35]

The greatest degree of Raman enhancement has been shown to occur between the wavelength of the excitation source and the wavelength of the Raman band of the analyte.[36] Figure 1.3 shows the relationship between the surface plasmon band of the metal nanostructure and the wavelength of the excitation laser for maximum SERS ehancement. It is predicted that the maximum SERS enhancement occurs when the λ_{LSPR} (absorption peak) of the metal nanostructures lies between the λ_{ex} (excitation wavelength) and λ_{vib} (particular vibrational band of the analyte molecule, in this case correlating to 1360-1644 cm^{-1} for Rhodamine 6G (R6G) and 1356-1587 cm^{-1} for the bioanalyte riboflavin).[36]

$$\Delta\nu_{\mathrm{vac}} = \nu_{\mathrm{vac}} + \delta - \frac{1}{\lambda_{\mathrm{air}}} \qquad \text{(Eq. 1)}$$

$$\lambda_{\mathrm{LSPR}} \approx \lambda_{\mathrm{ex}} + \frac{\lambda_{\mathrm{vib}} - \lambda_{\mathrm{ex}}}{3} \qquad \text{(Eq. 2)}$$

The vibrational wavelength of the analyte peak range (λ_{air}) can be calculated from Eq. 1, where $\Delta\nu_{vac}$ is the Raman peak location, ν_{vac} is the wavenumber of the excitation laser source, and δ is the correction factor. The correction factor is ignored in our calculations because it is on the same order (~5 cm^{-1}) of the error associated with the grating (600g/mm) of our Raman system and the correction factor does not significantly contribute to the Raman peak location of the analyte.

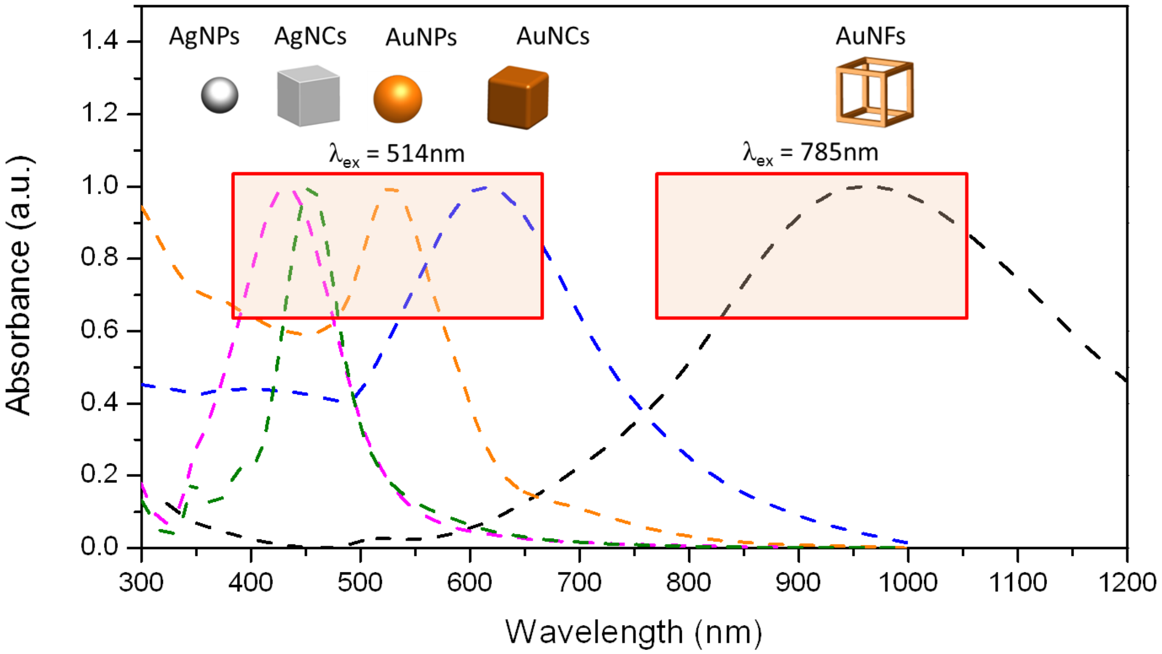

Figure 1.3 Plasmonic behavior of nanostructures with different shapes and compositions and the corresponding excitation source that is appropriate for a particular pairing of nanostructure and target molecule. The UV-Vis-NIR spectra of silver nanospheres, silver nanocubes, gold nanospheres, gold nanocubes, and gold nanoframes are shown.

In this study, we have adopted a useful expression (Eq. 2) which allows for the estimation of the necessary location for the plasmon resonance band peak (λ_{LSPR}) of the metallic nanostructures of the SERS substrate. This equation is based on previous experimental results of our group as well as literature values, which show that the λ_{LSPR} needs to be located approximately 1/3 of the distance between the excitation wavelength and the wavelength associated with the Raman peak of the analyte.[36] Therefore, silver nanoparticles assembled in PAMs (λ_{LSPR} =450-550 nm) show strong SERS enhancement from R6G molecules. This also means that when using an excitation wavelength of 785 nm, gold nanoframe hot spots are appropriate as they show a λ_{LSPR} range from 750 to 1050 nm, thus the resulting SERS enhancement can still be advantageous for riboflavin molecules. This equation provides the necessary background information needed to intelligently guide experiments to practically achieve optimal electromagnetic SERS enhancement of each specific analyte.

The second contribution to the overall Raman enhancement is the chemical enhancement which typically contributes up to 3 order of magnitude,[37] although some studies predict it to be as high as 10^5-10^7.[38,39,40] Chemical enhancement occurs due to the binding of analyte molecules on the metal nanoparticle surface and the consequent overlap between the metal and adsorbate wavefunctions.[41] Chemical enhancement is considered to be a combination of three main phenomena, namely the charge transfer,[42] molecular resonances,[43] and non-resonant interactions.[44]

The charge transfer and molecular resonance mechanisms arise when the incident radiation is in resonance with the molecule-metal charge transfer and the electronic transition in the molecule. These mechanisms provide major contributions toward the total enhancement of up to 10^6 for highly resonant analytes such as rhodamine 6G and other fluorophores. The non-resonant chemical mechanism occurs due to the interaction between the molecule and the metal surface, giving rise to enhancements of 10-10^2.[42]

However, the specific underlying mechanisms of chemical enhancement for complex biomolecules are not well understood.

1.1.3 Biological detection techniques

In medical diagnostics, other methods for the detection of biomoelcules have been used due to the simplicity of the output data such as enzyme-linked immunosorbent assays (ELISA), blotting techniques, surface plasmon resonance (SPR), and fluorescence resonance energy transfer (FRET). However, the key drawbacks of many of these detection techniques are their modest limit of detection and selectivity for the analyte, necessity for complex labeling steps, and the possible occurrence of false positives in complex fluids due to non-specific interactions. ELISA is one of the most commonly used techniques for biomolecule detection since its development in 1971.[45] This technique functions as a result of measuring the fluorescent signal of a labeled molecule that is either coupled or separated from a target leading to the ability to measure bound or free activity of biomolecules.[46] This makes this a highly-used method in the field of proteomics; however, drawbacks include the reliance on a labeled molecule and a secondary reaction for detection.[47]

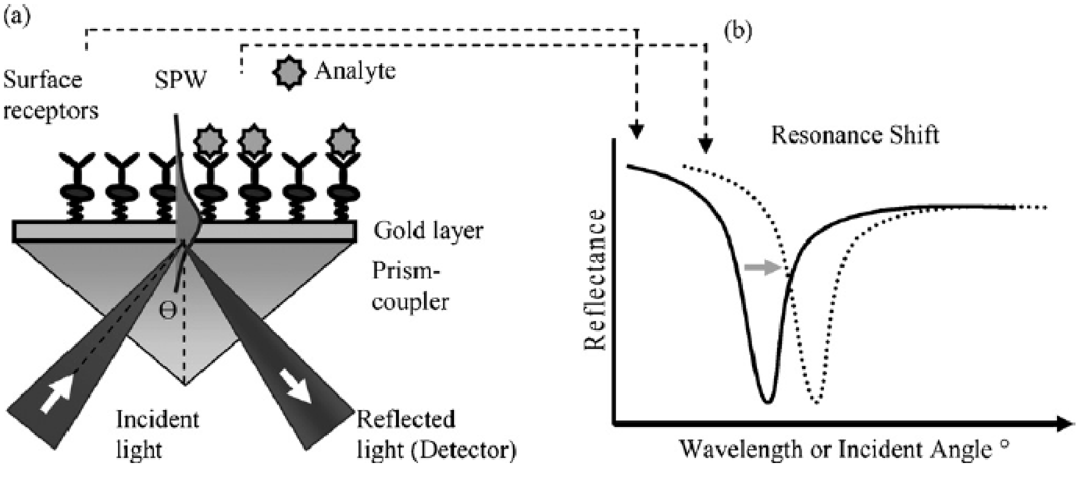

Figure 1.4 Tracking surface absorption by SPR (a) prism-coupled configuration and (b) resonance shift in the reflected light spectrum.[54]

Another common technique for identifying and separating proteins is through gel electrophoresis which utilizes a potential across a cross-linked polymer gel matrix to separate proteins based on their size, shape, and charge density.[48] This technique can also be applied to other biomolecules such as DNA for sizing.[49] Surface plasmon resonance was first demonstrated as a method for gas and biological sensing in the early 1980's and has since seen widespread growth and attention particularly related to binding characteristics and kinetics of biomolecules.[50,51,52] Surface plasmon waves in plasmonic materials are predominantly concentrated directly above the sensing surface and therefore are extremely sensitive to changes in the refractive index of this region. This means that when the surface is functionalized with biorecognition elements, the capture of an analyte from solution can be seen as an increase in the refractive index and detected by an SPR device with high sensitivity of down to nano and picograms of material (Figure 1.4).[53,54]

Another technique that is used to monitor the interaction of different biomolecules is fluorescence resonance energy transfer (FRET), which utilizes the energy transfer phenomenon of closely situated fluorophores or nanostructures to detect molecular binding.[55] Unlike typical fluorescent methods that can depend on probe concentration and environment, FRET can use varying ratios of fluorescent probes to simultaneously monitor fluorescent excitation/emission intensities at two different wavelengths, which means the ratios will not be affected by the environment.[56] However, all of these methods have limitations that will be described in more detail in subsequent sections including the need for labeling, time-consuming processing, and required signal amplification.

1.2 Materials

Here, we discuss the different materials that are of interest as components of surface-enhanced Raman sensors. This includes the optically-active metal nanostructures used for signal enhancement, porous 3D alumina membranes used as waveguiding and supporting platforms for sensors, and the biological ligands used to functionalize the sensors with highly specific moieties for biomolecule detection. A complete understanding of the intrinsic properties of each component of the sensor allows for the rational design of highly specific and sensitive detection substrates.

Nanostructure assembly has been an area of intense research due to the unique plasmonic properties of aggregated metallic nanoparticles useful for a number of applications.[57,58,59,60] These nanostructure aggregates have shown a potential for a wide variety of application in biological,[61,62,63] chemical,[64] vapor,[65] environmental,[66] and hazardous materials sensing and identification.[67,68,69] In contrast to conventional and widely used spherical nanoparticles, anisotropic noble metal nanostructures such as nanowires, platelets, nanorods, nanocubes, and nanoframes with sharp edges and corners provide a great deal of surface area for molecular binding as well as orientation-dependent plasmonic behavior.[70,71] Metal nanostructures have been extensively studied and applied in biological related fields such as biodiagnostics,[72,73] disease therapy[74] including controlled release and drug delivery,[75] and medical imaging.[76]

1.2.1 Metallic nanostructures

In SERS studies, noble metallic nanostructures are utilized for their excellent optical and plasmonic properties. Gold and silver nanostructures are optimal as a result of their interaction with light in the ultraviolet, visible, and near-infrared regime. The optical properties of these nanomaterials are highly depended on the nanostructure composition, size, shape, and state of aggregation leading to a wide range of tunability for proper sensor design (see Figure 1.3). This tunability is particularly critical for SERS sensor design because the complex interplay between the target and the nanostructured hot spots requires light interaction over the entire visible and near-infrared range and can open possibilities for the detection of new analytes such as biological molecules. A brief introduction on the structure and properties of gold and silver nanostructures that are most relevant to this study are discussed below.

1.2.1.1 Silver nanostructures

The plasmonic properties of silver nanostructures have recently become an area of intense research as a new application of the noble metal silver, which has traditionally been used for ornamentation, electrical conductors, mirrors, films for photography, and antimicrobial coatings in biomedical and textile applications.[77,78,79,80] Also, small amounts of silver have historically been used medically as it is not harmful to human cells, but is lethal to most bacteria, which has also given silver applications in water and food disinfection.[81] In a nanocrystalline form, silver has been used in a wide variety of areas for its exceptional properties and performance in electronics, chemical catalysis, biosensing, and optical labeling.[82,83,84,85] The wide variety of applications of silver nanoparticles is the direct result of the extensive range of property tunability of such nanostructures by varying size, shape, and degree of aggregation.[86,87,88,89]

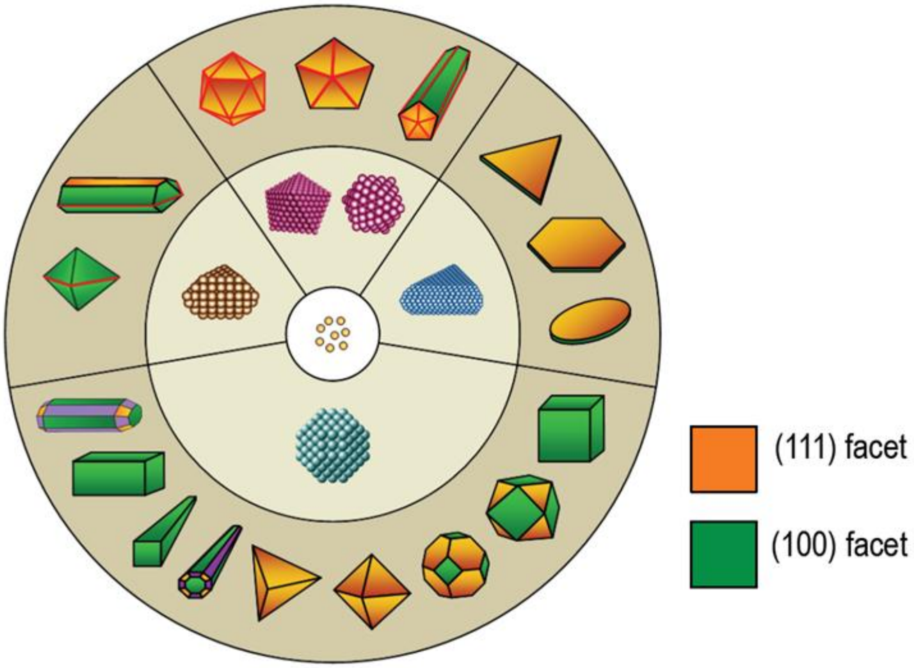

Figure 1.5 Different shaped silver nanostructures that can be formed by varying the capping agent, reaction conditions, and ratio of reactants in chemical reduction synthesis.[89]

There have been a wide variety of chemical and photo reduction techniques developed for synthetic routes to produce nanocrystalline silver including simple spheres, cubes, rods, bipyramids, plates, and other complex structures (Figure 1.5).[90,91,92,93,94,95,96] These techniques allow for the repeatable and often simple synthesis of silver nanostructures for plasmonic applications with peak absorbance ranging across the visible and near infrared regimes. The shape and size of the nanostructure can be controlled by the capping agent used, the reaction conditions, and the ratio of reactants in the chemical reduction process. For example, Xia et al. have demonstrated that a perfect or truncated octahedron (lowest energy state) can be achieved by using sodium citrate as a capping agent because it preferentially binds to the (111) crystal face of the nanostructure. On the other hand, when polyvinypyrollidone (PVP) is used as a capping agent, silver nanocubes can be formed because PVP preferentially binds to the (100) crystal face, leading to the complete growth of the remaining regions.[89] The stabilization of crystal faces that are not necessarily lowest energy allows for the synthesis of unique crystal growth and these strategies have been extensively studied.

There are also silver nanoparticles reduction methods that do not require capping agents, which allows for direct surface reduction, no interference by capping agents in sensing studies, and simple, bath-type processing and conformal surface functionalization. This technique is called electroless deposition and is a modified seeded growth method that can be applied to a variety of surface functionalization applications. However, there are issues such as size uniformity and large-scale aggregation that can be viewed as either positive or negative attributes depending on the application.

For their exceptional tunability of plasmonic and other properties, silver nanostructures have been applied in surface-enhanced Raman scattering (SERS) sensors. An added reason for the use of silver nanoparticles for SERS is that these nanostructures do not have any electrical transitions in the visible regime which can lead to enhancement losses that occur in other metals such as gold or copper.[97,98] Drawbacks of silver nanoparticles, however, are their extremely fast oxidation rate in air and questionable biocompatibility.

1.2.1.2 Gold nanostructures

Historically, gold has been used in a wide variety of applications such as coatings, jewelry, coins, and electronics as a result of its noble properties, meaning it is unreactive over long periods of time with no evidence of chemical oxidation or deterioration.[99] Gold has also been used in its molecular form as a catalyst for chemical reactions as well as in medicines.[100,101,102] However, in this work, the focus will be on the unique properties of gold as on the nanoscale a tool for enhanced electromagnetic fields resulting from coupled plasmonic behavior with photoexcitation. On the nanoscale (less than 100 nm) gold can exhibit unique characteristics such as striking colors, but most importantly it has extremely unique electronic properties.[103]

As a nanscale material, gold has been used extensively since ancient times for its vivid optical properties and methods for nanosized gold colloidal solutions date back to the Roman Empire.[104,105,106] However, the first scientific publication of colloidal gold is attributed to Michael Faraday in 1857 for his report of the reduction of gold chloride in aqueous solution by phosphorous and stabilized with the addition of carbon disulfide.[107] In fact, the most widely-used method of chemical reduction of gold nanospheres follows a similar procedure in which a gold salt is reduced and stabilized with a capping agent in aqueous solution.[108,109] Since that time, gold nanostructures have been applied in a wide variety of fields including medical imaging and diagnostics,[72,110,111] plasmonic sensors via assembly,[57] photonics,[112] as well as many other applications.

As was previously described with silver nanoparticles, gold nanostructure shape and size play a tremendous role in the plasmonic behavior of the nanostructures leading to the ability to tune their absorption across the visible and infrared spectrum by changing these variables. A great deal of work has been done to obtain different shapes and sizes of gold nanostructures as is illustrated in Figure 1.6. These include gold nanospheres,[109] nanorods,[113] nanocages/nanoframes,[92,114] nanocubes,[115] among many other unusual shapes.

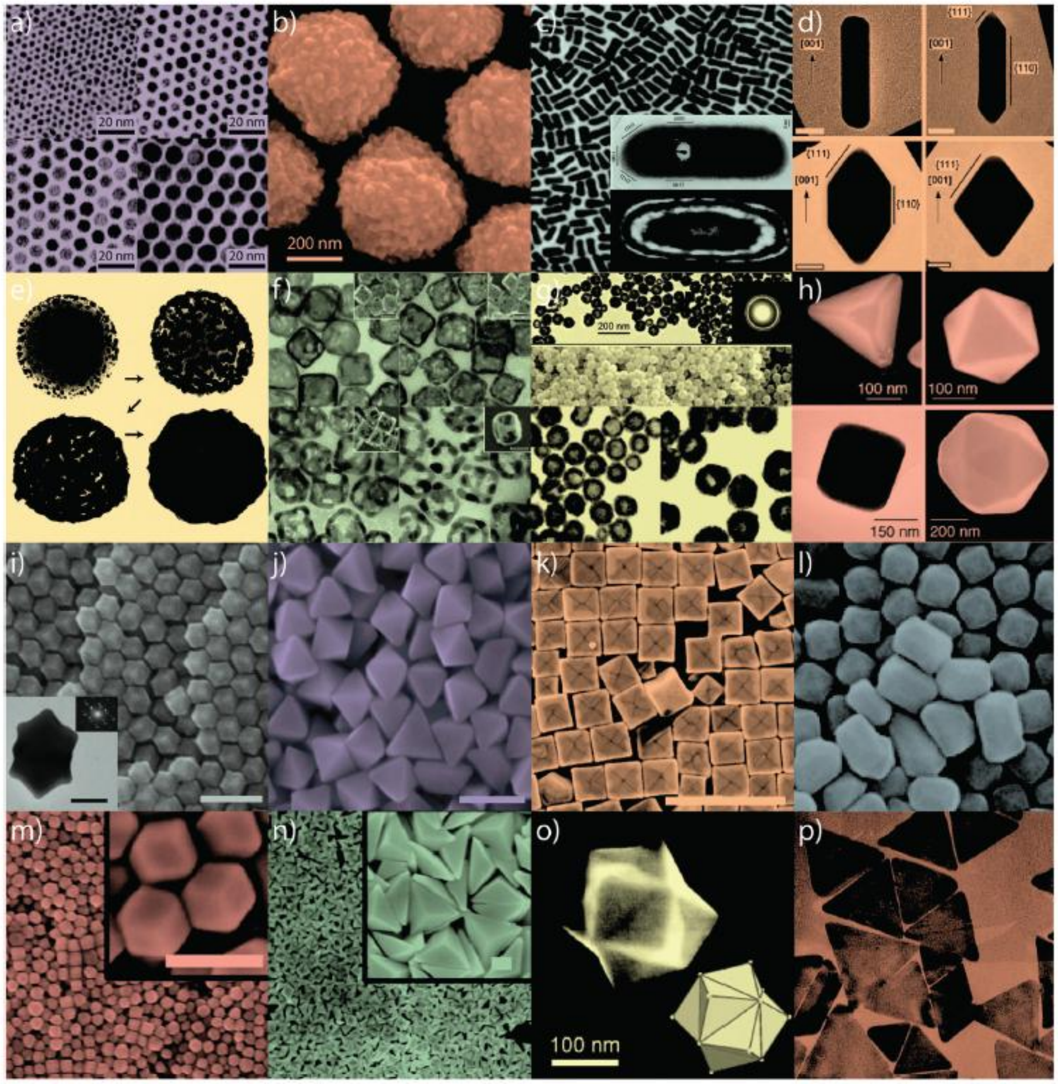

Figure 1.6 Different shaped gold nanostructures that can be formed by varying the capping agent, reaction conditions, and ratio of reactants in chemical reduction synthesis.[99]

1.2.2 Porous alumina membranes

There has been great interest in recent years directed at the development of porous nanohole arrays exhibiting a great degree of order. These arrays have attracted attention due to their potential use as templating systems for nanostructures that can be used as optical, electronic, or magnetic devices.[116,117] Anodic alumina is one such porous array and has been shown to provide a self-ordered nanochannel material.[118] Through the use of a two-step anodization process, highly ordered porous alumina membranes have been formed with a large range of pore sizes from 50-400 nm (Figure 1.7).[119] The change in pore size can be attributed to variation in the electrolytic solution (oxalic or phosphorous acid) and the applied voltage during synthesis. The optical transparency of porous alumina membranes over a wide range of wavelengths (particularly in the visible regime) makes them ideal substrates for the study of nanostructure assemblies. These membrane templates have been used for the fabrication of 3D SERS substrates as a result of their high degree of order, optical waveguiding properties, and ease of surface modification with plasmonic metal nanostructures.[60]

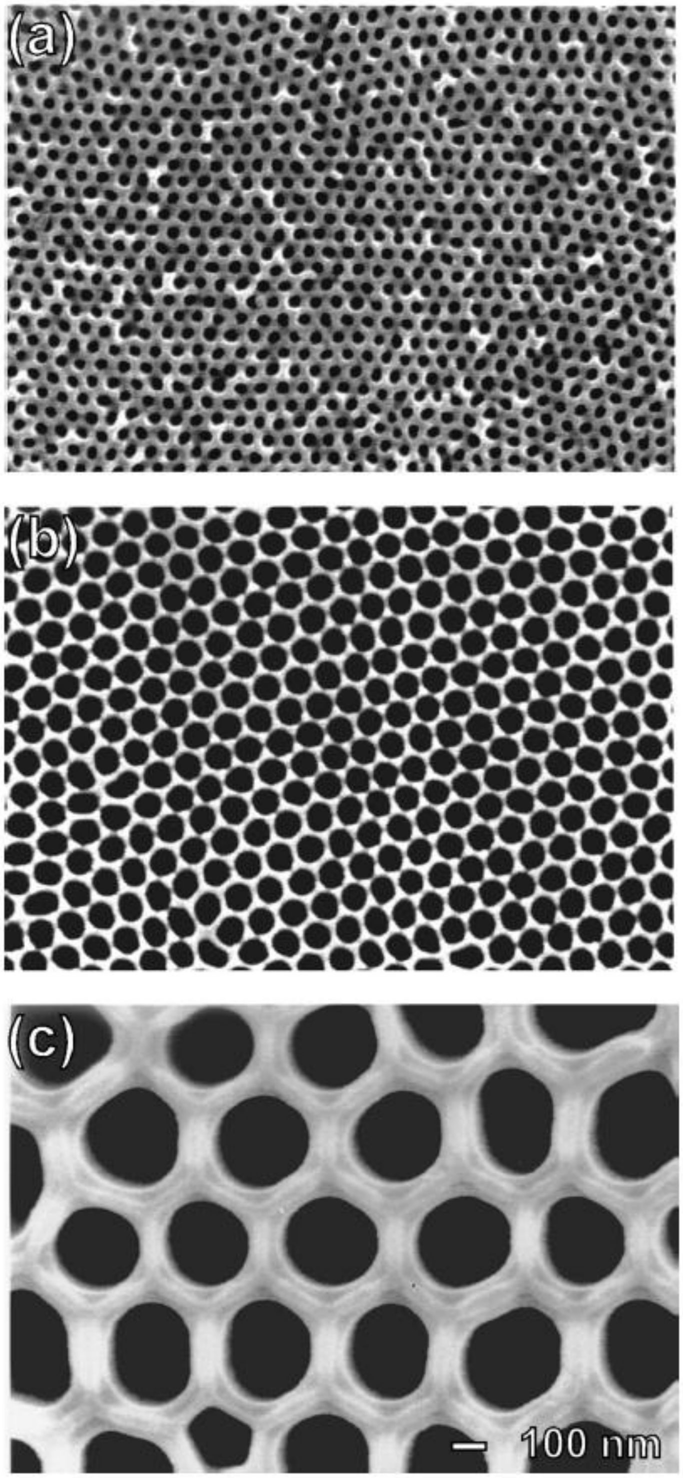

Figure 1.7 SEM micrographs showing the high degree of order and pore size tunability of porous alumina membranes formed with different voltages and electrolytic solutions.[119]

1.2.3 Standard Raman markers

In order to provide a fair comparison between the novel two- and three-dimensional substrates described in this work, it is important that common, standard Raman analytes are used for initial verification of sensor function. These molecules are typically fluorescent dyes or strongly binding small molecules. Highly resonant fluorescent dyes such as rhodamine 6G can be deceiving when reported a substrate's enhancement factor because they can contribute up to 10^6 enhancement from chemical resonance of the molecule alone.[41,44] For this reason, researchers often use benzenethiol as an alternative because it has a distinct Raman spectrum, has no innate chemical resonance, and can strongly bind to metal nanostructure surfaces as a result of the thiol-metal interaction.[120] These two common Raman analytes provide a foundation for the description of a substrate's enhancement properties that can be universally understood and compared across the field of SERS research and are therefore the basis for molecular detection in this work.

1.2.4 Biological molecules

The understanding of biological processes and the extremely wide variety of molecules that influence and interact during such processes is a critical requirement for the development of future medical detection, treatment, and prevention therapies. In many applications such as emergency workers, pilots, and medical personnel, it is critical to determine and monitor the level of fatigue and cognitive function of individuals. However, there are currently no in-the-field type monitoring systems for such applications that can provide reliable and label-free detection of specific biomolecules related to these issues. In the following sections, the biomarkers of interest for stress-related detection as well as the recognition elements to be used for their detection in this study are discussed.

1.2.4.1 Stress-related biomarkers

There are several different biological molecules that are interest in this study that range from neuropeptides and catecholamines, to hormones and vitamins, but all are related to stress, fatigue, and alertness reactions in the body. Catecholamines and corticosteroids have been chosen due to their physiological importance as stress-related biomarkers, functionalities that can be observed via Raman measurements, and the relatively small size of these biomarkers compared to other biological species (Figure 1.8). These biomolecules are important to monitor due to their ability to evaluate stress levels, cognitive ability, and fatigue. Catecholamines are a group of biomolecules secreted from the andrenal glands and are derivatives of tyrosine.[121] They are secreted in response to positive or negative stress. Their release can create a rapid increase in the basal metabolic rate and can have a dramatic effect on the subsequent production of other biomolecules. The concentration of catecholamines in the blood can also be an indicator of an individual's current state of stress and alertness. Cortisol is one example of a corticosteroid that has the primary function of increasing blood sugar and suppressing the immune system.

To date, trace detection of catecholamines has not been studied using Raman spectroscopy. However, there are several Raman studies of bulk samples that can be used as references for spectral assignment.[122,123] For example, dopamine has characteristic Raman peaks at 785 cm^{-1} (in-plane catechol ring vibration) and 1280 cm^{-1} (C-O stretching)[123] that can be monitored to determine the binding conditions and limit of detection of the bioanalyte.

These biomarkers offer a wealth of advantages for sensor design and understanding because they are small in size and contain functional groups that can be trapped within SERS hot spots at different levels of specificity. The small size of these molecules allows for the capability to model how the biomolecule binds and to predict the Raman signature based on which functional groups interact with the metal surface.

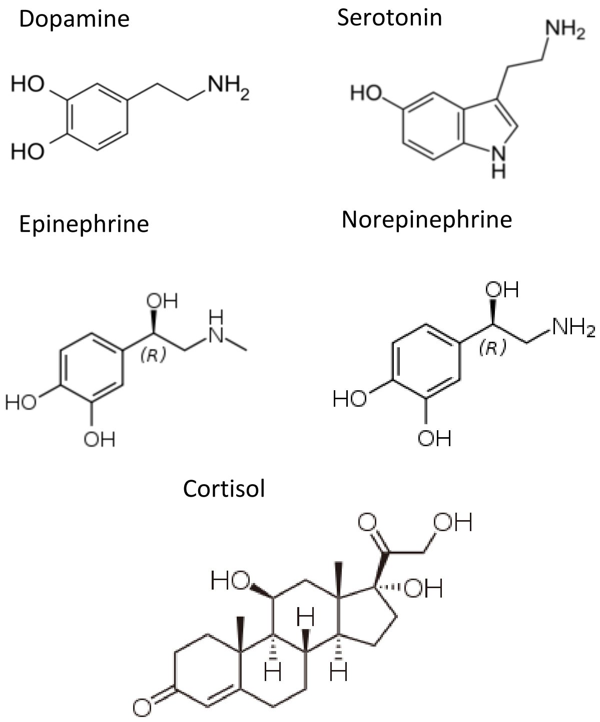

Figure 1.8 Stress-related biomarkers of interest for SERS detection.

More complex and larger bioanalytes are also relevant to stress-related situations and can provide more detailed information regarding the state of fatigue such as neuropeptide Y, interleukin-1β, and orexin-A (Figure 1.9).[124,125,126] Higher levels of orexin-A have been shown to increase cognitive function and ability in short term memory tasks.[127] Neuropeptide Y is attributed to food intake levels, sexual function, anxiety responses, and vascular resistance.[128] Interleukin 1β is an important biomarker in the inflammatory response.[129] Another biomolecule for detection is riboflavin, also known as vitamin B_2, is an important molecule for electron transfer reactions in the body, cell growth, and can even be used as a treatment for some clinical diseases.

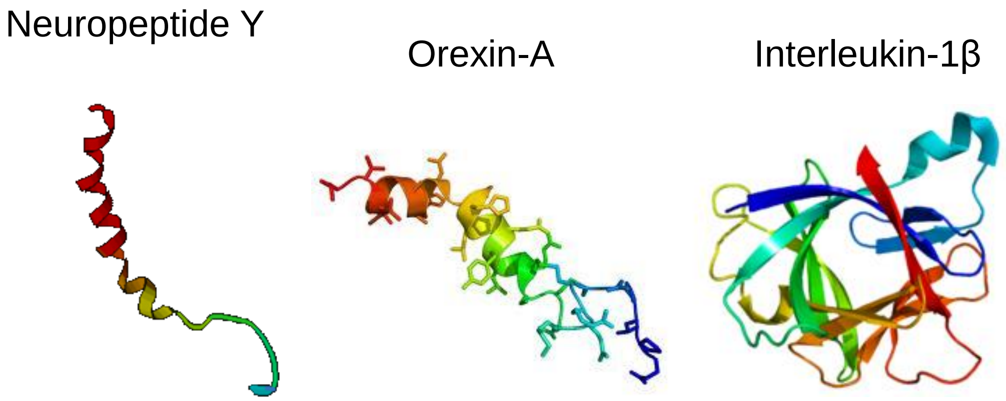

Figure 1.9 Structures of more complex biomarkers important in stress-related responses.[124,125,126]

Another important biomolecule for trace detection is immunoglobulin G (IgG) which is the most abundant immunoglobulin in the blood and is produced in large quantities during secondary immune responses.[121] For this reason, IgG can act as a representative molecule for the SERS detection of large proteins. The binding of the Fc region of IgG, which coats microorganisms in the blood, and the Fc receptors of macrophages and neutrophils allows these phagocytic cells to bind, ingest, and destroy invading bacteria.[130] The accurate and trace detection of IgG is extremely important in an effort to better understand its role in complement responses in the body and other concentration dependent roles it may play. IgG binding to specific surface chemistries is also of interest and can lead to further insight into SERS substrate design for specifically binding large proteins at nanostructure hot spots.

1.2.4.2 Biorecognition elements

In order to detect trace amount of biomarkers in complex fluid, a great degree of specificity must be integrated into the sensor design. This can be achieved by using specific biorecognition elements such as aptamers, peptides, or antibody fragments that bind specifically and only to the target molecule of interest.

Among prospective selective biomolecules, aptamers are well-known short single-stranded DNA or RNA sequences that can bind target molecules with a high affinity to different biomolecules. The compact nature of these molecules gives them a distinct advantage over large-volume antibodies for designing selective "hot spots" for SERS detection.[131,132,133,134,] Huh and Erickson have demonstrated the use of an aptamer to specifically detect the peptide hormone vasopressin using a fluorescent label as the Raman marker.[135] The detection of adenosine triphosphate down to nM level was also demonstrated using SERS aptamer detection by Li et al.[136] It was shown that the Raman spectra of the DNA thrombin-binding aptamer can differ significantly from its SERS

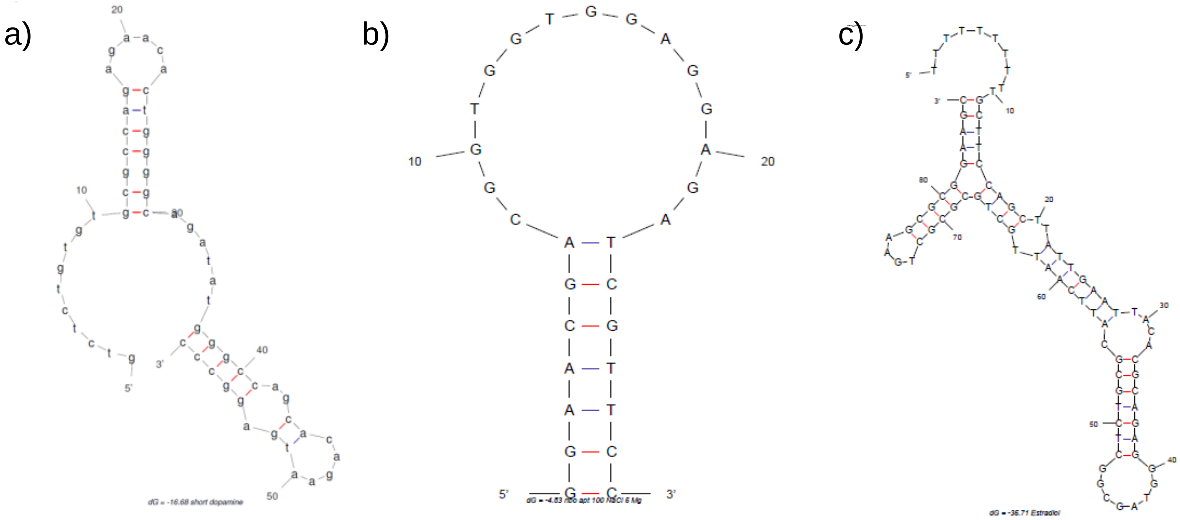

Figure 1.10 Known aptamers for a) dopamine, b) riboflavin, and c) estradiol as examples of aptamer structures for selective binding.[144]

counterpart upon binding to nanoparticles, likely due to changes of aptamer conformation.[137]

Alternatively, short selective peptides with tailored sequences can be immobilized onto metal nanostructures by using proper functional linkers. These molecules are selected according to phage display studies and are capable of firmly binding different synthetic and organic molecules such as cancer biomarkers and lethal molecules, and can be furthermore developed for different targets.[138,139] Surface adsorption of peptides on various metal surfaces has been performed, but these studies typically did not utilize fine and well-controlled nanostructured surfaces.[140] Other prospective highly specific probes are antibody fragments (nanobodies) which are short segments of selectively binding anitbodies that are not as bulky as traditional antibodies. [141]

As selective binding agents, functionalized short molecules and aptamers can be tethered to hot spot regions of the substrates using the strong interaction between a terminal thiol group and gold or silver surfaces in order to improve the selectivity and sensitivity of the substrates based on selective recognition of the biomarker. Examples of aptamers for dopamine,[142] riboflavin,[143] and estradiol are shown in Figure 1.10. Aptamer selection and testing was done in collaboration with the Kelley-Loughnane group at AFRL. The lowest energy folding structure of these single-standed DNA aptamer sequences is determined using the well-developed Mfold software.[144]

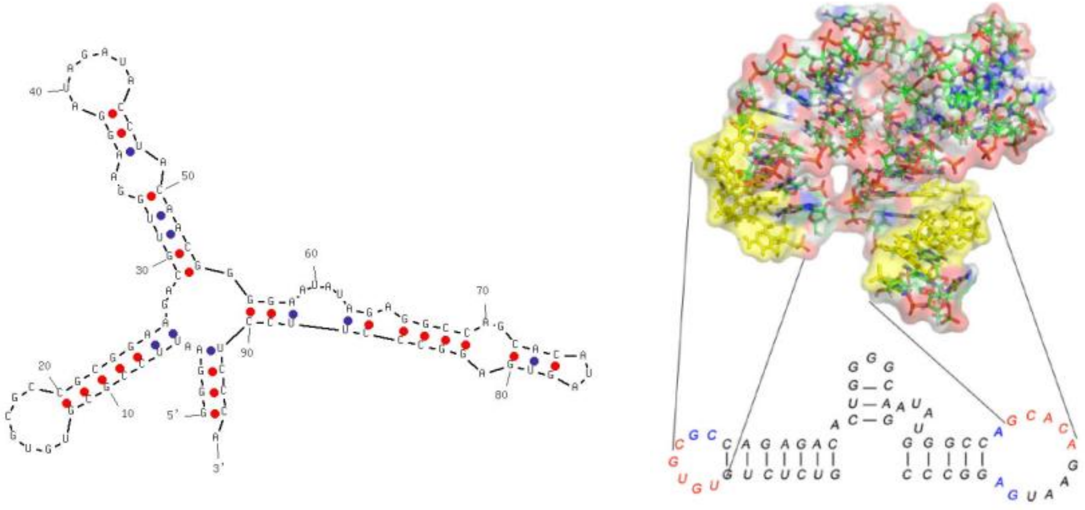

Figure 1.11 a) dopa2 – aptamer selective for dopamine.[142] b) Proposed binding sites for dopamine shown in yellow.[145]

In order to detect the SERS effect for specific analytes, the targeting molecules must be placed in a manner that allows the bioanalyte to be trapped within the interparticle junction. This binding can be guided through the variation of grafting density of the targeting molecule as well as passivating other regions of the substrate. The short synthetic organic ligands first tested in this project will be thioglycolic acid, which can bind to the amine group of dopamine. One potential biomarker to be tested is dopamine because there are known selective binding aptamers for this biomolecule (Fig. 1.11). The aptamer *dopa2* has been shown to be selective for dopamine and will be employed as a targeting binding agent in our substrates. There are several other examples of aptamers for dopamine composed of DNA and RNA[142,145] and also for riboflavin and neuropeptide Y[146] that can be purchased from Integrated DNA Technologies. Selection of bioanalytes and corresponding aptamers was also conducted in collaboration with Dr. N. Kelley-Loughnane, who supplied properly design aptamers beyond those available commercially.

1.3 Applications of SERS

SERS has attracted much attention recently as a highly sensitive probe for the trace level detection of small organic molecules since the demonstration of single molecule detection.[20,22,147,148,149] It has also been shown that SERS has great potential for monitoring internal chemical composition, inner stresses, and trace detection of hazardous molecules.[150,151,152,153,154,155,156,157] SERS phenomenon is possible due to the large electromagnetic fields that exist in the small gaps between metal nanostructures called hot spots.[158] The design of the substrate on which the SERS phenomenon becomes significant is the most critical aspect of a sensitive probe for small molecules or biomolecule analytes. Various design strategies have been suggested in order to provide dramatic enhancement for the SERS response. Typical SERS substrates include roughened metal nanoparticle films,[159,160] metallic and bimetallic nanostructures,[63,71,161,162,163,164,165,166,167] and three-dimensional porous substrates.[168,169,170,171] The highly specific and sensitive detection of liquid and plastic explosives, hazardous chemicals, and biomolecules has been demonstrated using SERS as the detection mechanism elucidating the significance of this sensing technique.[64,68]

1.3.1 Chemical and environmental detection

Arrays of nanoparticle assemblies show great potential for SERS enhancement due to their ability for guiding electromagnetic energy. [172,173] These nanostructured arrays can provide light confinement properties and excite hot spots for an enhanced electromagnetic field.[31,174,175,176,177] The 3D ordering of metallic nanostructures can further increase field enhancement compared to planar 2D substrates. Among others, porous anodic alumina membranes (PAMs) with ordered cylindrical nanopores have been widely used as 3D templates to assemble metallic nanostructures for SERS applications (Figure 1.12).[178,179,180,181] As compared to other porous substrates, PAMs provide a higher degree of light propagation through the depth of the vertically aligned channels and are beneficial for efficient light interaction because of optical transparency and waveguiding properties.[182,183]

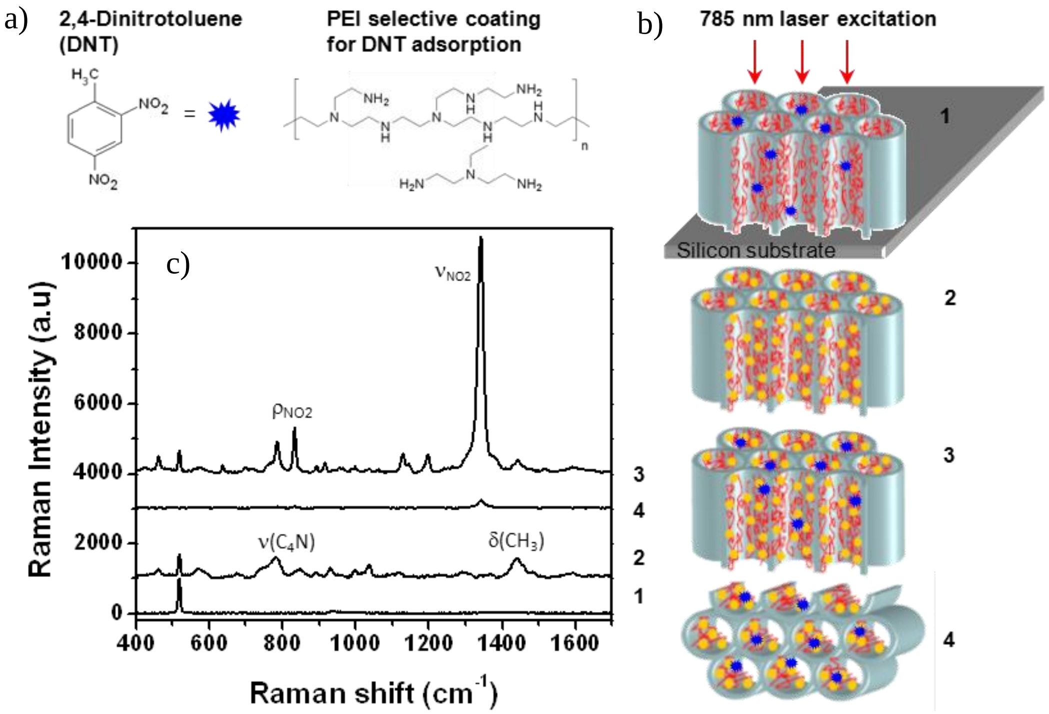

Figure 1.12 (a) Chemical structure of 2,4-DNT and PEI used for binding. (b) Raman measurement of 2,4-DNT with different light incidences to the SERS substrates. The excitation light is parallel (1,2,3) and perpendicular (4) to the pore-canal axes. (c) Raman spectrum of 1000 ppm 2,4-DNT on each substrate.[60]

The open nanoporous structures of this type which are exploited in previous studies in our group and in continuing research can also be advantageous for SERS sensing due to the high degree of through transport of analytes and high surface area which can result in excellent enhancement (Figure 1.12).[60] These studies, using PAMs as SERS substrates, demonstrated record limits of detection for plastic and liquid explosives. More specifically, the common plastic explosives of 2,4-dinitrotoluene (DNT) and 2,4,6-trinitrotoluene (TNT) were detected down to 5-10 zeptograms of material within the laser spot and the common liquid explosive HMTD was detected down to 1 picogram.[68] HMTD was identified based on the degradation products evolved from this volatile molecule upon laser exposure during SERS measurement showing the versatility of the SERS technique as a method for the trace detection of small, unstable organic molecules.[64] It is suggested that SERS can potentially provide a method for label-free sensing and analysis of proteins, down to a single molecule.[184,185,186]

1.3.2 Biological detection

As has been mentioned in previous sections, current biomolecular detection is frequently based on measuring specific optical absorption such as that implemented in ELISA,[45] SPR,[53] or FRET methods.[187] These well-known approaches, however, do not provide a pathway for direct label-free detection of the biomolecular analytes within one measuring cycle. These approaches also often require a complex sequence of fabrication and labeling steps, which are costly, time-consuming, and must be designed specifically for the biomolecular system of interest.

The design of SERS substrates for trace biological detection is the most critical challenge for further advancement of this detection method. The critical improvement should be done by switching from global binding based upon weak interactions, as facilitated by single-component functionalization of metal nanostructures (i.e. polyelectrolytes, capping agents, charged ligands), to a more sophisticated multifunctional selective binding platform. By changing the surface functionalization of the metallic nanostructures of the SERS substrate, the specificity and selectivity of the substrate can be dramatically improved to allow the detection of trace concentrations and detection of single analyte species within complex mixtures. To this end, specific binding agents such as antibodies or aptamers should be utilized to selectively bind the bioanalyte of interest instead of simple organic ligands. However, successful examples of such biofunctionalization are extremely rare. Among prospective SERS-relevant binding sites, aptamers show the greatest promise because their selectivity has been demonstrated to be higher than the binding affinities of antibodies, they are more compact, and can be easily tethered to functionalized metal nanostructures.[188] These properties all demonstrate the advantage of utilizing aptamers and are all critical for the trace detection of complex biomolecules.

To date, most of the empirical efforts in this field are limited to the detection of small, highly resonant organic molecules with high Raman activity. The few SERS studies involving the detection of biomolecules have been predominantly limited to 2D substrates[189,190] or solution-based[191] SERS systems. These approaches have several

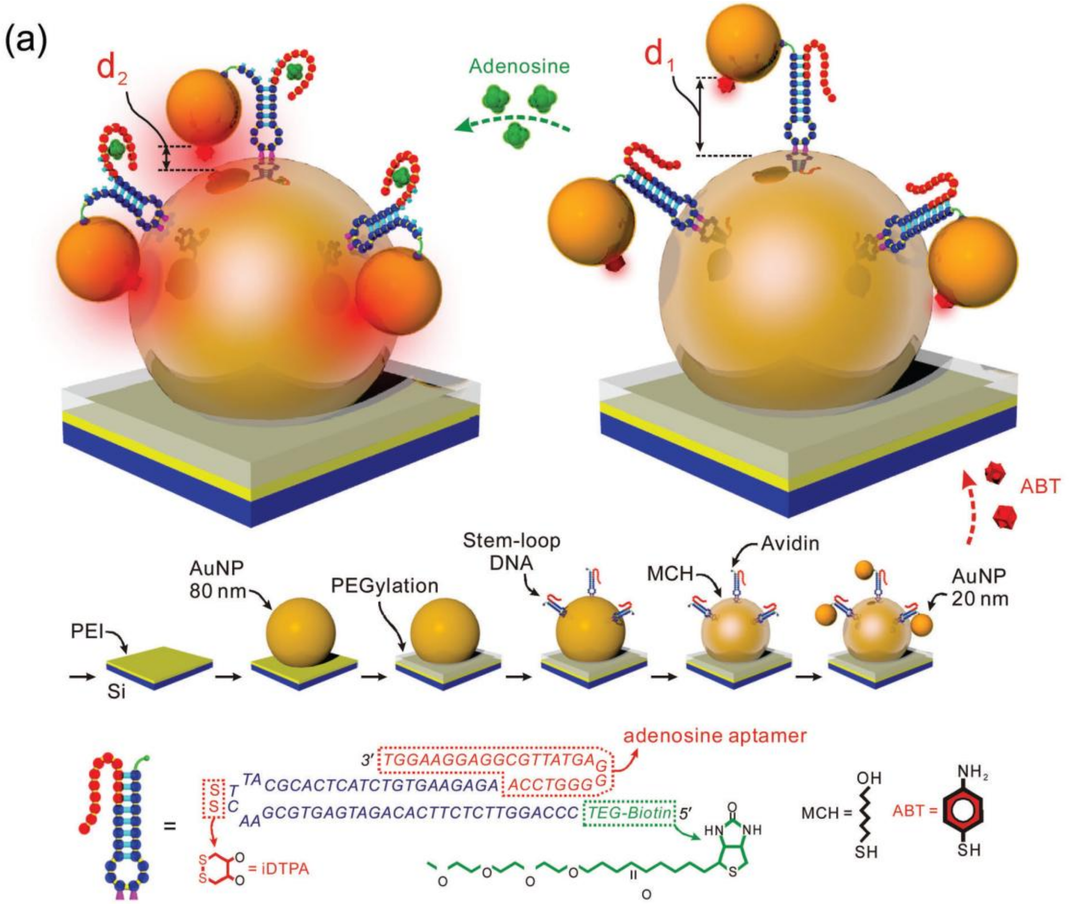

Figure 1.13 Use of aptamers for the specific SERS detection of a single biological analyte.[131]

drawbacks including the limited surface area of 2D systems, fluctuation in signal of solution methods, and overall lower enhancement than is required for the specific detection of physiological levels of complex biomolecules. In order to overcome these challenges, there are many examples in literature where researchers choose to design a SERS substrate with an integrated Raman marker for ease of detection.[131,192] This technique is also used in common biological practices such as ELISA. However, the specificity and absolute accuracy of such sensors is limited to that of the targeting element of the sensor (aptamer, antibody, peptide). It is also necessary to run several controls for each test to verify that the target analyte is actually being detected rather than another component of the complex fluid indicating a false positive.

Other reports have utilized the high specificity and selectivity of aptamers to detect biomolecules. As known, aptamers are relatively short single-stranded DNA or RNA sequences that can bind target molecules with a high affinity.[193] These molecules are relatively compact and can be derived chemically, giving them a distinct advantage over antibodies for designing biofunctionalized “hot spots”.[132,133] Indeed, aptamers have recently been exploited in SERS sensors for the detection of adenosine (Figure 1.13).[131] This method relies on the controlled nanoparticle junction formed following adenosine binding and shows preliminary detection results for a strong biomarker, 4-aminobenzenethiol. Huh and Erickson have also demonstrated the use of an aptamer to specifically detect the peptide hormone vasopressin using a fluorescent label as the Raman marker.[135]

1.4 Challenges for SERS sensor design

Although Raman spectroscopy in its enhanced mode has shown a great deal of progress, there still remain grand challenges with regard to substrate consistency, data analysis, enhancement factor measurement and reporting, and actual real-world application and implementation of this technology. Since its inception in the late 1970's,[21,194,195] surface-enhanced Raman scattering (SERS) and the design of SERS sensing technologies have progressed to more advanced levels; however, limitations in the comparability and reliability of competing technologies have hindered its use.[120] The following section will elaborate further on the challenges facing the field of SERS sensor design as well as possible solutions and opportunities for addressing these issues.

1.4.1 Substrate design

The most noticeable progress in the field of SERS has been developments in substrate design and the understanding of what components are necessary to provide the greatest degree of enhancement. From the early stages where roughed silver electrodes were the substrates of choice,[194] to the later use of silver and gold colloids,[196,197] to the application of metal films combined with metal nanostructures,[198,199] to simple, paper-based substrates,[161] and eventually to three-dimensional designs and well-controlled nanostructure hot spots,[64,67,68] the field has developed drastically with time. This can, in part, be attributed to developments in characterization tools such as high resolution scanning and transmission electron microscopies and atomic force microscopy, which have allowed for researchers to better understand the actual nanoscale characteristics of SERs substrates that are responsible for improved enhancement.[200] Figure 1.14 shows an SEM micrograph of a roughened silver electrode that was originally used for SERS detection.[201] It is important to notice the inhomogeneity and lack of nanscale junction uniformity in the surface features as these were critical drawbacks for such a sensing platform and are areas of improvement in modern SERS sensors.

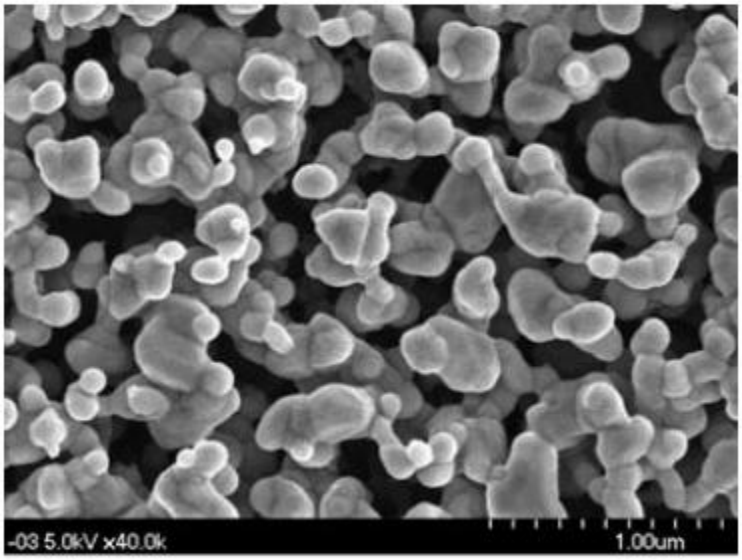

Figure 1.14 A representative SEM image of a roughened silver electrode surface.[201]

The high degree of variety of SERS substrates coupled with limited understanding of the underlying physical phenomena that occur at excite plasmonic hot spots lead to several recent issues with the field that have been described by the discoverer of SERS, R. P. Van Duyne, and coworkers in a recent article.[120] In such a rapidly growing field of SERS sensor design, critical characterization steps are often overlooked due to their complexity and this leads to the inability to compare different sensing platforms based on their sensitivity and reliability, large scale uniformity, and plasmonic tunability.

However, recently the limits of plasmonic enhancement effects as they relate to metal films separated by well-controlled distances from spherical metal nanoparticles have been explored in detail by Ciracì et al. and a schematic of their substrate design is shown in Figure 1.15.[199] By using extremely well-defined spacer layers composed of layer-by-layer polyelectrolyte films for larger separation distances (greater than 3 nm) and self-assembled monolayers of alkanethiols for smaller separation distances, they were able to show localized enhancement factors for such systems. These empirical results were then confirmed with simulations of the plasmonics fields of the nanospheres over the same distances and essentially defined and characterized the upper limit of enhancement for two-dimensional SERS substrates utilizing such nanostructures.

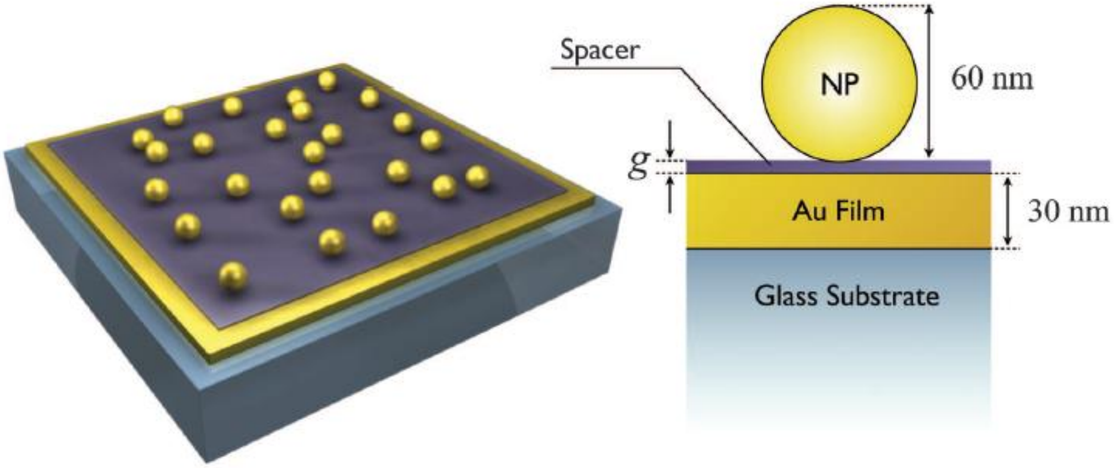

Figure 1.15 Geometry of the film-coupled nanoparticle system. (left) Schematic of the sample. (right) Cross-section of a single film-coupled nanosphere.[199]

Another well-developed and well-controlled two-dimensional substrate is that of immobilized nanorod assemblies fabricated on microsphere assemblies.[200,202] These substrates rely on the well-known approach of microsphere assembly on two-dimensional substrates followed by the deposition of silver nanorods using thermal vapor deposition (Figure 1.16). This allows for large-area enhancement uniformity across the entire SERS substrate, which is typically very difficult to achieve with a high enhancement factor. The plasmonic behavior of the assembled nanorods and overall substrate can easily be tuned by changing the size of the microspheres used as the sensor foundation. The uniformity and reproducibility of the substrate give this technique an advantage over traditional two-dimensional nanostructure assembly. However, it should be mentioned that although high enhancement factors (EF ~ 10^7) are achieve with a high level of

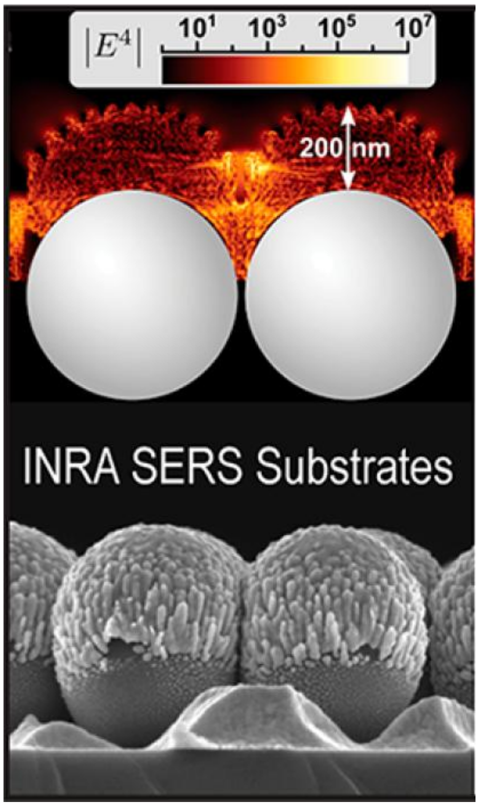

Figure 1.16 Immobilized nanorod assemblies (INRA) SERS substrates. (top) DDA simulations of the electromagnetic enhancement of INRA substrate with (bottom) corresponding SEM of the actual substrate.[202]

uniformity, these values can be further improved by transitioning to three-dimensional substrates as described in Chapters 4 and 5.

1.4.2 Nanostructure hot spot design

Although the overall substrate design is critical for sensing capabilities, advancement in the understanding of electromagnetic field enhancement as a result of the coupled plasmonics between aggregated metal nanostructures has given researchers the ability to manipulate the nanoscale assembly of individual nanoparticles in order to tailor the plasmonic behavior of the SERS substrates.[120,203] The design and control of electromagnetic SERS hot spots is most often carried out by the precise control of metal nanostructure aggregates as the enhanced region of the aggregate is dependent on the nanostructure size, shape, composition, and most importantly, the distance between individual nanostructures.[57] This assembly has been achieved through a variety of both top-down and bottom-up approaches including, but not limited to, lithographic techniques,[204,205] as well as electrostatic,[206] polymer,[70,207] and DNA[208,209] mediated assembly.

Top-down nano-patterning techniques like electron beam lithography (EBL) are one group of methods that address issues associated with the intentional formation of well-defined SERS hot spots and their characterization using multiple techniques through strict control (<5 nm resolution) of the nanostructure parameters that affect plasmonic coupling and SERS enhancement.[210,211] The EBL approach involves the exposure of a polymer resist to an electron beam in specific regions according to a computer design. The regions of polymer exposed to the electron beam are either degraded by breakage of their main chains into smaller pieces (positive resist) or strengthened through cross-linking (negative resist).[210] This process can produce nanostructures that have almost any shape[204,212] with geometrical dimensions typically well below 100 nm on materials like silicon nitride,[204,212] and quartz.[30,213] Improved adhesion of the nanostructures to the surface allows insulating surfaces like glass to be used as the substrate,[210,214] making more robust designs. Several studies have examined the relationship between structural and optical properties of nanostructures, including super-resolution optical imaging nanoantenna arrays,[215] nanodisk resonators,[216] and the transition of nanotriangle-nanohole arrays.[217] Occasionally, EBL substrates have been explored for SERS enhancement as well; however, only array-averaged signals have been analyzed.[218,219] These studies often do not involve the necessary type of well-defined nanostructures or only examine properties from a bulk perspective and without functionalization.

With recent advances in the understanding surface functionalization and the characterization tools required for monitoring features on the nanoscale, molecularly-mediated assembly of nanostructures in solution has also become an area of intense research for the design of SERS hot spots.[57] Not only can the surface chemistry of nanostructures determine their binding length from each other and their aggregated state, but functional surfaces can provide an additional tethering mechanism for trapping the analyte of interest in a SERS sensor.[203,220]

One method for nanostructure assembly that has gained a great deal of attention recently is the utilization of DNA as either an electrolytic or hybridization mechanism for controlled nanostructure aggregates.[72,221,222] One of the first examples of such a SERS sensor was developed in the Mirkin group, where gold nanoparticles functionalized with common Raman dyes as well as gold surfaces were both functionalized with oligonucleotides that could specifically bind to a target in solution.[223] When binding occurred, the nanostructures coated with Raman dyes were brought into close contact with the gold surface, thus facilitating a hot spot and eliciting the enhanced spectrum of the Raman dye. A more recent example is the use of oligonucleotide-functionalized gold nanoparticles to detect DNA in solution with well-controlled gap distance and subsequent signal amplification.[224] This was done by including a secondary step in which the gold nanostructure acted as a core nuclei while a silver shell was grown in solution following DNA binding, thus decreasing the nanogap distance (Figure 1.17). This amplification step allowed for the detection of a single molecule of the DNA target with a common Raman dye.

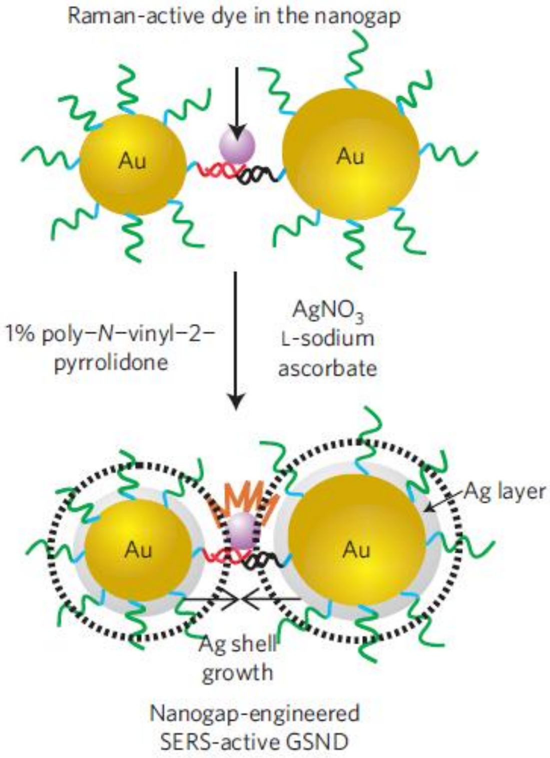

Figure 1.17 Schematic illustrating the single-molecule DNA binding of gold nanoparticle dimers followed by silver reduction to form a core-shell system with a well-defined hot spot gap.[224]

Researchers have also recently developed particle surface modification techniques that allow the isolation of controlled aggregates contained a defined number of nanostructures in order to create well-defined plasmonic properties and therefore consistent SERS hot spots.[57,200,206] One of the earliest examples of controlled aggregate size was the encapsulation of gold nanoparticle dimers and trimers with silica shells after the entrapment of Raman reporter molecules.[225] This type of nanoantenna SERS structure was found to have remarkably limited diversity in enhancement factors as a result of well-defined plasmonic properties leading to highly consistent SERS measurements.[226]

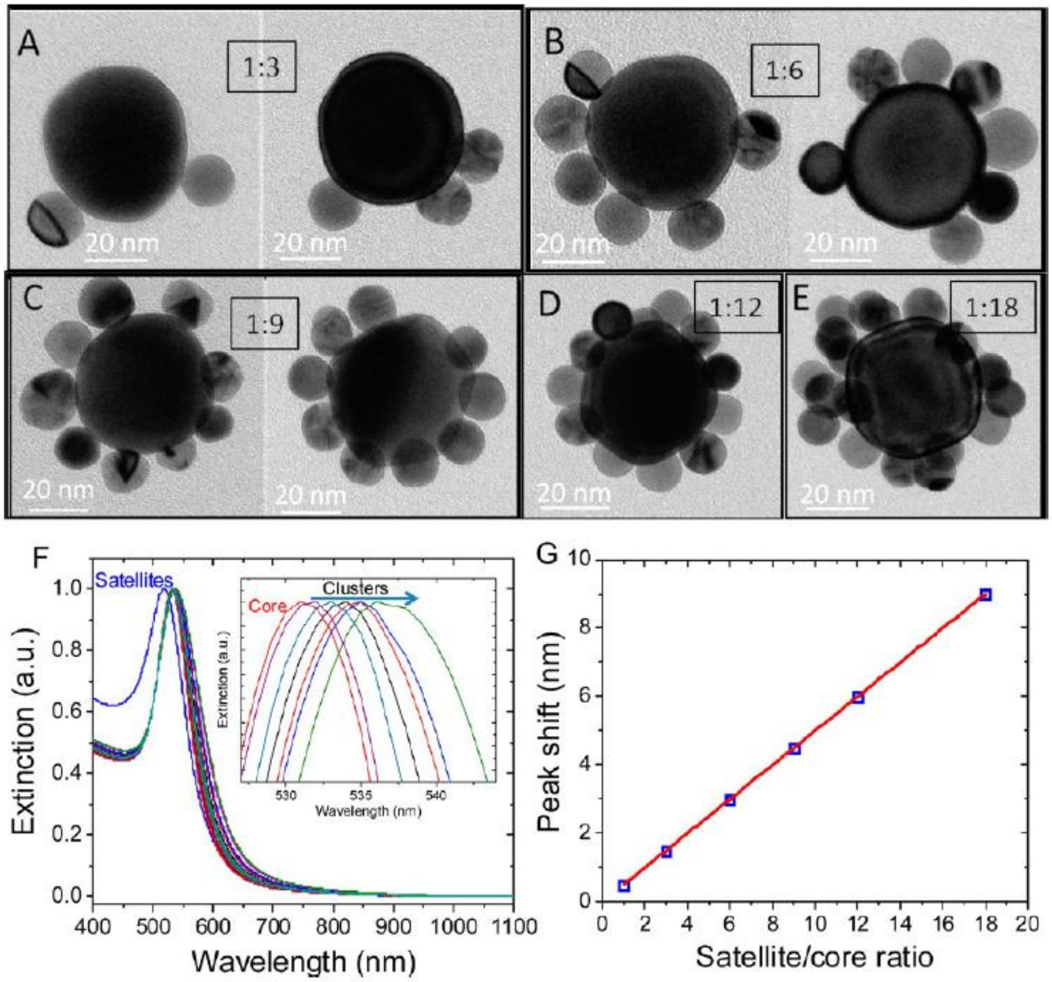

Figure 1.18 TEM images (A−C) showing various core-satellite assemblies based on the ratio of particles. (F) Extinction spectra of satellites, cores and core−satellite clusters with varying satellite/core ratio. Inset shows the progressively increasing red shift of LSPR wavelength of the core−satellite clusters with increase in satellite/core ratio. (G) Plot depicting the linear increase of LSPR wavelength red shift with respect to the LSPR wavelength of the cores as the satellite/core ratio is increased.[228]

Another example of controlled assembly is the formation of "planet-satellite" type structures which can provide increased enhancement and defined light interaction.[227,228] Figure 1.18 shows examples of the planet-satellite type configurations that can be achieved to create a high density of well-defined hot spots. These aggregates are formed using electrostatic interactions of the oppositely-charged gold nanostructures that compose the core and satellites. When mixed at the proper pH, these particles form clusters that provide the hot spot formation necessary for high SERS enhancement.

These examples of current SERS sensing and substrate design technologies demonstrate the many novel approaches to creating sensitive detection platforms. However, there are still critical issues that are overlooked and will be addressed in this study. Most particularly, these include the transition to a three-dimensional sensing platform in order to maximize light interaction and signal amplification, developing design principles that can be used to enhance SERS signals, moving from labeled approaches to label-free sensing for real-world SERS detection, and applying the ever-growing field of SERS sensing to biological detection with highly sensitive and selectively functionalized nanostructure hot spots. Specifically, current substrate designs have many limitations including random nanostructures, solution-based sensing, low nanoparticle density in two-dimensional substrates, simple chemistry with limited selectivity, and mostly spherical nanostructures with single resonances. The issues and possible solutions will be discussed in more detail in the motivation section.

1.5 Motivation

As the field of nanotechnology advances, so does the demand to utilize the unique and extraordinary properties of materials synthesized on the nanoscale. One such application of these novel structures is in the broad field of sensing devices spanning chemical, environmental, and biomedical detection systems. The development of SERS-based sensing devices involves the culmination of several critical guidelines in order to ensure proper function including (1) the identification of localized surface plasmon modes in the nanostructured substrate, (2) verification of the enhancement properties of the substrate using a non-resonant analyte to remove any chemical enhancement contribution, and (3) rigorous characterization of the nanostructured properties of the substrate using advanced characterization techniques (TEM, SEM, AFM) and correlate these properties with theoretical calculations and SERS measurements.[120] Although there are several examples described in the previous section that meet this criteria, there are several critical gaps in the study of SERS substrates that prevent these unique sensing platforms from transitioning to well-understood, reliable, and sensitive real-world sensing devices.

The first critical gap in the development of SERS substrates is the in-depth and detailed understand of the fundamental principles and properties of three-dimensional substrates and how they can be tailored to maximize enhancement. It has been shown in recent studies, related to two-dimensional substrates, that a well-controlled separation distance between two plasmonic structures (whether it be two nanoparticles or a nanoparticle and a surface) provides the absolute enhancement limit for SERS detection and has even resulted in single molecule detection.[20,199] However, for the real-world application of SERS substrates, consistent and quantifiable detection at this same trace level is required. For this reason, we suggest that three-dimensional substrate design is the pathway towards high sensitivity. Transitioning to the third dimension adds significant complications to fully understanding how to maximize enhancement such as multiple reflections leading to multiple light/hot spot interactions, depth of excitation source penetration, directionality of the incident beam in relation to the nanostructure aggregate orientation, and possible reusability of the substrate. Developing a deeper understanding of the fundamental phenomena that relate to the electromagnetic and chemical enhancement in three-dimensional SERS substrates will be an essential element of this study.

Large-scale uniformity and consistency over an entire substrate is an important factor that is often an issue with recent substrate designs.[202] The control of highly-localized aggregates is often the focus of current studies, but for in-the-field application, the level of enhancement and consistent signal needed over a large scale and between different substrates far exceeds that provided from single aggregate studies. Through the integration of advanced patterning techniques and substrate surface modification to induce intentionally positioned aggregation, novel substrate designs can be fabricated to address issues of substrate-to-substrate and intra-substrate signal consistency.

A largely overlooked advantage in the SERS community is the ability of this powerful technique to directly detect specific chemical functionalities and identify even similar molecules using their spectral fingerprint. This attribute of SERS sensing devices is often ignored and simplified by using labeled approaches that rely on a secondary reaction and the subsequent secondary detection of a Raman marker possessing strong chemical enhancement. This method for SERS detection is the most common in literature because it does not require an extremely high degree of electromagnetic enhancement because there is a significant contribution from the resonant Raman marker. In order to overcome this challenge, three-dimensional SERS substrates should be designed with exceedingly high enhancement factors that can provide enough signal amplification to achieve the same level of detection for both resonant and non-resonant molecules.

The practicality and simplicity of SERS sensor designs has been an area of progress in order to make this a realistic technique for in-the-field detection. For this reason, simplified and cost-effective substrate designs have been studied that incorporate nanostructures with commonly used sampling materials as well as amplification techniques to solve these issues. Paper-based swab substrates coated with gold nanorods have been shown to be able to detection down to hundreds of picograms hazardous explosive molecules through a simple wiping method of sample collection.[161] Another example of a paper-based substrate is one that utilized functionalized-gold nanorods on a paper substrate with a specific design and gradient that allows for preconcentration of the target analyte while drying.[229] This allows for the detection of a small concentration of analyte in solution by using a surface-charge gradient in the paper substrate to concentrate the entire amount of the target in an isolated location. The porous alumina substrates discussed in this study also allow for analyte preconcentration with exceptionally high enhancement.

In order to make SERS a viable method for biological detection, it is critical that the issues specific to biological systems be addressed including the specificity required to detect single analytes in complex fluids, monitor biomolecules in the state in which they would exist physiologically, create high throughput flow sensors for integration into existing equipment, and to design the hot spots so that they are biocompatible and can accommodate bulky biomolecules. Recent advances in the field of biochemistry have allowed for the development of tailored short chain biomolecules that are highly selective and specifically bind to their corresponding target. Of the greatest interest are aptamers,[131] short peptides,[138] and nanobodies,[141] as they are all small enough to not interfere with the SERS detection of the target molecule, but can still bind the target with a high degree of selectivity. This method for biorecognition and detection will be further developed in this study for the trace SERS detection of biomolecules in order advance the field of SERS substrate design for real-world applications.

CHAPTER 2

RESEARCH GOALS, OBJECTIVES, AND DISSERTATION OVERVIEW

2.1 Goals

The ultimate goal of this research is the understanding of fundamental principles that will lead to the most efficient design of potentially multiplexing, label-free, facile, ultrasensitive biological SERS-based sensors for important classes of biomolecules at physiologically relevant conditions and trace (nanomolar) concentrations. This far-reaching goal will be advanced in this research through the study of the selective binding characteristics of targeted biomolecules such as stress-related biomarkers and important biomarkers for other physiological processes with selective binding sites formed by aptamers, protein and electrostatic interactions, and short peptides. These selective binding sites will be specifically located within intentionally designed hot spots created by the surface plasmon resonance properties of metallic nanostructures interacting with light. A further understanding of the electromagnetic and chemical enhancement mechanisms related to such detection techniques will be explored using more advanced 3D porous substrates with greatly improved SERS enhancement.

We suggest that the enhanced specificity provided by aptamers and short peptides as selective binding agents combined and compared with traditional chemical functionalization methods, will eventually allow for the design of multiplexing sensors for the trace detection of bioanalytes in complex fluids. Through the implementation of selective ligands as references as well as aptamers and short peptides, substrates will be designed to specifically bind each bioanalyte at SERS active hot spots providing ultra-sensitive detection. Label-free, trace, and multiplexing detection of bioanalytes using Raman spectroscopy can provide clear advantages over traditional, modestly selective, methods which require complicated and time-consuming labeling and processing procedures.

2.2 Objectives

In this comprehensive study, the two tasks will be accomplished through the following specific ***technical objectives***. Details regarding the two specific tasks to be addressed are described in detail below and are summarized in Figures 2.1 and 2.2.

Task 1:

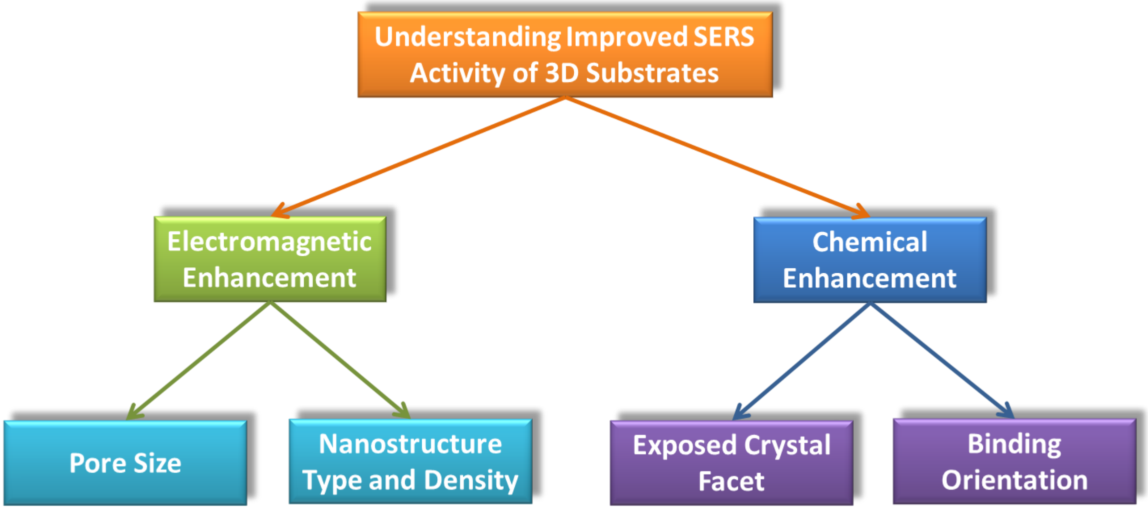

Figure 2.1 Schematic illustrating the motivation, goals, and specific areas of interest for task 1.

- *Synthesize metal nanostructures with sizes, shapes, and compositions suited for an enhanced SERS effect in a controlled aggregated state within cylindrical nanopores; experimental efforts will be guided by finite element modeling of electromagnetic field distribution in nanostructure junctions.*

- *Develop a fundamental understand of SERS phenomena including electromagnetic and chemical enhancement mechanisms occurring with 3D SERS substrates through testing small organic species and common Raman markers.*
- *Chemically modify the inner walls of nanopores with functionalized, self-assembled, and polyelectrolyte monolayers designed to tether and encapsulate nanostructures and their aggregates.*
- *Study the effects of pore dimensions and nanostructure location (depth in the pore) on the overall SERS enhancement.*
- *Determine optimal binding orientations and how this affects the Raman spectra of the target analyte and how to tailor binding of specific targets.*

Task 2:

- *Selection of important and relevant biomarkers, including stress-related small molecules as well as immunoglobulins and neuropeptides that are critical in many physiological processes.*
- *Synthesis of metal nanostructures of different sizes, shapes, and compositions as well as their functionalization with biorecognition elements such as aptamers or short peptides that will impart specificity and selectivity for the biomolecule target.*
- *Assembly of functionalized metal nanostructures into well-designed and uniform structures such as dimer aggregates or micropatterned arrays in order to provide repeatable and highly sensitive Raman hot spots.*
- *Design and test biological SERS sensor arrays to verify target specificity, binding affinity, and limit of detection for label-fee, trace biosensing.*
- *Establish key scientific principles for the future design of a robust platform for the trace detection of multiple vital biomarkers to improve field-grade biodetection systems.*

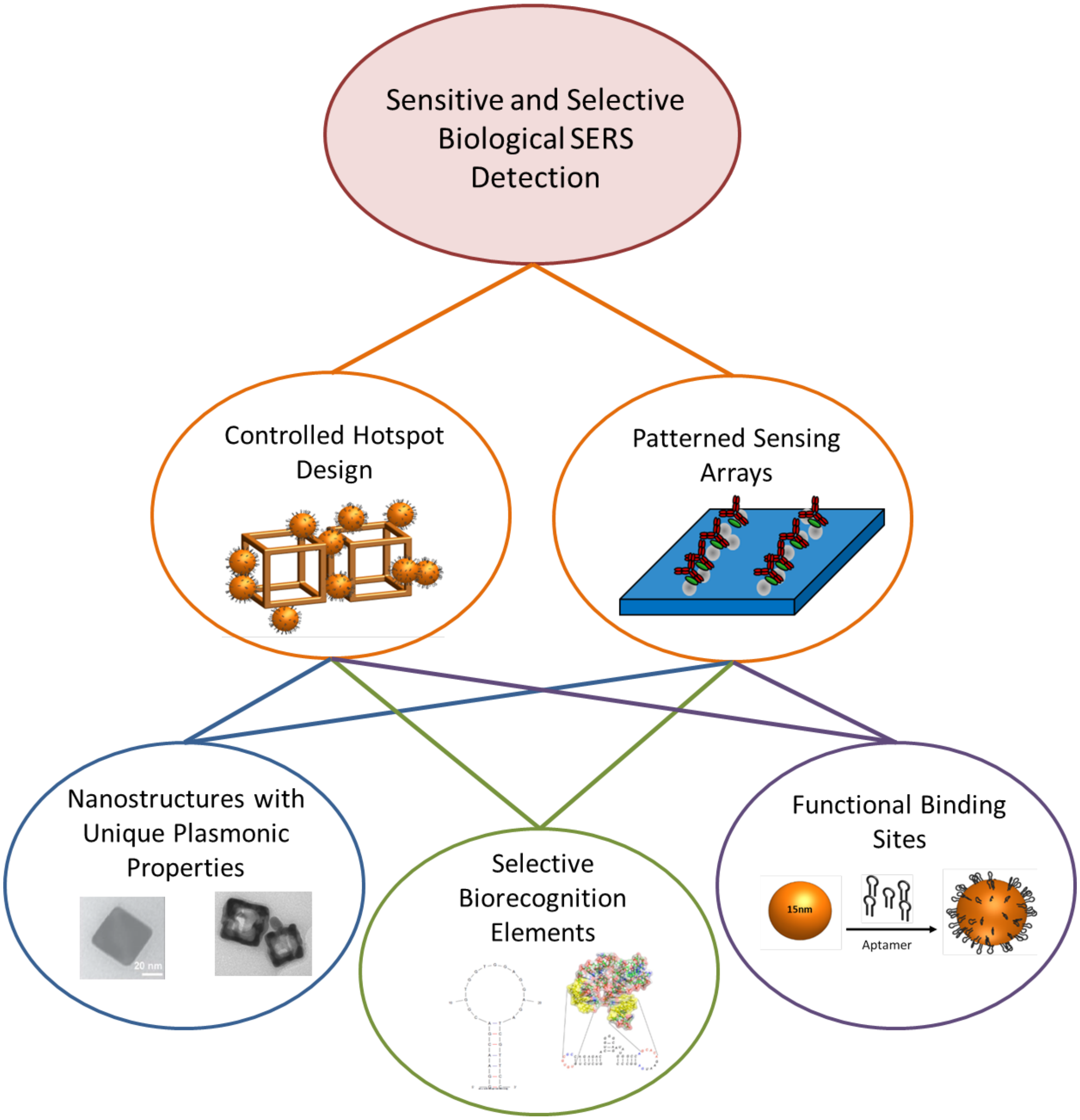

Figure 2.2 Schematic illustrating the motivation, goals, and specific areas of interest for task 2.

A deeper understanding of the underlying principles that drastically affect the enhancement mechanism of surface-enhanced Raman scattering is of particular importance as the complexity and capability of sensors designs progresses. The transition of the field of Raman spectroscopy from simple carbon materials and chemical analytes to larger more complex biomolecules elucidates more obstacles for sensor design, but also allows for advancements in label-free and sensitive detection in the traditional arena of biological diagnostics. The two tasks described in this study focus on the critical enhancement phenomena in new three-dimensional substrate designs and also provide new, highly specific and sensitive, and functional biological SERS sensor designs utilizing advanced biorecognition elements for important classes of biomolecules.

The significance of this study is that, first, we will show that there are critical design criteria for highly sensitive three-dimensional SERS substrates that can be probed and verified using conventional spectroscopic techniques and the substrate behavior can be predicted using electromagnetic modeling methods. Through the unique application of both well-developed and novel surface modification techniques as well as complex nanostructure fabrication methods, sensors can be developed that possess extremely high enhancement, recyclability, functionally target-specific binding sites, varied environmental exposure options, and high-throughput flowing capabilities.

Second, we will demonstrate that the principles learned from the detailed analysis of electromagnetic and chemical enhancement mechanisms can be applied to the developing field of SERS sensors for biological detection. This includes the selection of biomarkers for detection, the specific functionalization of nanostructure surfaces with targeted biorecognition elements, the assembly of nanostructures so to create well-designed and uniform hot spots for target binding, as well as the characterization and eventual Raman detection of the targeted analytes. This study will provide unique insight into new techniques for targeted label-free detection as well as significant information regarding binding affinities, orientations, and limits of detection of important biomarkers.

2.3 Organization and composition of dissertation

Chapter 1 is a critical review of issues and state of the art research related to current biological detection methods and proper SERS substrate design, prospective sensor design solutions and approaches for biological detection along with the challenges limiting their use. This chapter also includes a detailed review of metallic nanostructures (composed of silver and gold) as well as biomarkers that are important for the detection and monitoring of stress-related and other physiological processes as well as state of the art biorecognition elements that can be used for their specific detection which are all components of the motivation for the sensors designed in this study. Also discussed are the critical issues with current SERS substrate designs and the motivation for the research described in this work.

Chapter 2 is a concise description of the goals and technical objectives of the work presented in this dissertation. Furthermore, it provides a brief overview of the organization of the dissertation, with brief descriptions of the contents of each chapter.

Chapter 3 discusses the experimental techniques materials that played a critical role in the studies presented in this dissertation. It includes materials synthesis and functionalization of metal nanostructures, three dimensional porous substrate fabrication, and microscopic and spectroscopic characterization techniques. The various techniques that were used for the synthesis of both gold and silver nanostructures of different shapes and sizes, as well as the synthesis procedures for making highly ordered porous alumina membranes with different pore sizes are discussed. Also included are the detail procedures for the biofunctionalization and surface modification of metal nanostructures to allow for tailored surface chemistries. Characterization techniques include atomic force microscopy for measuring topography of substrates and nanoparticle size, confocal

Raman spectroscopy for analyte detection, UV-Vis-NIR spectroscopy and optical and fluorescent microscopy for measuring and imaging optical properties of nanostructures and substrates, scanning and transmission electron microscopies for imaging nanostructures and different substrates, zeta-potential and quartz crystal microbalance for monitoring surface functionalization of nanostructures and binding of biomolecules, and x-ray photoelectron spectroscopy to understand chemical compositions. In several subsequent chapters the experimental techniques are supplemented with specific protocols used for the particular studies presented.

Chapter 4 relates to the detailed study of the electromagnetic enhancement SERS effects within a silver nanostructure decorated porous alumina substrate. We demonstrate a comprehensive approach which includes the combination of light absorption, transmittance, and silver nanoparticle placement and can be utilized to dramatically maximize the 3D SERS enhancement of cylindrical nanopores. We demonstrate that this SERS substrate design has a record enhancement factor close to 10^{10}, which is very uniform (± 25%) across the membrane surface, and can be achieved through increasing the light transmittance by tuning nanopore diameters (up to 355 nm) and having predominant sub-surface nanoparticle placement within first 10-14 µm of the pore depth. This was determined by measuring and comparing the enhancement performance of substrates with different pore diameters and relating these measured observations to modeled enhancement predictions. The improved SERS activity is attributed to the enhanced transmission of light that facilitates the excitation of hot spots at greater depths within the substrate. These substrates were demonstrated to be able to detect a record vapor phase limit of 3 ppb n-methyl-4-nitroaniline, a common binder and stabilizing agent that can off-gas from plastic elxpolives.

Chapter 5 reports on PAMs with assembled metal nanostructures that are shown to be efficient three-dimensional substrates for SERS-based applications. In this study, we demonstrate our approach to dramatically improve the efficiency of PAM-based SERS substrates by tuning light absorption, transmittance and deposition of silver nanoparticles on cylindrical nanopores. SERS substrates with high SERS activity is achieved by increasing light transmission through the SERS substrates by varying the pore diameter (from 100 to 355 nm) and predominant deposition of silver nanoparticles in the first few microns (10-12 µm) of the membrane pores. SERS substrates with larger pore diameters exhibited higher SERS response compared to membranes with smaller pore diameters. The SERS substrates with larger pore diameter showed a high Raman enhancement factor (EF) of $\sim 10^{10}$ and $\sim 10^{6}$ with high uniformity (±25 %) for the common, non-resonant benchmark Raman analyte (benzenethiol) and non-resonant small molecule (perchloric acid), respectively. Electromagnetic and density functional theory simulation provided insight into the SERS phenomena that occurred in 3D PAM-based SERS substrates. The electromagnetic simulation suggests that the interaction of excitation light with the nanoparticles along the pore walls can be modified by tuning the pore sizes and high Raman enhancement can be achieved with membranes of ~400 nm pore diameters. Quantum chemical simulation of perchloric acid bound to nanostructured silver surfaces of different sizes and binding sites provided information regarding the orientation of molecules on the silver nanostructures and chemical enhancement mechanism towards SERS. Experimental results coupled with electromagnetic simulation studies enabled us to explain the observed high SERS activity which is attributed to the improved transmission of light (above 50%) and its interaction with nanoparticles facilitated by the substrates with large pore diameters.

In **Chapter 6,** we demonstrate a nanoengineered substrate composed of micropatterned silver nanoparticles to be used for the label-free mapping of adsorbed biomolecules. We utilized surface-enhanced Raman scattering (SERS) to monitor the known bioanalytes, protein A and human immunoglobulin G (IgG). The SERS substrate was composed of a poly(alylamine hydrochloride) (PAH)/poly(styrene sulfonate) (PSS) layer-by-layer (LbL) nanocoating micropatterned with silver nanoparticles confined to microscopic stripes. Selective adsorption of biomacromolecules is facilitated by the amine-terminated LbL nanocoating, which prevents the surface adsorption of positively-charged protein A across the surface except on the patterned regions containing negatively-charged silver nanoparticles. Furthermore, adsorption of IgG on predetermined regions is facilitated by the selective binding of the Fc region of IgG to protein A. This label-free SERS approach provides accurate, selective, and fast detection of protein A and IgG solutions with a nanomolar concentration, down to below 1 nM for IgG in solution. This method could also be utilized for the facile detection of proteins in field conditions as well as in clinical, forensic, industrial, and environmental laboratories.

In **Chapter 7**, we report on the assembly of gold nanoframe dimers assisted by aptamer-functionalized smaller spherical gold nanoparticles as prospective SERS biotraps for riboflavin, an important molecule for biological electron transfer reactions. In this approach, the aptamer-coated gold nanoparticles designed for selective binding of riboflavin also serve as the electrostatic driver for nanoframe dimerization in dilute solutions. The gold nanoframe dimers provide a unique condition for plasmonic coupling in a hot spot with sufficient space for the binding of bulky biomolecules. The use of an aptamer allows for highly selective binding of the targeted analyte as compared to conventional organic ligands with an excellent low detection limit of one micromol of riboflavin.

Finally, **Chapter 8** provides general conclusions for the overall work in the dissertation with a specific focus on impact and future directions.

CHAPTER 3

EXPERIMENTAL DETAILS

The following chapter is intended to provide a brief description and experimental details for the techniques and instruments used throughout this work.

3.1 Synthesis and fabrication

The bulk of this research relies on the accurate and homogeneous synthesis of gold and silver nanostructures as well as the substrates that they are deposited on. For this reason, a detailed description of the experimental procedures used in our lab as well as our collaborators for the synthesis of nanostructures, nanostructure surface functionalization techniques, and porous alumina membrane synthesis.

3.1.1 Spherical silver nanoparticle synthesis

Silver nanoparticles were synthesized by the photoreduction of $AgNO_3$ in the presence of sodium citrate by irradiation with ultraviolet light at room temperature producing monodisperse 33 ± 5 nm silver nanoparticles.[230] 42.5 mg of $AgNO_3$ and 73.5 mg of sodium citrate were dissolved in 250 mL of Nanopure water (18 MΩ cm) and an ultraviolet lamp (λ = 365 nm) was used as the light source for the reduction process with an exposure time of 8 hours. The silver nanoparticles were then centrifuged at 6,000 RPM for 10 minutes to remove excess reactant from the nanoparticle solution and redispersed in water.

3.1.2 Silver nanocube synthesis

The silver nanocubes were prepared as follows: 35 mL of ethylene glycol (EG) is heated to 150 °C for 1 hour with constant stirring. The temperature and stirring were held constant during the synthesis procedure. 10 mL of EG containing 0.25 g of polyvinyl pyrrolidone (PVP) (molecular weight of ∼55 000 g) was then added, followed by the addition of 0.4 mL of sodium sulfide (3 mM) dissolved in EG. 3 mL of silver nitrate solution in EG (282 mM) was injected into the reaction mixture to prepare nanocube templates with edge lengths of 50 nm.[231,232] The reaction was complete after 10 minutes and a nontransparent solution was formed. The silver nanocubes were washed by dilution with deionized (DI) water (Purelab ultra ELGA) and acetone, followed by centrifugation at 10,000 RPM for 5 minutes. The resulting precipitate was then dispersed in water.

3.1.3 Spherical gold nanoparticle synthesis

Spherical gold nanoparticles were synthesized using the seeded growth approach as has been previously reported.[109] Small gold seeds (<5 nm) were made in a 20 mL aqueous solution of 2.5 x 10^{-4} M trisodium citrate and 2.5 x 10^{-4} M $HAuCl_4$ with the addition of 0.6 mL of ice-cold, freshly prepared 0.1 M $NaBH_4$. The solution was allowed to react for 2 hours before use as the seed solution for subsequent particle formation. A 200 mL aqueous solution of 2.5 x 10^{-4} M $HAuCl_4$ and 0.08 M cetyltrimethylammonium bromide (CTAB) was prepared as a stock growth solution. Two flasks were labeled A and B and used for step-wise particle growth. In vial A, 9 mL of growth solution was mixed with 0.05 mL of 0.1 M ascorbic acid then 1 mL of seed solution was added with stirring and allowed to react for 30 minutes. In vial B, 9 mL of growth solution was mixed with 0.05 mL of 0.1 M ascorbic acid then 1 mL of solution A was added with stirring and allowed to react for 30 minutes. This procedure resulted in spherical gold nanoparticles with diameters of 15 ± 2 nm.

3.1.4 Gold nanoframe synthesis

A galvanic replacement technique was used to synthesize gold nanoframes from silver nanocube silver nanocube templates.[233] The silver nanocube solution was then used to prepare gold nanoframes. The purified nanocube solution was heated with stirring until it began to boil. A 10 mg/L hydrogen tetrachloroaurate solution was then injected into the boiling solution slowly until the absorption spectrum of the solution shifted to approximately 960 nm which corresponds to gold nanoframes with about 50 nm edge lengths with rounding. [234,232] The gold nanoframes were cleaned by centrifugation at 10,000 RPM for 5 minutes followed by dispersion in water.

3.1.5 Gold nanocube synthesis

Gold nanocubes were synthesized using an adapted seeded growth procedure that has been detailed previously.[235] A 10 mL seed solution was made containing 2.5 x 10^{-4} M $HAuCl_4$ and 0.1 M cetyltrimethylammonium chloride (CTAC). To this solution, 0.45 mL of an ice cold 0.02 M $NaBH_4$ was added and the resulting solution immediately turned brown and was allowed to age for 30 minutes. The seeds were shown to be 3-5 nm in diameter before use in subsequent synthesis steps.

Growth solutions were prepared in two vials labeled A and B. Each growth solution had a total volume of 10 mL and contained 0.1 M CTAC, 250 µL of 0.01 M $HAuCl_4$, and 10 µL of 0.01 M NaBr. Finally, 90 µL of 0.04 M ascorbic acid was added. Upon the addition of the ascorbic acid, each solution transitioned from gold to clear indicating the formation of ionic gold. Next, 25 µL of the seed solution was added to vial A, then 10 seconds later, 25 μL of vial A was added to vial B and allowed to react for 30 minutes. The reaction was stopped and the particles were washed by centrifugation at 10,000 RPM for 10 minutes.

3.1.6 Synthesis of porous alumina membranes

A detailed discussion on the fabrication of porous alumina membranes (PAMs) has been reported in the literature.[118,236] Synthesis of the PAMs with different pore diameters (100, 255, and 355 nm) was conducted by using oxalic acid and phosphoric acid as the electrolytes to achieve different pore diameters. In a typical synthetic procedure, prior to anodization, high purity aluminum (99.999%) sheets were degreased with acetone and electropolished in a 4:1 solution of 62% perchloric acid and ethanol at 7°C. The electropolished aluminum sheets were then subjected to the first anodization for 8 hours in appropriate electrolytes at an appropriate anodization voltage. The porous layer formed during the first anodization was selectively removed in a mixed solution of chromium oxide and phosphoric acid at 70°C for approximately 1 hour. The second anodization was performed in a similar manner as the first anodization step for 4-10 hours.

Porous membranes with pore diameters of ~40 nm were synthesized in a 0.3 M oxalic acid solution at 15°C and an applied voltage of 40V. PAMs with ~100 nm pore size was achieved by widening or controlling the resulting membrane using a 5 wt% phosphoric acid solution for 25 min at 35°C. The phosphoric acid treatment also results in pore opening of the bottom side to create through pores in the membranes. Synthesis of PAMs with pore diameters of 255 nm was carried out by following two-step anodization process in different electrolytes. The first anodization was done in 0.3M oxalic acid at 14°C for 8 hours followed by the second anodization in 10 wt % phosphoric acid for 10 hours at

120 V and 1°C. PAMs with 355 nm pore diameter was synthesized in phosphoric acid electrolyte at 160 V and 4°C. A solution of $CuCl_2$ (2g) in a water-hydrochloric acid mixture (50:50 v/v) was used to dissolve the residual aluminum to obtain free-standing membranes. Subsequently, the bottom side of the PAM was opened by chemical etching using 0.1 M aqueous NaOH. The pores of the membrane were filled with polystyrene to prevent uncontrolled pore widening during the etching process. The bottom sides of the PAMs are opened to facilitate faster diffusion of analytes through the membranes.

3.1.7 Electroless deposition of silver nanoparticles

Silver nanoparticles were immobilized on the pore walls of PAMs of varying pore size in accordance with the literature reported earlier[67] by immersing the PAMs in an aqueous solution of $SnCl_2$ (0.02 M) and HCl (0.01 M) for 2 minutes depositing Sn^{II} on the pore walls. The PAMs were rinsed in nanopure water and subsequently in acetone and dried. Then the PAMs were immersed in a 0.02 M aqueous solution of $AgNO_3$ for 2 minutes to deposit Ag nanoparticles on the pore walls followed by a second washing step. The deposition of silver nanoparticle seeds was carried out three times to provide a high degree of particle coverage on the pore walls. The PAMs were then immersed in 1 ml of 10 mM $AgNO_3$ and 0.5 ml of 100 mM ascorbic acid in order to grow silver nanoparticles from the deposited seed. The PAMs were removed from the solution and rinsed with nanopure water after different times after 28 minutes to achieve optimal nanoparticle size and density.

3.1.8 Biorecognition element functionalization of nanostructures

In order to functionalize metal nanostructures with aptamers, peptides, and other short biological ligands, a standard procedure was adopted from literature.[237] The number of aptamers needed per particle was dependent on the size of the nanostructures and was estimated from literature values.[238] The key to the nanostructure functionalization is the thiol-metal interaction of the ligand and nanostructure. Initially, the dithiol terminal end of the aptamer was activated by mixing 9 µL of 1 mM aptamer solution, 1 µL of 500 mM acetate buffer (pH 5.2), and 1.5 µL of 10 mM of tris-(2-carboxyethyl)phosphine hydrochloride (TCEP) and incubating the solution at room temperature for 1 hour followed by washing. This process cleaved the stable dithiol terminal group of the aptamer and created a thiol functional group for binding to metal nanoparticles. Next, the aptamer solution was added to 3 mL of nanoparticle solution and allowed to react for 20 minutes. The pH and salt concentration of the solution was change by adding 5 equal aliquots of 100 mM phostphate buffer (pH 7.4) and 2 M sodium chloride every 20 minutes with stirring while adding in order to prevent nanoparticle aggregation. The solution was then allowed to react in the dark overnight for at least 16 hours.

The reaction solution was then centrifuged at 15,000 RPM for 10 minutes and resuspended in half the volume of 10 mM phosphate buffer (pH 7.4). This process functionalized the surface of the nanoparticles with a high density of aptamers, but in order to provide enough room for aptamer activity, the surface was thinned with a separate procedure. A 4 µM solution of 6-mercaptohexanol (MCH) was prepared and 28 µL of this solution was added for every 1 mL of nanoparticle solution and allowed to react for 30 minutes. The remaining MCH was removed by added an equal volume of ethyl acetate and vigorously mixing. After the solution phase separated, the MCH-containing ethyl acetate layer was removed and the nanoparticle-containing buffer remainder was left. This process was repeated three times and then the nanoparticle solution was centrifuged three times at 15,000 RPM and resuspended in 10 mM phosphate buffer.

3.2 Characterization techniques

This research is highly dependent on the application of a wide range of characterization techniques for the comprehensive study of physical and chemical properties of different materials. A variety of techniques were used to determine detailed information about the structure and composition of the structures synthesized and used in this work. The accurate characterization of the nanostructures, substrates, and target analytes is an extremely critical part of this research and therefore the techniques used to do this will be discussed in detail with an emphasis on particular methods that are important for the work described.

3.2.1 Atomic Force Microscopy (AFM)

Tapping mode was commonly used for surface characterization and done using the Dimension 3000, Multimode, and Icon AFMs (Bruker AXS, Santa Barbara). This technique relies on a micro-fabricated tip that deflects a focused laser when interacting with the sample surface. This deflection is detected by optical methods onto a photodiode position sensor that can translate both normal and lateral deflection signal. The result is a three-dimensional map of the sample surface with nanometer resolution allowing for quantitative analysis of the surface roughness.[239] Tapping mode AFM allows for the high resolution imaging of soft polymeric and biological samples without damage to tip or sample since contact with the surface is minimized. This is achieved by using specially designed probes that oscillate above the surface at their resonant frequencies of 100-500 kHz.[240,241] It was particularly critical to use the extremely sensitive and accurate vertical resolution and phase resolution of tapping mode to determine the binding density and characteristics of proteins and other biological molecules on the surfaces of metal nanostructures. AFM characterization of the various nanostructures synthesized in these studies also provided an extremely accurate measurement of particle height as well as changes in particle height as a result of various surface modifications.

3.2.2 Confocal Raman Microscopy and Spectroscopy

Raman microscopy was used to understand and detect different analytes of interest by accurately assigning specific vibrational bands to chemical functionalities.[242] Confocal Raman microscopy was also used to study the plasmonic enhancement behavior of novel 3D surface-enhanced Raman scattering (SERS) substrates and monitor signal changes and uniformity through the depth of the substrate and over large areas using 2D surface mapping. Raman microscopy relies on vibrational spectroscopy which can provide chemical composition, structure of the material by monitoring the frequency shifts between excitation laser and scattered light. It has the potential to be one of the most important tools for characterizing and sensing biological, environmental, and chemical targets, primarily due to its non-destructive approach, presence of sharp bands, and high intensity of these characteristic bands. A WiTec (Alpha 300 R) confocal Raman microscope equipped with a Nd:Yag laser (514 nm) is employed for spectroscopic analysis of the various sensing substrates as well as bulk analyte reference spectra. The Raman microscope provides a lateral resolution of ~250 nm and vertical resolution of 1µm.[243] Confocal Raman images were acquired line by line with an Avalanche photodiode detector (APD) in the single photon counting mode by fast imaging with a 50x objective lens.

3.2.3 UV-Visible-NIR Spectroscopy

UV-Visible-NIR spectroscopy is an incredibly powerful tool for the characterization of plasmonic nanostructures in both the solution and dry state. This technique allows for the accurate determination of the extinction band location of different nanostructures which depends highly on the size, shape, and composition of the metallic nanostructures. Understanding the plasmonic peak location is critical for proper SERS measurements as the maximum enhancement occurs when the excitation wavelength source is in resonance with the plasmonic peak of the active nanostructures. For standard solution state UV-Vis measurements performed in this study, a Shimadzu UV-2450 spectrophotometer was used and spectra were recorded in 1.5 semi-micro plastic cuvettes (PlastiBrand, Germany). When longer wavelengths were needed, UV-Vis-NIR spectra of different nanostructures as well as the mixed aggregates in solution were recorded in 1.5 mL semi-micro quartz cuvettes using a Cary 5E UV-Vis-NIR spectrophotometer (Varian). Solution state aggregation of the nanostructures must often be measured with a longer wavelength instrument due to the highly red-shifted extinction behavior of coupled plasmonic bands. In order to study the coupled plasmonic behavior of aggregated nanostructures on 2D surfaces including micropatterned substrates, a Craic QDI 202 microscope spectrophotometer attached to Leica DM 4000M microscope with a 50x objective.

3.2.4 Optical and Fluorescence Microscopy

General optical and fluorescence microscopy were performed to analyze surface distribution of nanostructure aggregates, micropatterned samples, and protein binding distributions. Both techniques were performed using a Leica DM 4000M optical/fluorescent microscope and images were collected using a Leica DFC 480 camera. For fluorescent microscopy, a mercury lamp source was used with fluorescent filter cubes specific to the fluorophore.

3.2.5 Scanning Electron Microscopy (SEM)

Scanning electron microscopy was used to characterize several aspects of the SERS substrates and nanostructures such as nanostructure shape and size, porous alumina membrane pore size and uniformity, nanostructure density and aggregation state on substrates, and energy dispersive x-ray spectroscopy (EDS) can be used to determine chemical composition of the substrates and nanostructures. For general observation of the samples, a lower resolution Hitachi-3400 SEM was used with operating voltages of 5-10 keV. For high resolution imaging, a Zeiss Ultra60 SEM was used at an operating voltage of 5-10 keV. For samples that were not conductive such as porous alumina membranes, polymer-coated surfaces, or aptamer- or peptide-coated nanoparticles, a 5-10 nm layer of gold was sputtered using a Denton Vacuum Desk IV sputter coater operated at a current of 20 mamps and a pressure of 50 mTorr in an Argon environment.

3.2.6 Transmission Electron Microscopy (TEM)

Transmission electron microscopy is an extremely powerful technique that was used in this study to determine nanostructure shape, size, aggregated state, and compositional properties. The extremely high resolution provided by TEM allows for the determination of particle spacing, aggregation state, degree of cube edge rounding, and polymer shell thickness that no other technique can provide. For particle shape, size, and aggregated state, a Jeol 100CX TEM operated at 100kV was used. For high resolution imaging as well as crystallographic and diffraction studies of nanoparticles, an FEI Tecnai F30 TEM operated at 300 kV was used. This instrument was able to provide atomic resolution for determining which crystal faces of the silver and gold lattices were present at the surface of the nanostructures. Samples were prepared by dropcasting from dilute solutions onto 200 mesh copper TEM grids with a carbon-formvar support film (Ted Pella, Inc.). All samples were allowed to dry for at least 24 hours in order to ensure there would be no contamination of the TEM chamber or burning of the sample from the electron beam.

3.2.7 Zeta-potential and Dynamic Light Scattering (DLS)

Zeta-potential was used to determine the surface charge of the nanostructures used in this work. The surface charge is a critical property of the nanostructures that can determine both the interaction with other nanoparticles or surfaces, but also can be used as a metric for determining if proper nanostructure surface functionalization has been achieved when exchanging polyelectrolyte, surfactant, or aptamer and peptide ligands. Zeta-potential measurements were made at neutral pH, at 25°C, and with the Smoluchowski model using a Malvern Nano S Zetasizer with Malvern polystyrene disposable Zeta-potential cuvettes. The same instrument was also used for dynamic light scattering measurements of the nanostructures using disposable polystyrene 1.5 mL microcuvettes (PlastiBrand, Germany) and measurements were made with the 173° backscatter detector. These measurements provided the hydrodynamic diameter of the nanostructures and allowed for an estimation of the binding state of the surface ligand in solution (fully extended or collapsed) as well an estimation of the aggregated state of mixed particle solutions.

3.2.8 X-ray Photoelectron Spectroscopy (XPS)

Thermo k-alpha XPS was used to understand the composition of 3D SERS substrates and the total number of silver nanoparticles bound to the substrate by monitoring the total amount of silver present. XPS is an analytical technique that directs a monochromatic beam of X-rays on a sample and detects the characteristic electrons that are ejected. The energies and number of electrons are used to determine the elements present, their abundance and chemical bonding state. This technique is highly surface sensitive and the typical detection depth is ~5nm. It can detect light elements such as Silicon at about 1%

of the total surface composition and heavier elements down to ~0.1% with an accuracy of 20-50% of the given value.[244]

CHAPTER 4

SERS EFFECTS IN SILVER-DECORATED CYLINDRICAL NANOPORES

4.1 Introduction

Surface-enhanced Raman scattering (SERS) has shown great potential for monitoring internal chemical composition, inner stresses, and trace detection of hazardous molecules that are otherwise difficult to detect by other experimental techniques.[150,151,152,153,154,155,156,157] SERS has become an area of intense research as a highly sensitive probe for the trace level detection of small organic molecules since the demonstration of single molecule detection.[20,22,147,148,149] For cutting-edge practical applications of SERS-active substrates, the sensitivity of planar metal structures remains rather low due to the limited density of hot spots available within the laser-activated footprint.[60,64]

Three-dimensional SERS substrates have been recently introduced which show great potential for increasing the level of enhancement for practical SERS detection due to the unique properties they provide in comparison to traditional planar substrates.[169,245] By extending the SERS substrates into the third dimension, a much greater surface area for particle coverage compared with traditional substrates is realized.[246,247] Several 3D SERS substrates suggested are photonic crystal fibers[248] porous membranes with cylindrical nanopores,[249] and periodic nanohole arrays.[250] Their high enhancement allows for the ultrasensitive detection of “stealthy”, non-resonant molecules.[68] Although the distribution of nanoparticles on templates via directed assembly is not as homogeneous as that observed for substrates microfabricated (pillars, holes) with micro[251] and nano[252] fabrication techniques, the overall SERS signal is very consistent, within 10% from specimen-to-specimen. However, this approach does not bear a huge burden associated with extremely high cost: many thousands of dollars for EBL nanostructures versus a few dollars for assembled nanoparticles as well as the relatively low surface area of microfabricated structures due to third-dimension expansion issues in all lithographic techniques.[246] In fact, even if enhancement factors for microfabricated substrates are higher than for regular planar substrates, common values average around 10^7.[253] Therefore, microfabricated lithographical substrates, which are important for fundamental studies, are not promising for practical applications with their current characteristics being a tremendous unresolved roadblock for further utilization.

Porous alumina membranes (PAMs) with long cylindrical nanopores decorated with metal nanoparticles are among the potential candidates for 3D SERS substrates with extremely high enhancement owing to their optical transparency in addition to their large specific surface area extended to a third dimension.[60,68] Moreover, open cylindrical pores facilitate the mass transport of analytes (gases and fluids) which is important for practical analysis. In addition, the incident beam can be directed deeper into the substrate through the waveguiding properties of nanopores (50-400 nm in diameter) facilitating added Raman signal enhancement.[182,183] Several PAM-based SERS substrates have already been studied and their high efficiency has been reported, but general design principles have not been established.[60,68,254,255,256,257] It has only been suggested that the transmission of incident light through holey substrates and proper placement of metal nanoparticles inside the pores play a vital role in achieving the highest efficiency, which is critical for ultrasensitive bio- and chemical detection.

Therefore, in this study we focus on the role of light transmission and its interaction with metal nanoparticles within cylindrical nanopores of different diameters and suggest general guidelines for the design of nanoporous substrates with the highest SERS activity. Here, we present simulations and experimental studies of substrates with different pore sizes decorated with in situ grown silver nanoparticles bound to the pore walls. We observed that SERS substrates with 355 nm pore diameters facilitate enhanced light transmission as well as nanoparticle aggregation that results in greatly improved SERS activity with an enhancement factor above 10^{10}, which is dramatically higher than that for traditional 2D substrates. Electromagnetic simulation of silver nanoparticle dimer clusters placed at different pore depths confirmed the experimentally observed pore diameter dependence. Simulation studies coupled with experimental results suggested that nanopore diameters of around 400 nm, the incorporation of nanoparticle dimers within the first 10 µm beneath the surface, and keeping light transmittance above 50% are all critical for the optimization of SERS substrates showing high enhancement factors exceeding 10^{10} for the selected benchmark Raman marker, benzenethiol (BT). The observed record enhancement factor is four orders of magnitude better than that commonly reported for this marker on 2D substrates of gold and silver nanostructures.[258,259,260]

4.2 Experimental details

Information regarding the fabrication of porous alumina membranes with different pore sizes, synthesis of and deposition of different metal nanostructures, and characterization through UV-Vis spectroscopy, AFM, SEM and Raman spectroscopy can be found in Chapter 3.

The simulation studies were carried out by our collaborators (R. J. C. Brown et al.) using the following experimental details. The simulations were designed by considering silver nanoparticles of 40 nm diameters in aluminum oxide pores with 10 nm walls, parameters close to our experimental parameters. In all cases nanoparticle dimers have been considered as these will dominate the maximum response seen for such a system. Dimers have been modelled at various depths within the pores and in the center of the pore.

Various pore widths have also been considered. The polarization of the incoming radiation (at 514 nm) was in the incident plane to ensure excitation of the surface plasmons. Widely- published optical data for silver and aluminum oxide were used to input properties into the modelling.[261] The incident electromagnetic field in the complex-field representation can be written as:

$$\mathrm{E}(\mathbf{r},t) = \mathrm{E}_0 \exp(i\mathrm{k}\cdot\mathbf{r} - i\omega t) \tag{1}$$

$$\mathrm{H}(\mathbf{r},t) = \mathrm{H}_0 \exp(i\mathrm{k}\cdot\mathbf{r} - i\omega t) \tag{2}$$

where $\mathrm{E}(\mathrm{r},t)$ and $\mathrm{H}(\mathrm{r},t)$ and the electric and magnetic field components, respectively, at location $\mathbf{r}$ and time t; E_0, and H_0 are the electric and magnetic field amplitudes, respectively, k is the wavevector, and ω is the angular frequency of the wave. In the absence of nonlinear optical effects and when only the elastic scattering process is considered, the electromagnetic fields surrounding the scatterers must be self-consistent, leading to the conditions:

$$\mathrm{E}(\mathbf{r},t) = \mathrm{E}_{\mathrm{in}}(\mathbf{r},t) + \mathrm{E}_{\mathrm{sc}}(\mathbf{r},t) \tag{3}$$

$$\mathrm{H}(\mathbf{r},t) = \mathrm{H}_{\mathrm{in}}(\mathbf{r},t) + \mathrm{H}_{\mathrm{sc}}(\mathbf{r},t) \tag{4}$$

where the subscripts in and sc denote the incident and scattered waves respectively. The electromagnetic waves must satisfy Maxwell's equations within the modeling domain, and adhere to the boundary equations at the interface between the media and the scatterer, leading to the conditions:

$$\nabla \times (\nabla \times E) - \omega^2 \varepsilon \mu E = 0 \quad (5)$$

$$\nabla \times (\nabla \times H) - \omega^2 \varepsilon \mu H = 0 \quad (6)$$

$$(E_2(\mathbf{r}) - E_1(\mathbf{r})) \times \mathbf{n} = 0 \quad (7)$$

$$(H_2(\mathbf{r}) - H_1(\mathbf{r})) \times \mathbf{n} = 0 \quad (8)$$

where the ε and μ are the complex valued permittivity and permeability and $\mathbf{r}$ is on the boundary of the scatterer, and $\mathbf{n}$ is a unit vector orthogonal to the boundary. The field distribution must be a solution of these equations.

Finite element methods (FEM) using Comsol Multiphysics software[262] have been employed to provide numerical solutions to these equations for each substrate with common practices used for FEM studies of the field enhancement and spectral response in the vicinity of rough surfaces[263] and nanoparticles.[264] The FEM methodology requires the creation of a ‘radiation boundary condition’ or ‘absorption boundary condition’ to truncate the modeling scenario into a confined domain. The ‘perfect matched layer’ (PML) boundaries method[265] has been used for this simulation. This matches the optical index at the interface of the media and attenuates the wave quickly within the artificial layer so that little or no electromagnetic radiation will be reflected back into the domain of scattering. Additionally, a low-reflection boundary condition is applied at the outer PML boundary in order to minimize residual reflection. In this way the possibility of artifacts occurring in the modeling output is minimized.

The output of the modeling process is a two-dimensional map of the electric field intensity which can be used to calculate the Raman enhancement $G_{(r,\omega)}$ using:[266]

$$G_{(r,\omega)} = \left| \frac{\hat{E}_{loc}}{\hat{E}_{free}}(\omega_L) \right|^2 \left| \frac{\hat{E}_{loc}}{\hat{E}_{free}}(\omega) \right|^2 \tag{9}$$

Where ω_L and ω are the frequencies of the incident and scattered light respectively; $\hat{E}_{loc}$ and $\hat{E}_{free}$ are the absolute values of the local vector potentials (normalized to the intensities of the incident and scattered light) in the presence, and absence, respectively, of the substrate. When the polarization of the scattered light is the same as that of the incident light, the expected electromagnetic enhancement of the Raman signal may be expressed to a first approximation (for example Otto,[266] Pendry,[267] and Kneipp[22]) as:

$$G_{(r,\omega)} = \left| \frac{E_{(r,\omega)}}{E_{inc(\omega)}} \right|^4 \tag{10}$$

where $E_{(r,\omega)}$ is the total predicted electric field at position r, and $E_{inc(\omega)}$ is the electric field associated with the incoming electromagnetic radiation. The interpretation of this quantity for the work here is given as the average value for $G_{(r,\omega)}$ obtained in a 5 nm^2 area in the region containing the maximum enhancement observed in the model. Validation of the modeling procedure was carried out against published data,[268] in particular, Garcia-Vidal's implementation of Maxwell's equations on adaptive meshes for the study of the interaction of light with metals surfaces[267] and with Xu et al.'s study of colloid particle shape and size on the electromagnetic enhancement factor using classic electromagnetic theory.[24] In these cases the methodology used here produced comparable enhancement factors to those predicted by Garcia-Vidal for structured metal surfaces for incident wavelengths of light between 310 and 620 nm. The modeling used here also produces results that are comparable to Xu et al.'s predictions of enhancement factors for spherical particle substrates with separations of 1 nm and 5 nm to within an order of magnitude. This level of agreement with published data from two quite different studies confirms the applicability and flexibility of the modeling methodology used here for predicting Raman enhancement factors. Taking this data into consideration, the uncertainty in the predicted Raman enhancement data, within and between modeling scenarios, is approximately one order of magnitude.

4.3 Results and discussion

4.3.1 Substrate fabrication and optical properties

In order to systematically study the effect of pore diameter on the SERS activity, we have synthesized PAMs with different pore diameters ranging from 100 to 355 nm following a two-step anodization process[118,236] (see Chapter 3 for more details). In this study we have used an in situ 'electroless-deposition' growth method[67] to obtain a uniform distribution of silver nanoparticles on the pore walls as shown in Figure 4.1. This technique provides a uniform deposition of highly dense and aggregated silver nanoparticles throughout the depth of the substrate and without the requirement of an organic capping agent using a direct reduction method.

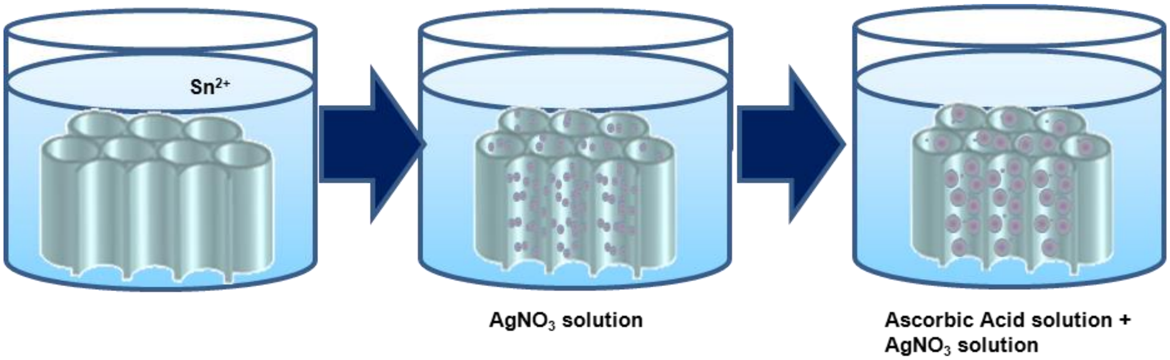

$$Sn^{2+}\,(aq) + 2\,Ag^{+} \rightarrow Sn^{4+}\,(aq) + 2\,Ag\,(s)$$

Figure 4.1 In situ electroless deposition of silver nanoparticle seeds and overgrowth of nanoparticles in porous alumina membranes.[67]

Indeed, high resolution SEM images of the fractured substrates with pore diameters of 355 nm show a distribution of immobilized silver nanoparticles on the inner walls (Figure 4.2a). Particles with smaller sizes that can be seen on the pore walls are initial silver seeds with a diameter of around 5 nm pre-deposited for the growth of silver nanoparticles. It was demonstrated earlier that PAMs decorated with silver seeds did not show significant SERS activity.[67] The size of grown silver nanoparticles and their aggregates estimated from the atomic force microscopy (AFM) and SEM images are 30 ± 10 nm (Figure 4.2b). Although for smaller pore diameters predominantly individual nanoparticles are observed, PAMs with larger pore diameters facilitate the aggregation of

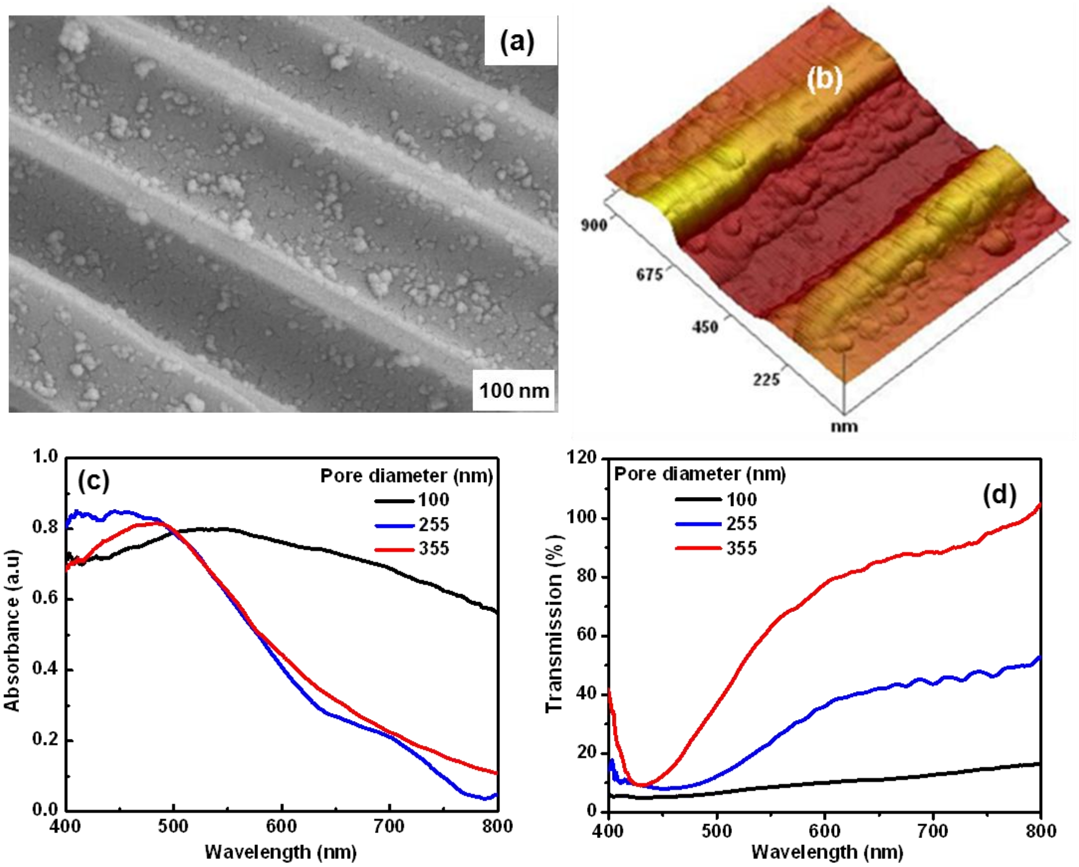

Figure 4.2 (a) SEM image and (b) AFM image of silver nanoparticles grown in porous alumina membranes with 355 nm pore diameters. (c) UV-vis absorption and (d) transmission spectra of porous alumina membrane-based SERS substrates with different pore diameters.

silver nanoparticles on the pore walls with predominantly dimers (about 60 nm) formed in additional to individual nanoparticles.

The optical absorption centered at 486-530 nm for the nanoparticle-decorated PAM substrates is caused by the surface plasmon resonances (SPR) of silver nanoparticles (Figure 4.2c).[67] The maximum absorption occurred at a longer wavelength as compared to SPR for a single nanoparticle (420 nm for silver nanoparticles of 30 nm diameter in solution)[269] suggesting the formation of silver nanoparticle aggregates, which was indeed confirmed by SEM images (Figure 4.2a). The UV-vis absorption spectra of the SERS substrates of varying pore size overlap with the excitation wavelength of the incident light thus providing efficient conditions for 514 nm excitation.[36] On the other hand, the transmission of light through the SERS substrates is the highest in the near-IR range and remains high in the visible region (Figure 4.2d). SERS substrates with 355 nm pore diameters show the highest transmission in the visible region, around 50% at the excitation wavelength of 514 nm. The reflectance spectra of the neat PAMs show almost similar reflectivity, irrespective of the pore diameters and thus no calibration was done in the Raman measurements.

4.3.2 Confocal Raman mapping and spectral analysis

The SERS activity of the substrates was tested using BT as a common benchmark Raman marker.[178] The SERS activity of the substrates is found to increase dramatically as the pore diameter increases from 100 to 355 nm as evidenced by the rise in relative intensity of the characteristic peaks of the BT molecules as will be discussed below. To understand the enhancement pattern, we elucidated the 3D distribution of SERS activity of cylindrical pores by conducting complete Raman mapping in both the (x,y)-plane and the z-direction (Figures 4.3a, 4.3b). The mapping was conducted by monitoring the

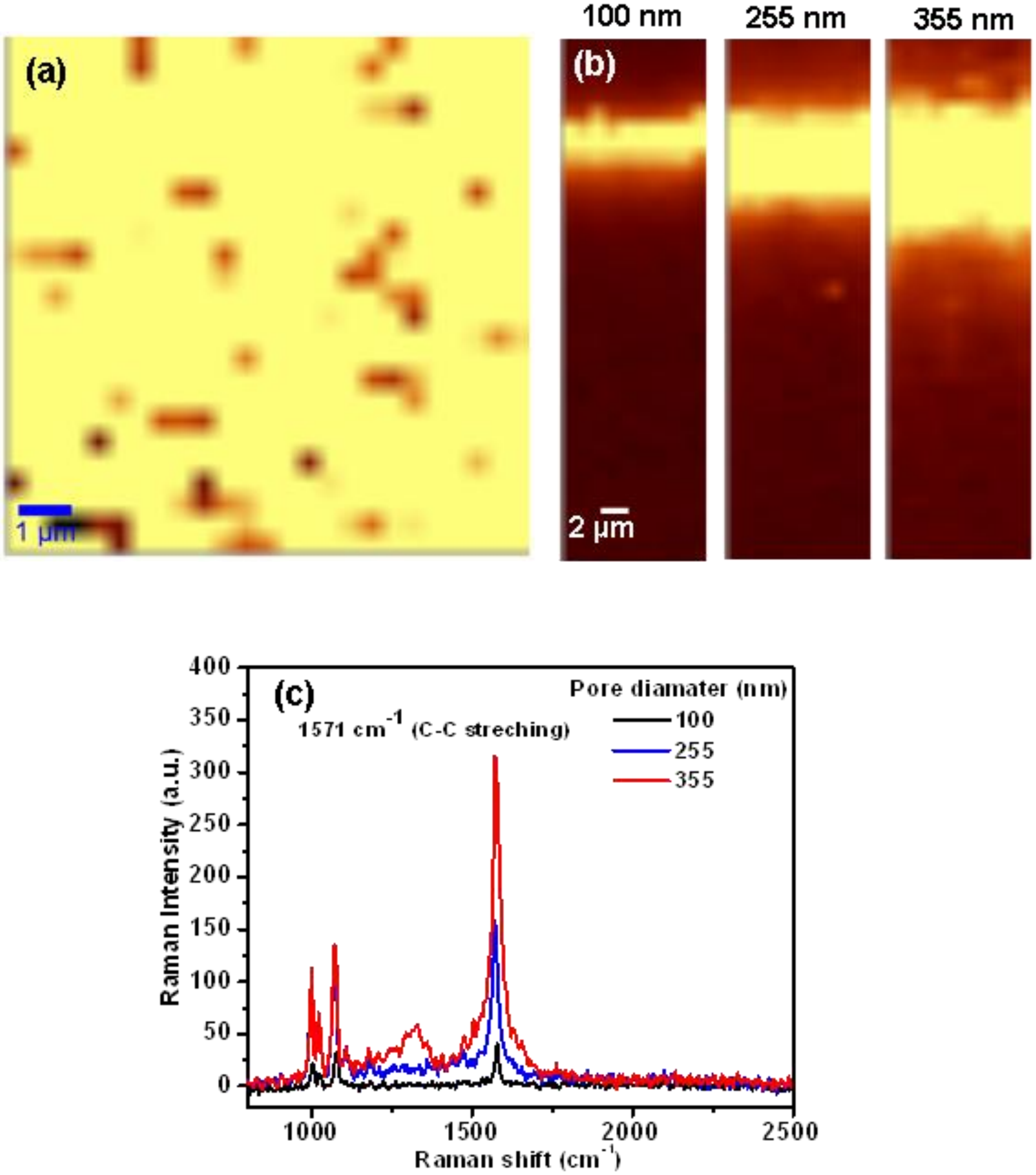

Figure 4.3 (a) Surface (x,y) Raman mapping of the 1571cm^{-1} peak of benzenethiol for substrates with 355 nm pore diameters. (b) Confocal SERS mapping of the 1571 cm^{-1} peak of 10^{-6} M benzenethiol through the depth of the porous alumina membranes with different pore diameters (pore dimension is shown on the corresponding z-profile). (c) SERS spectra of benzenethiol obtained at ~ 5 µm depth of the PAM-based SERS substrates.

intensity of the 1571 cm^{-1} peak (caused by symmetric C-C stretching of BT molecule) through the depth of the nanopores. The (x,y) distribution of the SERS signal for 10 µm x 10 µm surface collected for pore diameters of 355 nm is presented in Figure 5.3a. As apparent from the 2D Raman map, uniform SERS enhancement occurs over the entire region of the substrates with SERS intensity varying from pore-to-pore within ± 25 %.

To further check macroscopic uniformity of the SERS substrates and different batches, reproducibility of SERS activity from different positions (at least 10 positions) of multiple substrates of the same pore diameter (355 nm) was measured for a laser footprint below 1 µm across. The SERS intensity was found to be very reproducible at different locations within a substrate and from the different substrates (within ± 7%) which indicates high homogeneity of the SERS substrates despite the variation of local aggregated morphology and the presence of residual seeds.

On the other hand, z-mapping of SERS activity of different nanopores shows that the largest SERS enhancement occurs within the first 10 µm of depth directly beneath the membrane surface region (Figure 4.3b). The SERS intensity of BT gradually decreases as the depth of measurement increases for all pore diameters. SERS spectra of BT obtained at approximately 5 µm depth from top surface of the PAM show consistent spectra with diminishing Raman band intensity (Figure 4.3c). To confirm the presence of a BT surface layer in the SERS substrates, fractured SERS substrates (cross-sections) were analyzed using X-ray photoelectron spectroscopy (XPS). Quantitative estimation of surface coverage was found to be impossible because of inhomogeneity of the fractured surface structure; however, signals corresponding to BT were detected from the fractured samples. The XPS spectrum of the carbon (1s) and sulfur (2p) collected for SERS substrates with 355 nm pore diameter confirms the presence of BT layer inside pores. The major photoemission occurs at 284.1 eV and is attributed to indistinguishable phenyl group carbon atoms and the minor peak at 288.6 eV is due to carbon connected to an electronegative sulfur atom.[270,271] The two peaks are assigned to the $2p_{3/2}$ and $2p_{1/2}$ spin-orbit split levels with binding energies of 163.3 and 167.2 eV, respectively.[270,271] An example of a typical XPS spectrum from these fracture PAMs with benzenethiol can be seen from a subsequent study in Figure 5.6.

4.3.3 Pore size comparison and electromagnetic modeling

The electromagnetic SERS enhancement through the cylindrical pores was further simulated by using silver nanoparticle dimers placed at various depths. Silver nanoparticle dimers were selected to reflect the common geometry of aggregates inside pores and these dimers were placed in the pores with an orientation that provides maximum enhancement between nanoparticles (see "hot spot" in Figure 4.4a). Dimers are selected because this is the predominant type of aggregate and dimers with other orientations and separations provide minor contributions. The modeling we have performed is limited to two dimensions. Therefore we did not model larger aggregates than dimers because there is no way to arrange particles in two dimensions and create a larger enhancement that closely approaches that of two particles. Even in three dimensions, it is difficult to arrange spherical particles so more than two touch in any one location. To have three or more nanoparticles meeting at a single location requires non-spherical particles. The enhancement predicted here corresponds to the enhancement levels reported earlier for silver dimers.[272,273]

These simulations showed that the cylindrical pore acts to constrain the incident radiation in a manner such that the maximum enhancements can be realized at a certain pore diameter and at a certain depth (Figure 4.4b). As the pore diameter increases, the electric field in the interparticle gap increases and the highest field intensity is achieved for about

400 nm pore diameter. Moreover, a series of electromagnetic field peak intensities is observed along the main axis of the cylindrical pores with spacing close to $\lambda/2$. It is also evident from Figure 4.3b that significant electromagnetic enhancement occurs for nanoparticles dimers placed continuously at several microns beneath the surface, which is in good agreement with the experimental z-mapping of the enhancement factor (Figure 4.3b). The Raman enhancement factor gradually increases with the accumulated addition of nanoparticle dimers along the pore depths (Figure 4.4c). The simulated accumulated enhancement factor shows saturation at depths higher than 10 µm. Consistent with simulations, experimental observation confirms that the membranes with 355 nm pore diameters show increasing SERS activity with saturation at depths of 10-14 µm (Figure 4.4d).

For the direct calculation of the experimental enhancement factor, we utilized a common approach which compares the intensities of major Raman bands for solutions with known concentrations with and without the SERS substrate. This method assumes that all molecules in the solution migrate from the solution to the substrate in the course of solvent evaporation. As is well understood, this method underestimates the actual enhancement because only a fraction of molecules from the solution actually end-up on silver nanoparticles with higher affinity to thiolated analytes and thus, the number reported here represents only the lower bound of true values which can be in fact many fold higher. But even this lower bound value is significantly higher than that reported for ordered microfabricated lithographical SERS substrates with average values around 10^7 and the highest enhancement of 10^9 reported for localized highly enhancement obtained without averaging over the total surface or volume.[213,251,253,274,275]

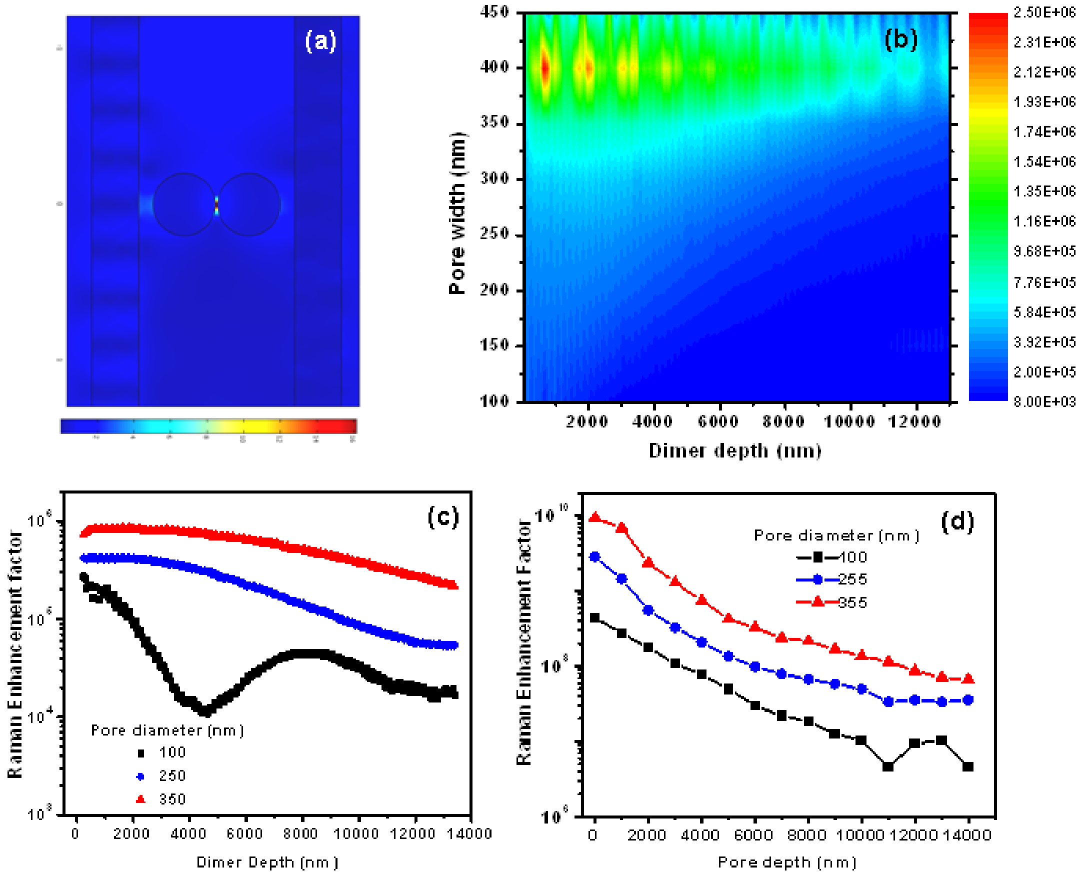

Figure 4.4 (a) Electric field distribution for silver nanoparticles of 40 nm diameter with a separation of 1.5 nm placed in an alumina membrane with pore diameter of 100 nm. The nanoparticles were excited by sending 514 nm light from the top of the pore with a polarization parallel to the long axis of the dimer. (b) Simulated field intensity for a silver nanoparticle dimer as a function of pore diameter and pore depth. (c) Variation of simulated Raman enhancement factor for membranes with different pore diameters (100, 250, and 350 nm) and particles located along the pore wall. (d) Raman enhancement factor extracted from the experimental z-mapping and its variation with depth from surface.

General behavior for all pore diameters is similar, but 355 nm pores show the highest enhancement factor which is an order of magnitude higher than that obtained for substrates with 100 nm pore diameters. As clear from the data, general trends observed in experiments and obtained in simulations are similar considering the limited z-resolution of the Raman mapping of about 1 μm. However, the experimental enhancement factor is more than two orders of magnitude higher than that calculated in simulation from electromagnetic field distribution. This increase can be attributed to the additional contribution from chemical enhancement (which can reach 10^3) for benzenethiol molecules chemisorbed on silver nanoparticles, which is not accounted in the simulation.[276]

4.3.4 Vapor phase detection using silver nanocubes

Three-dimensional porous alumina substrates also showed potential as a vapor phase detection platform. For this application, four substrates were compared using different fabrication mechanisms included vacuum infiltration of silver nanocubes (AgNCs) after different PAM surface treatments (Figure 4.5a) and electroless deposition of silver nanospheres (AgNSs) (Figure 4.1). Analysis of the SEM images of the PAH, PEI, and (PAH-PSS)-coated substrates in Figure 4.5b, c, and d (respectively) shows a dense distribution of AgNCs over several microns depth from the top surface of the PAM. Figure 4e is an SEM image of the PAM-AgNS fabricated by the electroless deposition method, showing a uniform deposition of quasi-spherical nanoparticles over the entire PAM.[69,277] The high adsorption of particle density of AgNC on the pore walls is due to the strong electrostatic attraction between the positively-charged polyelectrolyte layer and the negatively-charged PVP-coated AgNCs. The majority of AgNCs in the PAH and PEI substrates are assembled in many-particle densely-packed aggregates, which leads to enhancements in the SERS response through the presence of SERS hot spots between

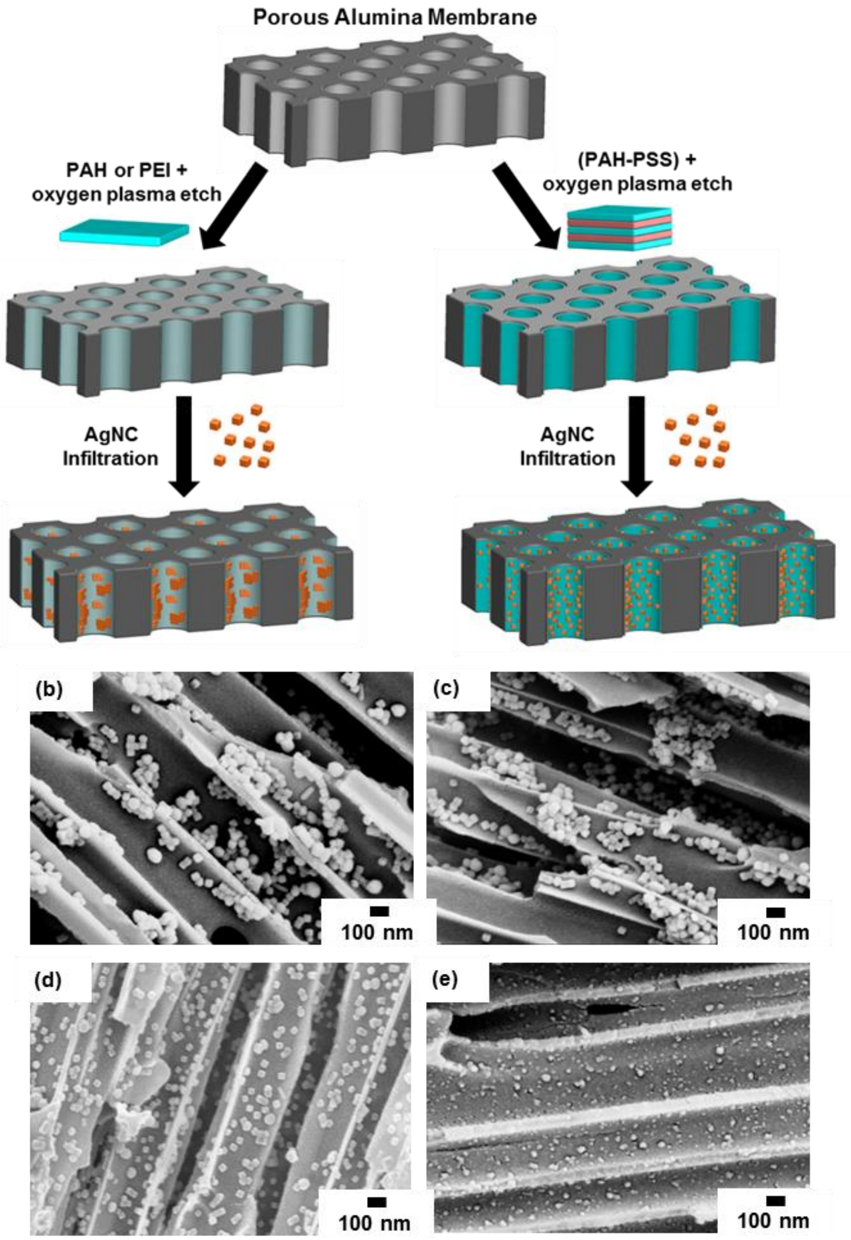

Figure 4.5 (a) Schematic of the AgNC infiltration method showing the porous alumina membrane coated with a positively charged polyelectrolyte (PAH and the PAH-PSS bilayers) that is subsequently decorated with silver nanocubes by infiltration. SEM images of the cross section of the infiltrated substrates (b) PAM-AgNC (PAH), (c) PAM-AgNC (PEI), and (d) PAM-AgNC (PAH-PSS). (e) SEM image of the cross section of the PAM-AgNS substrate produced via the electroless deposition method.

closely adjacent nanocubes. The AgNC-(PAH-PSS) substrate on the average demonstrates single and smaller AgNC aggregates that are more dispersed than the PAH and PEI substrates. This difference in adsorption behavior is likely due to the PAH and PEI substrates not having as uniform a polymer layer over the pore surface area after the oxygen plasma etching process, while the (PAH-PSS) substrate has multiple bilayers that are electrostatically bound which are more resistant to oxygen plasma etching.

The presence of aggregates in the (PAH-PSS) substrate can be explained by shielding of the repulsive electrostatic interaction between PVP-capped AgNC by the highly positive terminating cationic polymer layer (PAH) on the PAM pore walls which minimizes the repulsive electrostatic interaction between adjacent PVP-coated AgNCs,[278,279] potentially allowing for AgNC to adsorb close to each other via Van der Waals interactions. In addition, it is evident from Figure 4b, c, and d that the majority of the AgNC aggregates assemble with a face-to-face orientation which is due to Van der Waals attractions having a stronger influence over assembly orientation than steric hindrance between PVP chains of adjacent AgNCs, an expected result for particles stabilized with short-chain polymers.[70]

The SERS substrates were exposed to six different n-methy-4-nitroaniline (MNA), an important binder and stabilizing agent in plastic explosives, vapor concentrations that were established using specific temperatures: 3 ppb (5 °C), 10 ppb (15 °C), 29 ppb (25 °C), 99 ppb (35 °C), 297 ppb (45 °C) and 790 ppb (55 °C),[280] a procedure similar to previous studies.[281] The ppb vapor concentration of MNA was calculated using theoretical calculations of the MNA vapor pressure at different temperatures and by assuming ideal gas conditions (applicable given the low pressure and temperatures involved) as is standard practice for parts per vapor concentration estimations.[280]

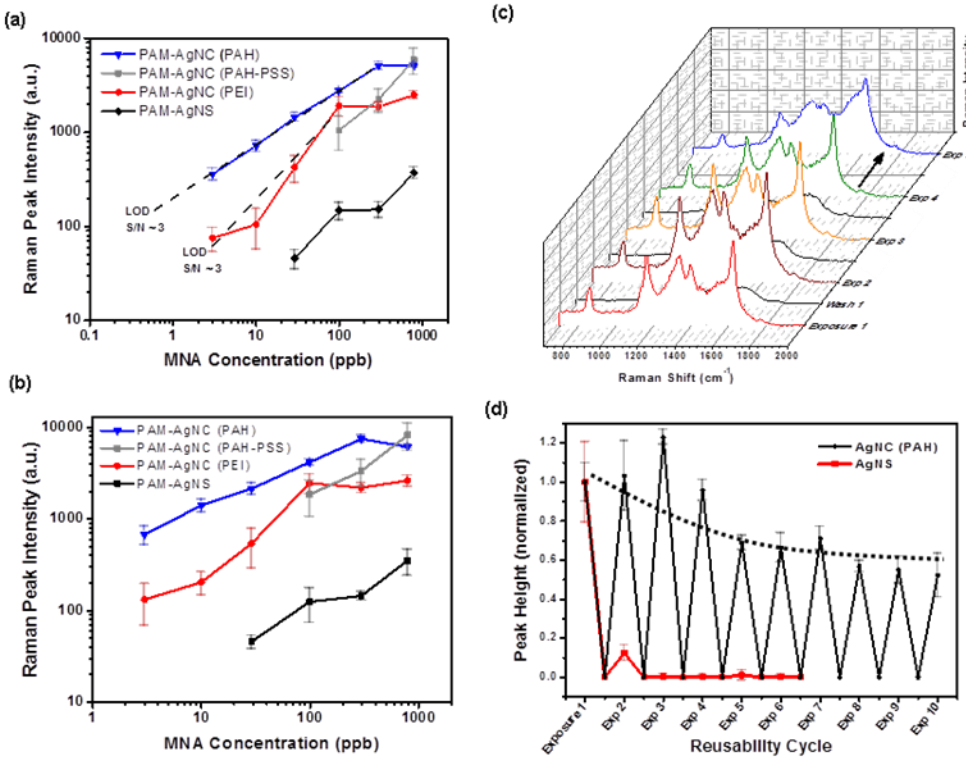

Figure 4.6 Variation of the SERS intensity versus concentration between the PAM-AgNC (PAH), PAM-AgNC (PAH-PSS), PAM-AgNC (PEI), and PAM-AgNS substrates for the (a) 857 cm^{-1} and (b) 1157 cm^{-1} peaks. (c) SERS responses of PAM-AgNC during repeated MNA exposure-ethanol washing cycles (the sample was exposed to MNA vapor created at 45°C). (d) The normalized SERS response of the 857 cm^{-1} peak through multiple exposure-wash cycles (the dotted line is a visual aid, not a fit). The AgNC (PAH) and AgNS SERS response were normalized according to the intensity of the 857 cm^{-1} peak during the first MNA exposure for each substrate.

Variation of the Raman intensity of the 857 and 1157 cm^{-1} peaks with MNA vapor concentration is shown in Figure 4.6a and b. This figure shows that the Raman intensity of the peaks increases with MNA concentration until they saturate at 300 ppb and 100 ppb for the PAM-AgNC (PAH) and PAM-AgNC (PEI) substrates, respectively. It is also shown that MNA vapor concentrations of approximately 3 ppb can easily be detected by the AgNC-(PAH) and (PEI) substrates by identifying either the 857 or 1157 cm^{-1} peak, where a signal-to-noise ratio of at least 3 was used to identify peaks. This is a record level of detection for MNA in the vapor phase. Neither the AgNS nor the AgNC-(PAH-PSS) substrate demonstrates saturation for the concentration range studied.

This is likely due to the more dispersed adsorption pattern of the nanostructures which leads to a larger effective surface area. Therefore, the AgNC (PAH) and (PEI) substrates are very effective for low ppb detection, but are unable to distinguish between higher vapor concentrations, while the AgNC-(PAH-PSS) and AgNS substrates demonstrate the ability to distinguish between higher ppb concentrations. The ability to change the adsorption behavior of AgNC can therefore offer a means to tailor the substrate's effective concentration response which is an important, but commonly overlooked, substrate parameter.

The reusability of the substrates was also investigated by exposing the substrates to multiple MNA exposure-ethanol wash cycles. The AgNC substrates were found to be robust against solvent washing and could be readily reloaded for repeated tests. Figure 4.6b and c show the SERS response of the substrate which was exposed to MNA at 45°C after repeated MNA exposure-ethanol washing cycles. The SERS activity of the substrate was monitored by tracking the peak intensity of the 857 cm^{-1} peak (Figure 4.6b). The SERS activity remained consistent in the first four repeated measurement-washing cycles and was then found to decrease and finally stabilize in the subsequent cycles. The reduction in intensity is likely due to the removal of lightly bound, physically adsorbed AgNCs during the washing steps. This is further supported by the apparent leveling of the SERS intensity (at later washing steps), which likely occurs as the loose AgNCs are removed and the total number of AgNCs approaches a constant value. A baseline intensity of < 2 % was observed after each washing step.

Overall, the current study provides an example of a comprehensive approach that considers the transmission of light and the aggregation of nanoparticles confined in cylindrical pores toward designing highly optimized 3D SERS substrates with enhancement factors several orders of magnitude higher than that of traditional planar substrates or non-optimized porous substrates. Also demonstrated is the ability of these substrates to have a tuned density of silver nanocubes and nanospheres for the record trace detection of vapor phase important analytes.

CHAPTER 5

COMBINING THE THIRD DIMENSION WITH CHEMICAL ENHANCEMENT FOR TRACE CHEMICAL DETECTION WITH SERS

5.1 Introduction

For practical applications of SERS-active substrates, the sensitivity of planar metal structures remains modest due to the limited concentration of hot spots available within the laser-activated footprint.[60,64] 3D substrates show a great potential for increasing the level of enhancement for SERS detection due to the unique properties they provide. By extending the sensing device into the third dimension, a much greater surface area for particle coverage compared with two-dimensional (2D) substrates is realized, which could provide opportunities for a greater degree of interaction between hot spots and the incident beam as well as more binding sites for probing molecules. As a result, 3D substrates fabricated with different metallic nanostructures can be considered as efficient SERS substrates for the detection of trace amount of analyte molecules of interest. Efficient 3D SERS substrates have been fabricated using different methods such as deposition of silver nanostructure on gold supported polyaniline membranes.[247] Fabrication of periodic 3D metal nanostructures with nanoporosity via colloidal crystal templates was demonstrated in another study[246] and the resulting structure showed higher SERS activity compared to the 2D counterpart. Recently Lee et al. have shown that variety of 3D nanoparticle structures deposited from charged aerosols exhibit enhanced SERS efficiency.[282] Photonic crystal fibers[283] and porous membranes possessing cylindrical nanopores decorated with different metallic nanostructures[249] and periodic nanohole arrays[250] have also attracted great attention due to their large SERS enhancement.

Porous alumina membranes (PAMs) formed by the anodization of aluminum, have been used in the fabrication of many functional materials for many years because of their unique nanostructures.[284] The geometrical characteristics of the PAMs (pore diameters, pore spacings, and membrane thicknesses) can be controlled by employing different anodization conditions such as anodization voltage and the electrolytic solution used in the process.[119] Porous alumina membranes are ideal host templates to understand the optical properties of metallic nanostructures because of their optical transparency over a wide range of wavelengths.[285] PAMs decorated with metal nanoparticles are potential candidates for the fabrication of 3D SERS substrates owing to their optical transparency in addition to the large specific surface area of their 3D geometry. The incident beam can be directed deeper into the substrate through the waveguiding properties of alumina[182,183] adding another element to increase the Raman signal enhancement. It has been previously demonstrated that efficiency of a PAM-based SERS substrate decorated with gold nanoparticles in the label-free molecular level detection of plastic explosive materials such as dinitrotoluene and trinitrotoluene down to the ppt level. The detection limit is more than four orders of magnitude better than the previously reported detection limit.[68]

The high efficiency of the PAM-based SERS substrate was attributed to the large specific surface area of the porous alumina membrane coupled with the optical waveguiding effect of alumina pore wall. In addition to the aforementioned effects, the transmission of the incident light through the PAM-based substrates was also found to play a vital role in achieving improved efficiency.[68] In this context, we envisaged that the waveguiding effect of the alumina, propagation of light and transport of analytes through the membranes may be modified by tuning the pore diameter of the PAM. A general design principle has been demonstrated recently to improve the SERS activity of PAM-based SERS substrates with a common Raman marker benzenethiol.[277] It has been suggested that the transmission of incident light through the holey substrates and proper placement of metal nanoparticles inside the pores play vital roles in achieving the highest efficiency. Therefore, this study focuses on detailed investigation on the role of light transmission and its interaction with metal nanoparticles within cylindrical nanopores. In addition to this, understanding of the chemical interaction between the analyte and nanoparticle, binding sites and molecular orientation on the nanoparticle surface are very important in achieving high SERS activity and interpretation of the SERS spectrum.

We investigated the SERS efficiency of the substrates with different analytes such as benzenethiol (BT) and a non-resonant perchloric acid (PA). Based on the experimentation with PAMs of different pore sizes (100, 255, and 355 nm) decorated with in situ grown silver nanoparticles bound to the pore walls, we have found that SERS substrates with 355 nm pore diameter facilitate enhanced light transmission, that result in improved SERS activity with very high enhancement factor, which is several orders of magnitude better than that reported for traditional 2D substrates.[258,259,260] Electromagnetic simulation studies with silver nanoparticle dimer placed at different depth of alumina membranes using finite element methods (FEM) suggested that nanopore diameters of around 400 nm, incorporation of nanoparticles within first 10 µm beneath the surface of the PAM are critical for the optimization of PAM-based SERS substrates. This helps us in the fundamental understanding of SERS phenomenon that occurs in 3D nanoporous structures and optimization of pore diameter to achieve high SERS activity. Density functional theory (DFT) simulations of Raman spectra of PA on silver clusters of different sizes and geometries demonstrated the effect of chemical binding on Raman spectrum and lead us to get insight into the chemical enhancement mechanism towards SERS. In addition to this, the role of molecular orientation and adsorption site on SERS spectra provided a better understanding of the current experimental system. Fabrication of PAM-based substrates with optimal pore diameters with controlled molecular orientation improves the sensitivity of the current SERS substrates for the detection of hazardous chemicals and biomolecules.

5.2 Experimental details

A detailed discussion on the fabrication of porous alumina membrane (PAM) has been reported in the literature[118,236] and has previously been described in great detail in Chapter 3. Silver nanoparticles were then immobilized on the pore walls of PAMs following a two-step processe in accordance with the literature reported earlier[67] and described in Chapter 3. Since the electroless deposition method does not use any molecule or polymer as an adherent layer to bind the nanoparticles to the pore walls, the possibility of overlapping of the Raman bands of the binding layer and the analyte can be ruled out. This makes the method superior to other conventional methods such as vacuum infiltration of nanostructures through the membrane. PAMs with the silver nanoparticles were characterized using methods detailed in Chapter 3 including AFM, SEM, and high resolution TEM. XPS was performed according to Chapter 3 in order to determine the quantitative amount of silver nanoparticles in the cross-sections of the different pore size membranes.

Raman measurements were performed according to the typical procedure adapted in our laboratory (Chapter 3).[243] PA from water and BT from ethanol were deposited on the SERS substrates and Raman spectra were collected. Each spectrum was collected with 10 seconds of exposure time, and at least two exposures were averaged to ensure accurate spectra were recorded. Mapping images were acquired with a vertical resolution of about 1μm with a 50x objective lens. The UV-Vis absorption, transmission and reflectance spectra of the SERS substrates and neat PAMs were collected using a Craic QDI 202 spectrophotometer attached to a Leica microscope.

Simulation studies were carried out by considering silver nanoparticles of 40 nm diameters in aluminum oxide pores with 10 nm walls, parameters close to our experimental parameters. In all cases nanoparticle dimers have been considered as these will dominate the maximum response seen for such a system. Dimers have been modelled at various depths within the pores, and for two positions: (1) at approximately 1nm from the pore wall and (2) in the center of the pore. Various pore widths have also been considered. The polarization of the incoming radiation (at 514 nm) was in the incident plane to ensure excitation of the surface plasmons, and orthogonal to the line joining the centres of the nanoparticles in the dimers. Schematic diagram of the structures used for the simulation studies is shown in Figure 5.1. Light was always parallel to the long axis of the dimer.

DFT simulations were also completed for the Raman spectrum of perchloric acid with the initial silver cluster geometries taken from the Cambridge Cluster Database[286] and optimized at the B3LYP/6-31+G(d) level using Gaussian 09.[287] The different perchloric acid-silver cluster geometries (PA-Ag_n n= 2, 6, 10, 18 and 20) were re-optimized at the same level of theory and then the relaxed coordinates of the combined system are obtained and used in our study. Tentative peak assignment was carried out by comparing mainly the normal Raman spectrum with the DFT Raman spectra.

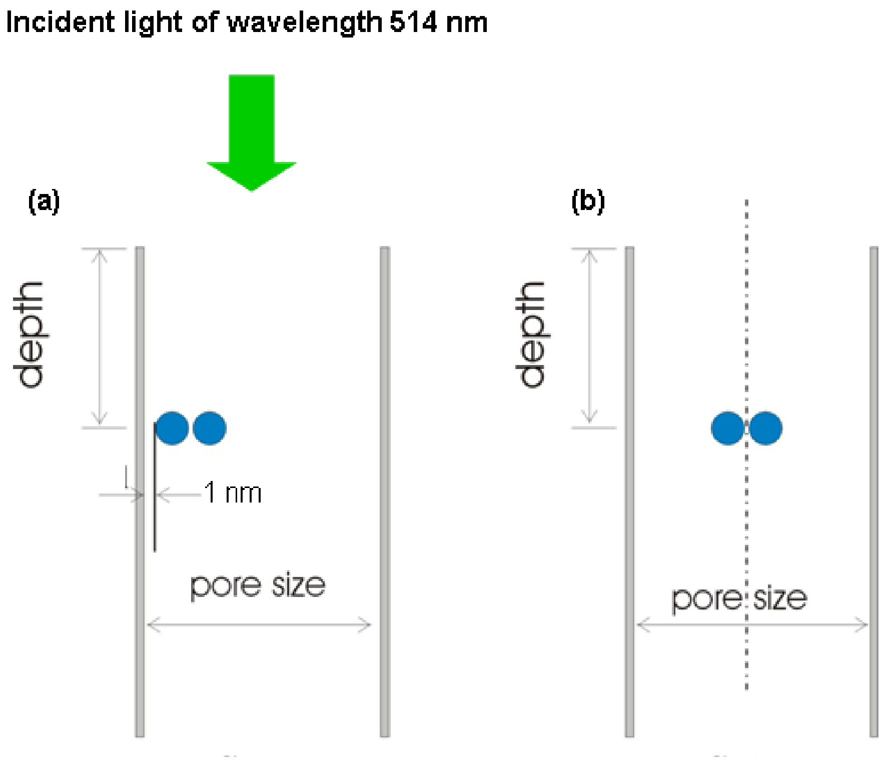

Figure 5.1 Schematic diagram of the geometries used for the simulation studies (a) dimers at the pore wall and (b) dimers at the center of the pore. The 'pore size' is the distance between the inner walls of the pore. In the situation where the dimer is close to the wall, the distance between the pore wall and the nanoparticle is 1 nm. The distance between the nanoparticle is 1.5 nm. The laser light with wavelength of 514 nm is incident from above, with its polarization parallel to the line joining the centers of the nanoparticles.

5.3 Results and discussion

5.3.1 SERS substrate fabrication

Figure 5.2 shows SEM images of PAMs with different pore diameters under different experimental conditions. The pore diameter variation of the membranes is between 7-10 % and the ordered domains extend over several microns. Immobilization or organization of metal nanostructures is very crucial in order to achieve intense Raman signal from the substrates which eventually makes the system more sensitive. In this study we have used a simple in situ growth method called ‘electroless- deposition’[67,288] to obtain a uniform distribution of the silver nanoparticles on the pore walls of the PAMs. A detailed growth mechanism and time dependence of particle size and distribution were reported in a previous report from our group.[67] In the current study, the deposition of silver nanoparticles was carried out for 28 minutes because it was found that PAM-based substrates containing silver nanoparticles grown for 25-30 minutes showed the largest Raman enhancement.[67]

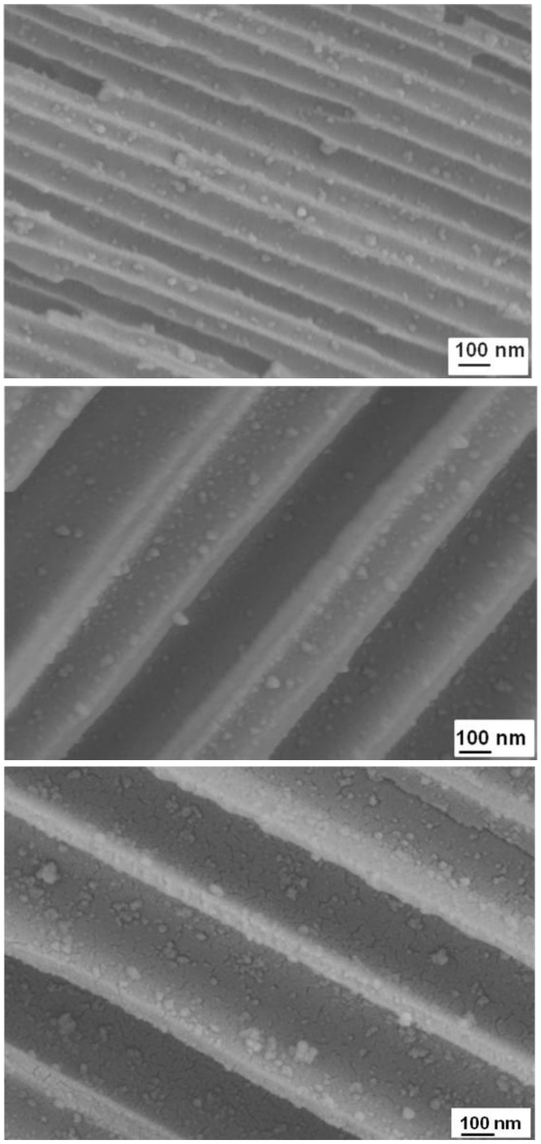

Figure 5.2 SEM images of silver nanoparticles grown on the porous alumina membranes (cross sectional view) of (a) 100 nm, (b) 255 nm and (c) 355 nm pore diameters.

High resolution SEM images of the cross-section of the SERS substrates show the distribution of immobilized silver nanoparticles on the inner walls of the membranes (Figure 5.2). As is clear from the SEM images PAMs facilitate a fairly uniform in situ growth of silver nanoparticles with particle diameters of 30 ± 10 nm along the pore walls. Particles with smaller sizes observed on the pore walls are initial silver seeds with a diameter of around 5 nm pre-deposited for the growth of silver nanoparticles. It was demonstrated earlier that PAMs decorated with silver seeds did not show significant SERS activity.[67] The size of grown silver nanoparticles and their aggregates estimated from the SEM image is 30 ± 10 nm. Although for smaller pore diameters predominantly individual nanoparticles are observed, PAMs with larger pore diameter facilitate aggregation of silver nanoparticles on the pore walls with predominantly dimers (about 60 nm) formed in additional to individual nanoparticles. The distribution of nanoparticles inside the membranes is not as homogeneous as that observed for substrates fabricated with micro[251] and nano[252] fabrication techniques. However, fabrication of SERS substrates using the above techniques is limited due to relatively high cost of fabrication, time consuming and the low surface area of the metal structures.[246] Since utilization of the lithographic techniques to assemble particles inside the membranes is extremely difficult, the SERS substrates fabricated by wet chemical approach ‘electroless deposition’ which we used in this study provide highly reproducible and stable SERS substrates which is necessary for using SERS in routine and on-line studies. Also, the electroless deposition method is inexpensive and fast compared to other fabrication techniques.

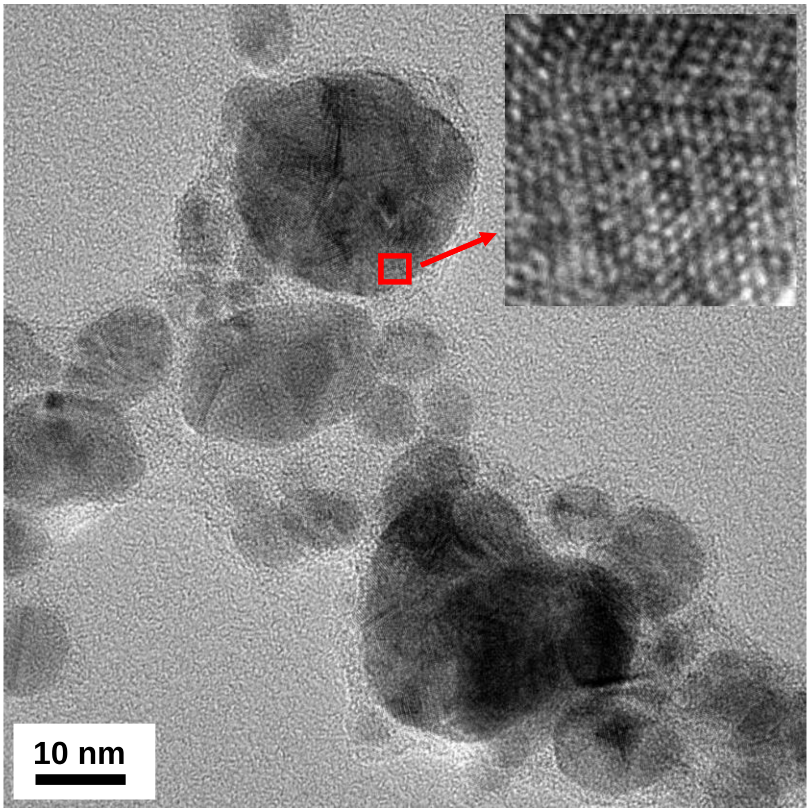

Figure 5.3 High resolution TEM image of electroless-deposited silver nanoparticles. Inset image shows the crystallographic planes in the silver nanoparticles.

The particle size was further confirmed from high resolution TEM images (Figure 5.3). Analysis of TEM images shows that presence of (111), (200), (220) and (311) crystallographic planes [289] of the face-centered cubic silver with (111) planes exposed at the surface. The interplanar distance corresponds to (111), (200), (220) and (311) is 2.3 Å, 1.9 Å, 1.4 Å and 1.2 Å respectively with a standard deviation of 0.1 Å. To characterize the nanostructured morphologies further, we conducted AFM imaging on a cross-section of the SERS substrate fabricated from a PAM with 355 nm pore diameters. The AFM image clearly shows the size and distribution of silver nanoparticles formed by in situ growth from the electroless-deposited seeds on the pore walls. The presence of nanoparticles and nanoparticle aggregates are clearly seen along the pore walls.

5.3.2 Optical plasmonic properties of SERS substrates

UV-vis absorption spectra and transmission spectra of the silver nanoparticle decorated PAMs with different pore diameters are shown in Figure 5.4. The optical absorption centered at 486-530 nm due to the surface plasmon resonance (SPR) absorption of silver nanoparticles indicates the presence of silver nanoparticles immobilized in the PAMs (Figure 5.4a). It has been shown that nanoparticle aggregation causes the SPR absorption to occur at longer wavelength due to dipole-dipole interactions between adjacent nanoparticles, resulting in the reduction of the plasmon frequency.[30] The typical plasmon band of approximately 30 nm AgNPs in solution is located near 430 nm.[269] A plasmon band that has been red-shifted for the same size of silver nanoparticles is indicative of coupled plasmonic behavior as the result of particle aggregation. The SPR absorption occurred at the longer wavelength (486–530 nm) suggest the formation of silver nanoparticle aggregates inside the pore walls; which is confirmed with the SEM images of the cross-sections of the substrates. The UV-vis absorption spectra of the SERS substrates show considerable absorption between 486-530 nm that overlaps with the excitation wavelength of the incident light thus providing for efficient excitation.[36] As a result, all the substrates are expected to show high SERS activity at an excitation wavelength of 514 nm.

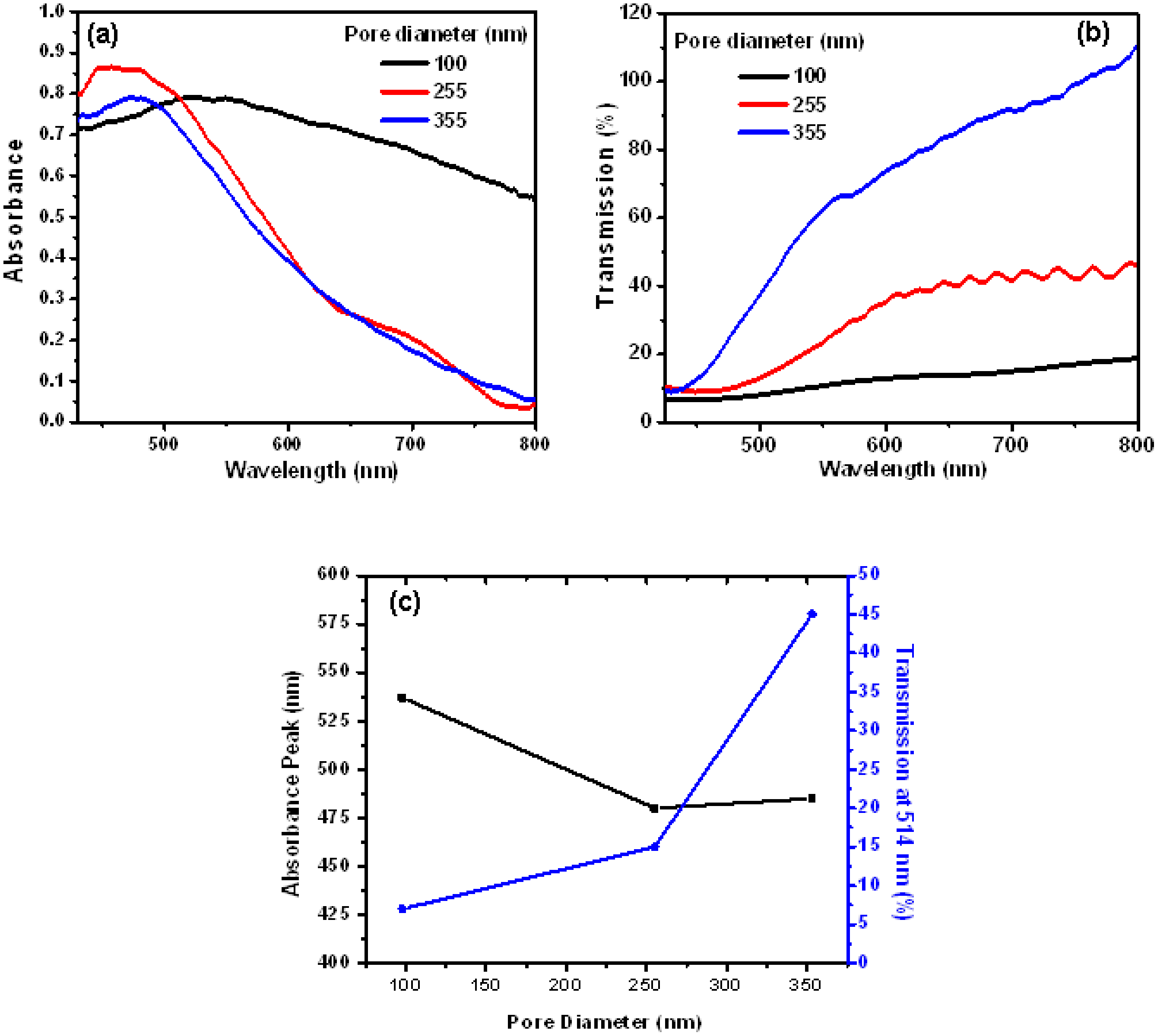

Figure 5.4 (a) UV-vis absorption and (b) transmission spectra of SERS substrates fabricated from porous alumina membranes with different pore diameters. (c) Variation of absorption maxima and transmission at 514 nm of SERS substrates with pore diameters.

The transmission of PAMs is relatively high in the near-IR range and decreases in the visible region because of scattering.[68] Surface plasmon mediated enhanced light transmission was observed in periodic arrays of metallic nanoholes[290] and ordered nanoporous-metal films.[291] Transmission spectra obtained for PAM-based SERS substrates with different pore diameters are shown in Figure 5.4b. The transmission of the SERS substrates decreases as the pore diameter decreases; SERS substrates with 355 nm pore diameters show the highest transmission in the visible region compared with smaller pore diameters. Variations of the transmission at 514 nm of the SERS substrates with different pore diameters are shown in Figure 5.4c. SERS substrates with 355 nm pore diameters exhibit transmission of approximately 50% at 514 nm while the substrates with smaller pore diameters show lower transmission (15 and 10% for SERS substrates with 255 and 100 nm pore diameters respectively). The transmissivity of the PAM-based substrates decreases at lower wavelengths due to the scattering and absorption of light by the substrate and the metal nanoparticles within.

5.3.3 SERS activity of silver-decorated PAMs

To evaluate the SERS activity of the PAM-based substrates, 10^{-6} M ethanolic solution of BT and 10^{-3} M aqueous solution of PA were deposited on each substrate. An excitation light source with a wavelength of 514 nm was employed for Raman measurements because the SPR absorption of the SERS substrates decorated with silver nanoparticles nearly overlaps with the wavelength of the excitation laser. Figure 5.5 shows the SERS spectra of BT and PA adsorbed on the substrates possessing different pore diameters. The SERS activity of the substrate exhibits a strong dependence on the pore diameter of the membranes. The characteristic SERS bands of BT (1571 cm^{-1}, due to phenyl ring stretching) and the PA (932 cm^{-1},due to symmetric stretching mode of Cl-O bond) are shown in Figure 5.5. The SERS activity of the substrates is found to be enhanced as the pore diameter increases from 100 to 355 nm as evidenced by the increase in relative intensity of the characteristic peaks of the analyte molecules BT and PA adsorbed on the substrates (Figure 5.5). Similar trend was observed for Rhodamine 6G deposited on each of the substrates. We suggest that the higher SERS activity of the PAM-based substrates is associated with the waveguiding effect as well as transparent nature of porous alumina membranes. The transmission spectra of the SERS substrates (Figure 5.4b.) indicates that light transmission is higher (50%) at 514 nm for the substrates with 355 nm pore diameters than that of the substrates with smaller pore diameters (100 and 255 nm).

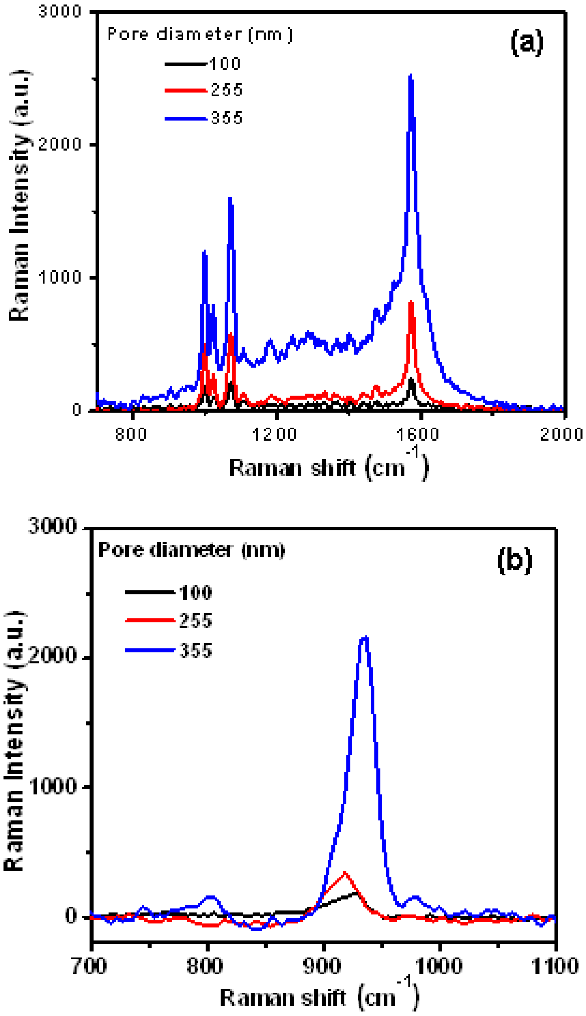

Figure 5.5 SERS spectra of (a) 10^{-6} M Benzenethiol, (b) 10^{-3} M Perchloric acid on each of the porous alumina membranes.

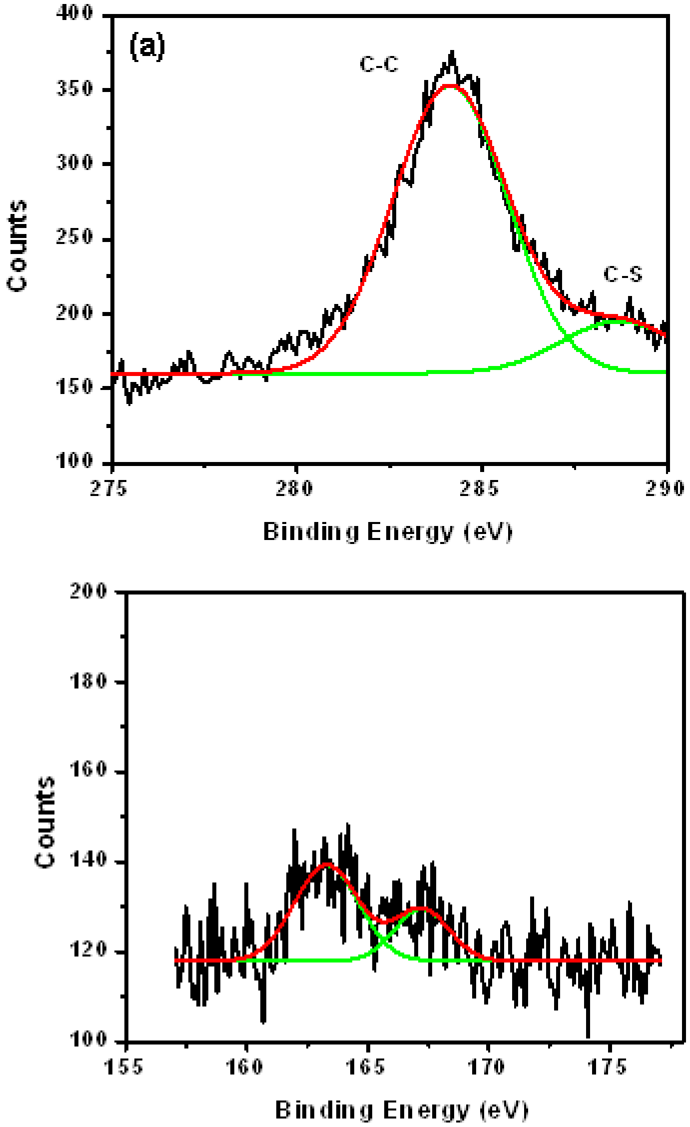

Figure 5.6 High-resolution XPS spectra of the (a) C (1s) and (b) S (2p) core levels from BT adsorbed on silver nanoparticles deposited on pore walls with 355 nm pore diameter. Deconvolution of the experimental data using Gaussian peaks is also shown in the plots.

We suggest that higher SERS activity of the substrates with larger pore diameters is due to the enhanced light transmission through the membranes in addition to the enhancement caused by nanoparticle aggregation. The enhanced transmission through the membranes could result in the excitation of many more nanoparticle hot spots within the substrate which in turn provides higher SERS activity. The reflectance spectra of the neat PAMs show almost similar reflectivity for all the PAMs irrespective of the pore diameters and hence no calibration was done in the Raman measurements.

To further confirm the presence of analyte molecules on the silver nanoparticles inside the membranes, fractured substrates (cross section) were subjected to XPS measurements. BT was deposited on the substrates prior to the measurements. Signals correspond to BT were observed form all the fractured substrates. XPS spectrum of the carbon (1s) and sulfur (2p) collected for SERS substrates with 355 nm pore diameter confirms the presence of BT layer inside pores (Figure 5.6). In Figure 5.6a the major photoemission occurs at 284.1 eV is attributed to indistinguishable phenyl group carbon atoms and the minor peak at 288.6 eV is due to carbon connected to an electronegative sulfur atom.[270,271] The two peaks observed in Figure 5.6b are assigned to the $2p_{3/2}$ and $2p_{1/2}$ spin-orbit split levels with binding energies of 163.3 and 167.2 eV, respectively.[270,271] Although the presence of BT inside the membrane is confirmed, actual estimation of surface coverage was found to be impossible because of inhomogeneity of the fractured surface structure.

Raman enhancement factor was estimated for PAM-based SERS substrates following usual procedures reported earlier.[68,292,293] The enhancement factor has been calculated using the following equation:

$$\mathrm{EF} = \frac{\mathrm{I_{SERS}}}{\mathrm{I_{REF}}} \mathrm{X} \frac{[\mathrm{REF}]}{[\mathrm{SERS}]}$$

where $\mathrm{I_{SERS}}$ and $\mathrm{I_{REF}}$ are the measured Raman intensities and [SERS] and [REF] are the concentration of analyte molecules in the SERS and reference samples, respectively. For determining the enhancement factor, the SERS intensity of the characteristic peaks of each analytes (1571 and 932 cm^{-1} for BT and PA, respectively) and Raman intensity of the analytes of known concentration on silicon wafer was compared. Raman intensity at different pore depths was extracted from the z-mapping experiments. The enhancement factor calculation was done by assuming that all molecules in the excitation volume which migrate from solution to substrates in the course of solvent evaporation will participate in SERS. This method underestimates actual enhancement because only an unknown fraction of the molecules actually end-up on silver nanoparticles and hence number reported here represents only low-bound estimation. The calculated enhancement factor value is higher than that reported for ordered micro-fabricated SERS substrates with the average values around 10^7 and the highest localized enhancement of 10^9 reported without averaging over the total surface or volume.[213,274,275]

The enhancement factor obtained for BT is ~ 10^{10} with substrates of 355 nm pore diameters. The observed record enhancement factor is four orders of magnitude better than that commonly reported for 2D substrates of gold and silver nanostructures.[258,259,260] The SERS activity with non-resonant and small PA is close to 10^6 and is ~2 orders of magnitude better than compared to 2D silver substrates.[294] It is important to note that in most of the perchlorate detection studies, the nanoparticle surface is functionalized with positively charged molecules to facilitate the adsorption of perchlorate ion on the nanoparticle surface.[295] The higher enhancement observed for BT may be attributed to the higher surface coverage because of high affinity of BT to the nanoparticle surface. Also the SERS activity of the substrates with 355 nm is an order of magnitude higher than that of the substrates with smaller pore diameters (100 nm).

To confirm the SERS intensity through the pores of the PAM-based substrates, we conducted complete Raman mapping in xy as well as in z-direction (Figure 5.7). The mapping was conducted by monitoring the intensity of the 1571 and 932 cm^{-1} peak of BT and PA through the depth of the porous alumina membranes. Since the transmission of light is higher for SERS substrates with larger pore diameters, these substrates are expected to show higher SERS intensity for greater depths from the surface of the PAM. The largest SERS enhancement occurs within 5 and 8 µm regions near the surface of the PAM for the substrates with 100 and 255 nm pore diameters, respectively. However, SERS substrates with 355 nm pore diameters show the highest SERS intensity over 10 µm region from the surface of the PAMs. The Raman intensity of the analytes gradually decreases as the depth of measurement increases from top surface of the substrate. Based on the Raman mapping experiment in the z-direction, it may be concluded that PAM-based SERS substrates with larger pore diameters facilitate enhanced light transmission through the channels. As a result, the excitation of silver nanoparticles occurs at greater depths through the PAMs, which in turn improves the SERS activity of substrates with larger pore diameters. In addition to this, the nanoparticle aggregates present on the pore walls may also help in achieving improved SERS efficiency.

The homogeneity of the substrates in the lateral direction 10 µm x 10 µm (x, y) was investigated by mapping the characteristic Raman band of the analytes on the substrates. As apparent from the 2D Raman map, uniform SERS enhancement occurs over the entire region of the substrates with SERS intensity within ± 25 %. The macroscopic uniformity of the SERS substrates was checked by collecting Raman intensity from three batches of samples fabricated from membranes with same pore diameters. SERS activity from different positions (at least 10 positions) of multiple substrates of the same pore diameter (355 nm) was measured for a laser footprint below 1 mm. The SERS intensity was found to be very reproducible at different locations within a substrate as well as between the substrates. The SERS intensity varies within ± 7% between the substrates which indicate high homogeneity of the SERS substrates despite the variation of local aggregates and the presence of residual seeds.

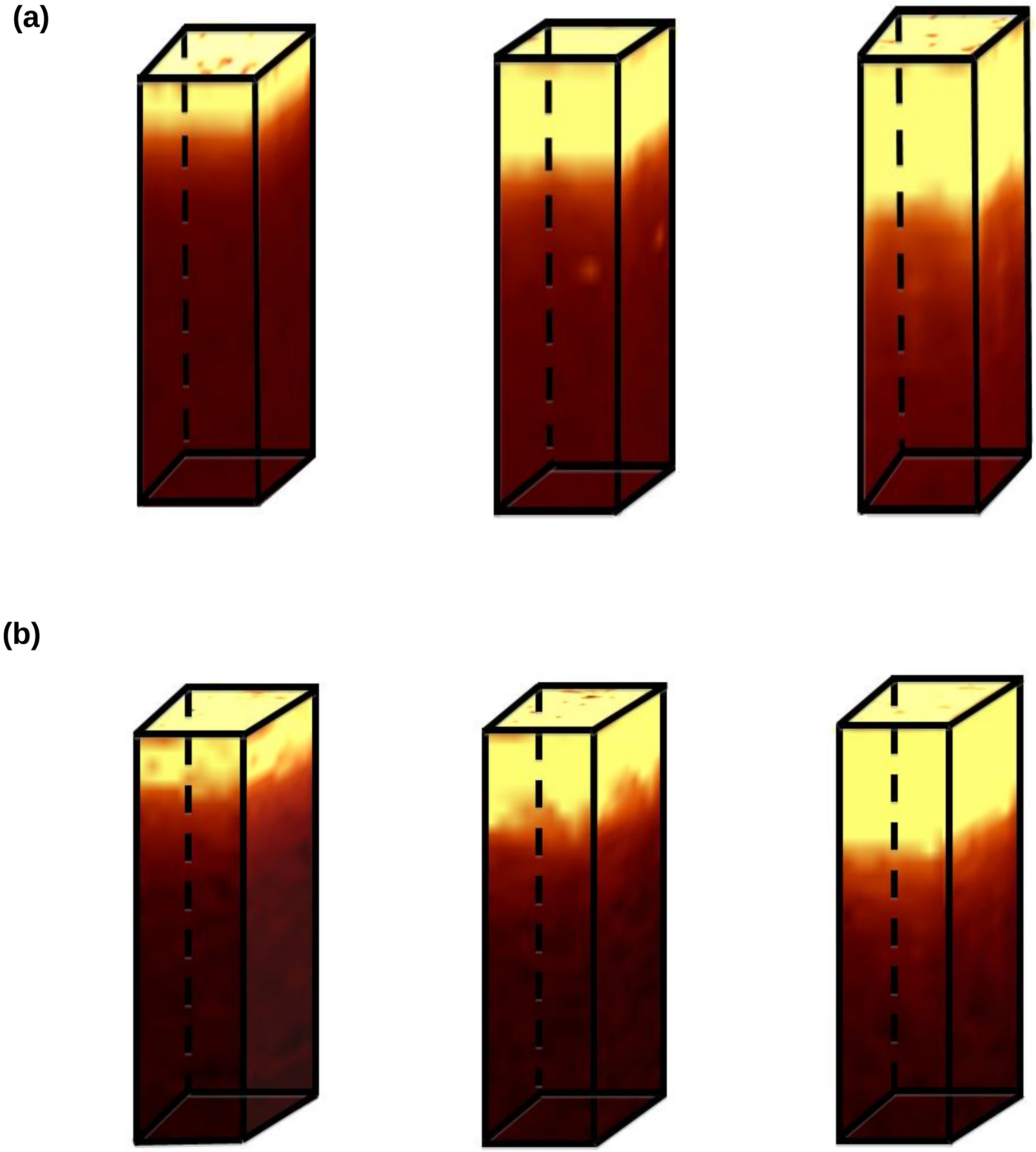

Figure 5.7 Confocal SERS mapping of (a) 1571 cm^{-1} peak of BT and (b) 932 cm^{-1} peak of PA through the depth of the porous alumina membranes with different pore diameters. (Pore dimension is shown on the corresponding z-profile). The 3D images were constructed from the experimental z- and xy-mapping.

5.3.4 Electromagnetic and quantum chemical modeling of PAMs

It has been well demonstrated that there are two mechanisms, electromagnetic (EM) and chemical enhancement (CM) that are responsible for large enhancement in SERS. EM enhancement arises due to the resonance of incident laser and the SPR of metallic nanostructures assembled on the substrates.[296,297] It is well accepted that EM contributes major part to the SERS enhancement yielding somewhere between 10^4 to 10^8. However, underlying mechanism of CM is not well understood yet and it arises due to the interaction of the analyte molecules on the metal surface. In this study, we discuss both electromagnetic and quantum chemical simulations to understand the various factors that influence the SERS activity and propose a design strategy for the fabrication of PAM-based SERS substrates with high SERS activity.

5.3.4.1 Electromagnetic modeling of Raman enhancement in cylindrical pores

To understand the pore size dependence on the SERS activity, we have simulated Raman enhancement using a silver nanoparticle dimer under different conditions. Dimers are chosen for the modeling since they are the predominant aggregates observed on the pore walls. Higher nanoparticle aggregates are not considered in this study even though higher aggregates would give an equally large enhancement over a larger area, but will not actually increases the maximum enhancement observed. Silver nanoparticles were placed in the pores with an orientation that provides maximum enhancement between nanoparticles. Dimers with other orientations and separations are not discussed here since they provide minor contributions. In all cases, enhancement predicted is at an approximately similar order of magnitude as the enhancement levels we expected to see from a silver dimer.[272,273] This implies that the majority of the enhancement is coming from the silver dimers, and that there is no great enhancing effect from the pore itself.

However, the pore acts to constraint the incident radiation in a manner such that the maximum enhancements can be realized at certain widths.

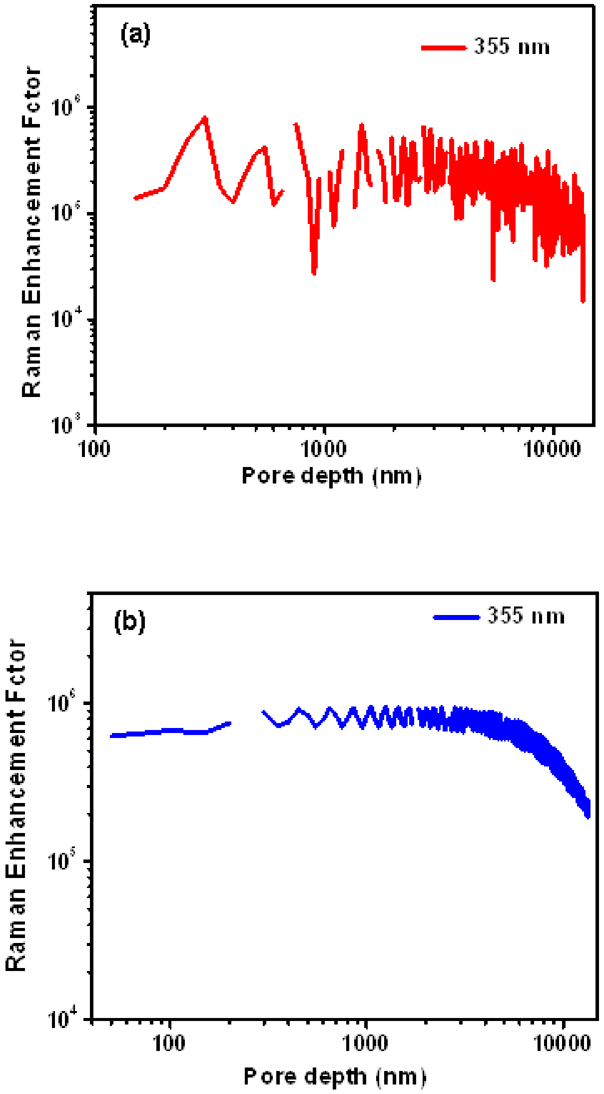

Figure 5.8 Representative Raman enhancement pattern simulated for silver nanoparticle dimers inside channels with different pore depths. (a) for the silver nanoparticle dimer placed on the wall and (b) at the centre of the pore (diameter is 355 nm).

The simulated Raman enhancement as a function of pore depth for the dimers placed at the pore walls and the center of the pore for substrates with 355 nm pore diameter shown in Figure 5.8. A series of electromagnetic field peak intensities is observed along the main axis of the cylindrical pores with spacing close to l/2. It is also evident from Figure 5.8 that significant electromagnetic enhancement occurs for nanoparticles dimers placed at several microns beneath the surface, which is in good agreement with the experimental z-mapping (Figure 5.7). Enhancements observed are in general smaller for dimers located close to the pore wall, and show much less periodicity with depth in the pore. In both cases it is thought that this is related to the damping effect of the conducting aluminum oxide walls on the incident light. The periodicity related to interference of the wavelength of the incident light with the width of the pore is apparent throughout the modeling, although this is a lot less clear when the dimer is close to the pore wall. This is due to the interfering effect of the alumina at the side of the pore. For the dimer placed at the center of the pore, the periodic variation associated with the wavelength of the light is initially much larger than any change as a result of depth with the pore. However, between about 2 and 10 microns depth in the pore, the attenuation begins to dominate the size of the overall enhancement observed. At 10 microns average enhancements are an order of magnitude less than those observed between 0.1 and 1 micron (Figure 5.8).

The enhancement observed appear to increase with pore diameter (Figure 5.9). The simulations suggest that the enhancement is at a maximum at 400-450 nm pore width before decreasing again as the pore gets wider. Membrane with 400nm pore diameter is about optimum for the pore to act as an efficient waveguide for the incident light. Any narrower than this and the light is unable get down effectively, and any wider than this and there might start to be some significant reflections and destructive interference of the light. At very wide pore sizes the light does not actually see the side of the pore at all and hence the interaction with the nanoparticles.

To compare the experimental results and simulated Raman enhancement factor, we extracted Raman intensity from the z-mapping of the substrates with different pore diameters at various pore depths. The Raman enhancement factor from both experiments and simulations for different pore depths are plotted in Figure 5.9. The overall enhancement from each of the substrate was estimated by adding Raman enhancement at

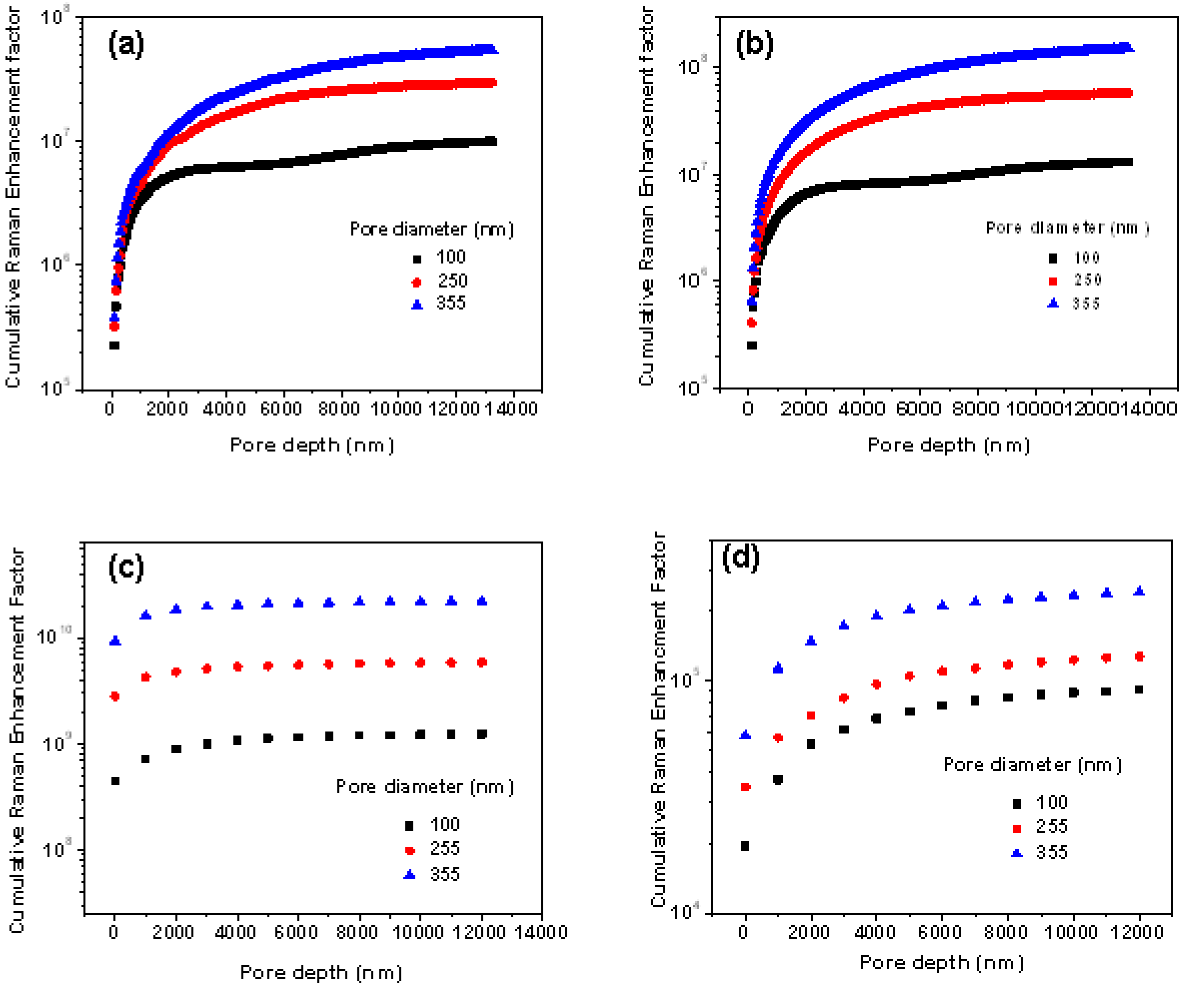

Figure 5.9 Variation of cumulative Raman enhancement factor extracted from electromagnetic simulation for different pore diameters with silver nanoparticle dimer placed (a) at pore wall, (b) at center of pore. Cumulative Raman enhancement factor obtained from experimental z- mapping for (c) BT and (d) PA with substrates of different pore diameters.

different depths (1µm interval) from the top surface of the substrates. The Raman enhancement factor gradually increases with the increasing accumulation of nanoparticle dimers along the pore depths (Figure 5.9a and b). The cumulative enhancement factor shows saturation at depth higher than 10 µm. Consistent with simulations, experimental observations also follow the same trend with SERS substrates fabricated from 355 nm pore diameters show high SERS activity with saturation at depths of 10-12 µm (Figure 5.9c and d). The general trend observed in experimental and simulations is similar considering the limited z-resolution of the Raman mapping of about 1 µm.

5.3.4.2 DFT simulation of chemical enhancement

Chemical enhancement (CM) is driven by the combined effect of three contributions namely the charge transfer (CT) mechanism,[42] molecular resonance (RRS) mechanism[41] and the non-resonant chemical (CHEM) mechanism.[44] The CT and RRS mechanism arise when incident radiation is in resonance with molecule to metal or metal to molecule electronic transition and molecular excitation respectively; they both contribute a major part towards the total enhancement of about $10\text{-}10^6$. The CHEM mechanism on the other hand occurs due to the bonding interaction between the molecule and the metal surface, allowing relaxation of the electronic structure, and giving rise to enhancements of the order of $10\text{-}10^2$.[41] Even though the difference in nature of the above enhancement mechanisms has been well identified and characterized over the years, a separation of their effect is not straight forward.

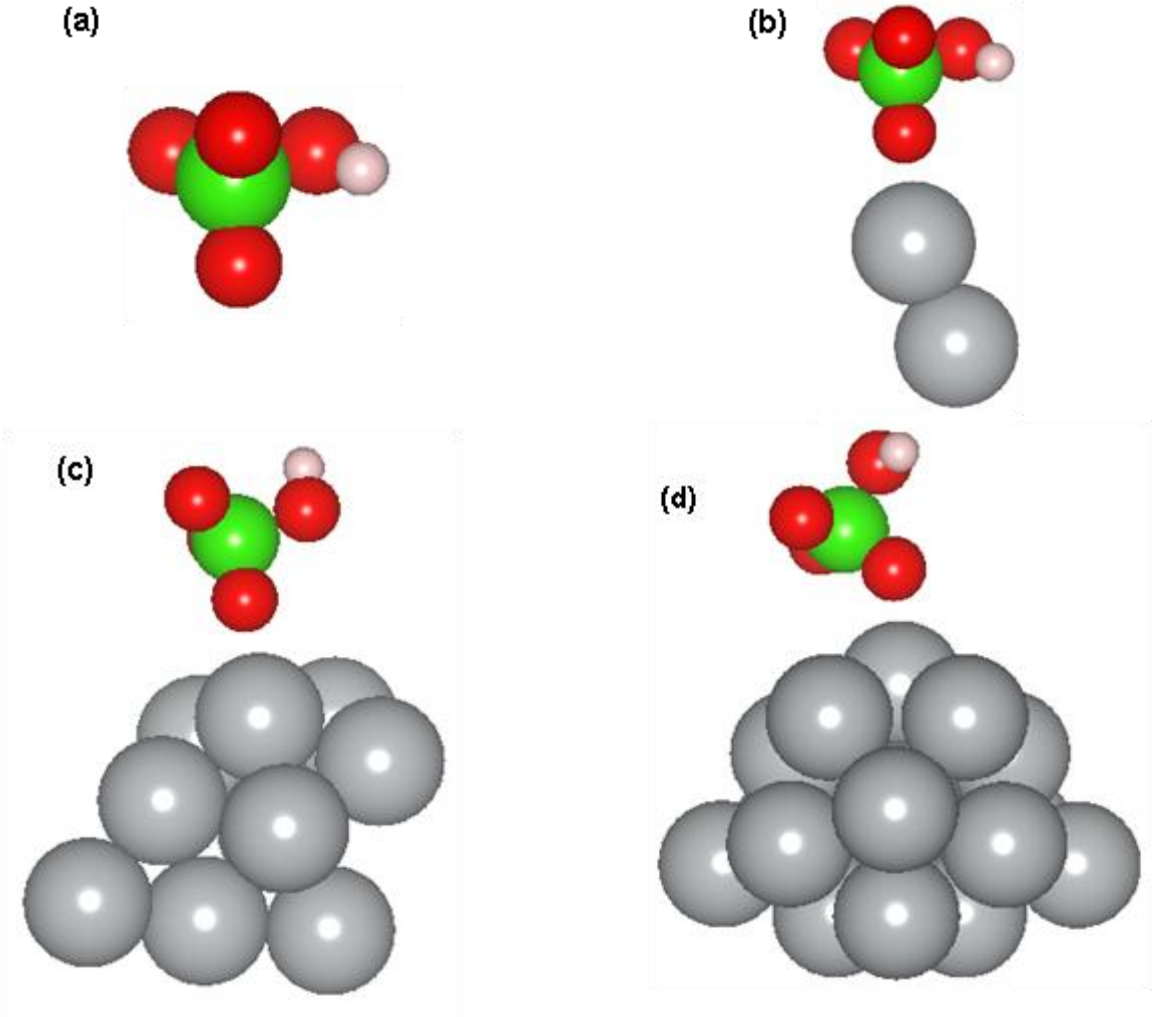

Figure 5.10 Computed structure for (a) PA and PA-Ag nanosurface with (b) 2 atoms, (c) 10 atoms and (d) 18 atoms clusters.

Simulations of SERS spectra and extraction of CM for BT have been studied extensively during the past few years.[276,298] On the other hand not many studies focusing on the CM for PA have been published. In this section we try to elucidate the combination of effects governing CM for PA concentrating on the electronic structure, bonding interactions and SERS spectra of PA on silver clusters of different size, denoted as PA-Ag_n (n=2, 10 and 18), following the theoretical procedure described in previous section. Figure 10 shows the optimized geometries of the molecule alone and combined system PA-Ag_n that were used throughout our simulations. We have found that PA is bound to the metal through the oxygen atom (Figure 5.10). In terms of bonding geometry we observe that oxygen prefers to bond directly on a Ag atom than a hollow site with a total energy difference between on-site and hollow-site bonding of about 0.05 eV.

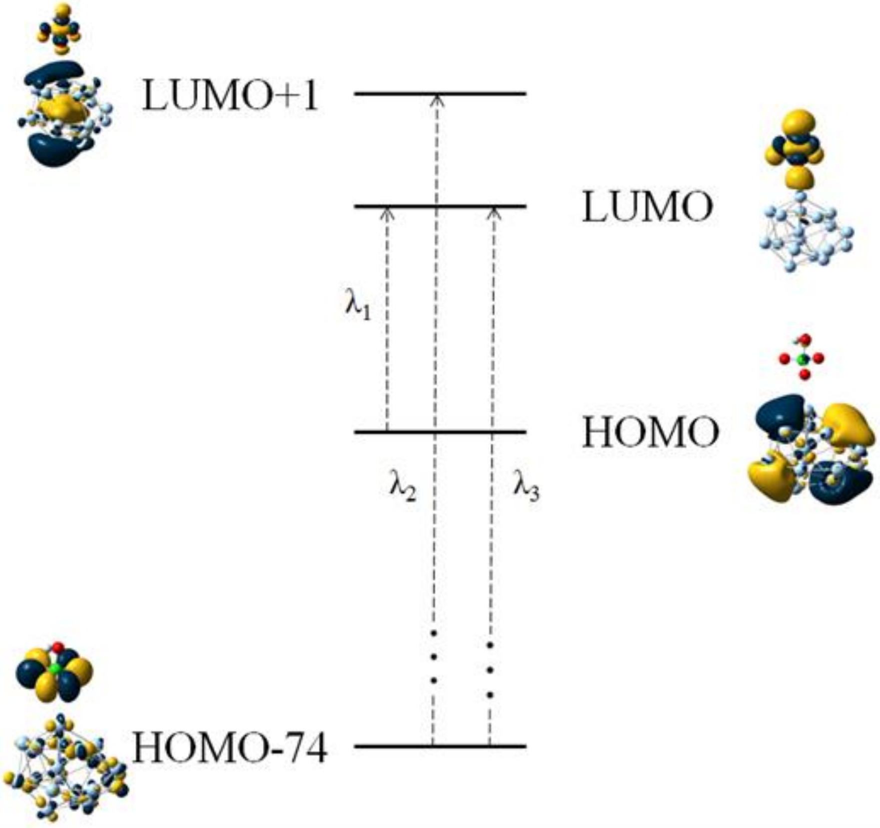

Figure 5.11 Energy level diagram of the PA-Ag_{18} complex. λ_1 = 1.12eV = 1180.3nm corresponds to a metal to molecule CT, λ_2 = 7.02eV = 176.8nm corresponds to a molecule to metal CT, while λ_3 = 6.37eV = 194.9nm shows the required incident wavelength for resonant Raman scattering to occur.

Table 5.1 Calculated electronic polarizability (in a.u) and O-Ag (nm) bond length for PA and Ag_n-PA (n= 2, 10, 18).

System	Induced static polarizability (a.u)	Bond length (O-Ag) (nm)	Partial charge on cluster (e.u)	HOMO-LUMO gap(ev)
PA	-	-	-	6.54
Ag_2-PA	10.464	0.277	-0.0112	1.93
Ag_{10}-PA	34.581	0.277	-0.0528	1.20
Ag_{18}-PA	44.526	0.266	-0.0609	1.12

The structures PA-Ag_2 and PA-Ag_{10} represent the simplest configuration of PA bound to Ag. The larger structure PA-Ag_{18} shows a more prominent metallic character as the energy difference between the highest occupied molecular orbital and the lowest unoccupied molecular orbital, i.e. the HOMO-LUMO gap, is found to be smaller (Table 5.1). The HOMO of the complex shows a strong metallic contribution while the LUMO is primarily localized on the adsorbate as shown on Figure 5.11. The energy level diagram of Figure 5.11 gives an account of the possible chemical mechanisms for the PA-Ag_{18} complex. A CT metal to molecule enhancement can only occur when there is a transition from the HOMO to the LUMO of the complex with an energy barrier of 1.12eV corresponding to λ_1=1180 nm which is the wavelength of the incident light required for such a transition. In the same way a molecule to metal CT enhancement can occur when there is a transition from the highest occupied molecular orbital with major contribution on the adsorbate to the lowest unoccupied molecular orbital with major contribution on the metallic cluster. We find that in this case the former orbital corresponds to a deep lying energy level, HOMO-74, while the latter is one energy level above LUMO, denoted as LUMO+1. The energy barrier in this case is 7.02eV or λ_2=177nm. An enhancement relevant to resonant Raman scattering can occur during a transition from HOMO-74 to LUMO. Both orbitals have a major contribution on the adsorbate, in fact they are the HOMO and LUMO of the isolated molecule shifted due to bonding with the metallic cluster. The energy barrier for this transition is 6.37eV or λ_3=195nm. The incident laser pulse of λ=514.5 nm used in our SERS measurements is therefore insufficient to initiate either a metal to molecule, λ_1, or molecule to metal, λ_2, electronic transition as well as a molecular excitation, λ_3, implying that contribution from either CT or RRS on the Raman enhancement should not be significant on the PA-Ag_n complex. We hence consider only the CHEM mechanism from now on.

Due to the bonding interaction between PA and metal as well as the subsequent relaxation of the electronic structure of the complex, there is a redistribution of charge and transfer occurring from PA to the silver cluster. The amount of partial charge transferred along the O-Ag bond in each of the three complexes is tabulated in Table 5.1 and was estimated via a natural population analysis. It is clear from Table 5.1 that the amount of charge transfer on the silver cluster is increasing with the size of the cluster which in turn is related to the increase of the induced static electronic polarizability calculated for the PA-Ag complexes (Table 5.1). This reflects the degree of interaction between the organic/inorganic components in the complex as well as the ability of the system to be Raman excited; hence complexes of larger sizes are expected to show enhanced Raman intensity.

Simulated Raman spectra of perchloric acid and PA-Ag_n complexes are shown in Figure 5.12a. The Raman band at 932 cm^{-1} is due to symmetrical stretching of Cl-O bond as indicated by the displacement vectors of PA bonded to an 18-atom cluster (Figure 5.12b). We observe that silver atoms do not contribute to any significant Raman band; it is the Cl and O atoms mainly responsible for the Raman peaks. We notice from Figure 5.12a that the intensity of the characteristic Raman band of PA increases with cluster size. Analysis of O-Ag bond length in each of the clusters suggests that O-Ag bond length becomes

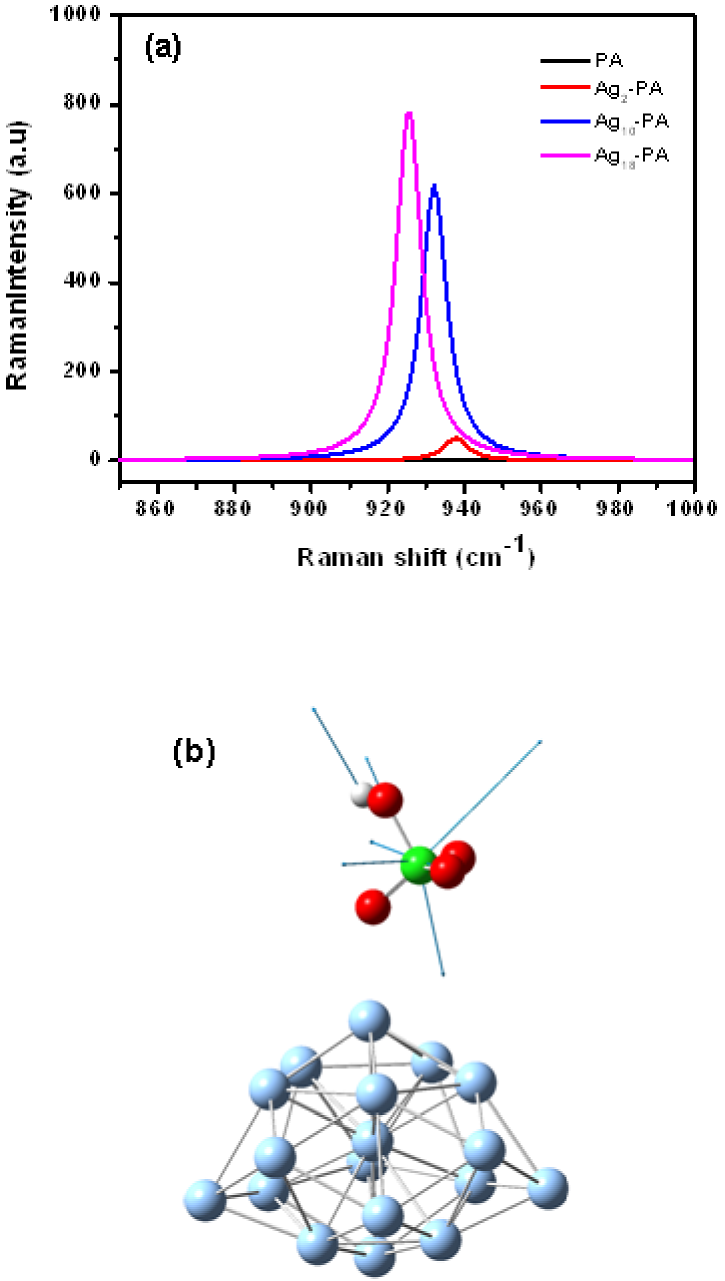

Figure 5.12 (a) Computed SERS spectra of perchloric acid and perchloric acid-silver clusters with different atoms. (b) Displacement vector corresponds to 931 cm^{-1} band.

shorter as the cluster size increases (Table 5.1). Oxygen binds to metal clusters via a dative bond where the O lone pair is partly donated to the metal; therefore charge transfer along the bond is more pronounced, the dipole formation is stronger and the polarizability is higher at bigger clusters. This has a prominent effect on the enhancement in Raman intensity. Also it is interesting to note that the Raman band of isolated PA shifts to lower frequency (from 945 to 932 cm^{-1}) when attached to silver clusters of increasing size. This red shift in the frequency of the vibration is related to the decrease of the O-Ag bond as the cluster size increases (Table 5.1). This range of Raman peak position is in good agreement with the experimental SERS spectrum obtained with silver nanoparticles.

To understand the effect of different binding sites on Raman spectra, we have simulated two extreme cases of different binding configurations of the tetrahedral Ag_{20} cluster, i.e. surface (S) vs vertex (V), bound to PA (Figure 5.13). Several theoretical studies have shown that absorption properties of Ag_{20} are quite similar to the plasmon absorption of silver nanoparticles, thus Raman enhancement due to these clusters is comparable to that of large nanoparticles of diameter greater than 10 nm.[299,300]

It has been shown that for pyridine (py), Ag_{20}-py surface complex shows better agreement with experimental results.[301] In our study, comparison of the experimental and simulated SERS spectra shows better agreement with the PA-Ag_{20} vertex system than the surface complex. Since the analysis of HRTEM images of silver nanoparticle suggest the presence of (111) crystallographic planes at the surfaces, we believe that adsorption of PA on (111) plane is more probable in our experiment. It is well known that in order to reach the state of thermodynamic stability, crystal faces with higher free energies will grow faster and be difficult to expose at the surface in large proportions.[289,302,303] On the other hand, crystal faces with lower energies such as (111) can be exposed in large preposition while the crystal faces with higher energies such as (110) and (311) grow on edges, corners, etc. in small proportions. We thus believe that the simulation carried out with the Ag_{20} clusters is relevant to the real experimental conditions.

The V-complex can be considered as adatom or adparticle structure. It is believed that atomic scale roughness such as adatom or adparticle are crucial structures for short-range chemical enhancement mechanism.[304,305,306] In our experimental system, we believe that it is more probable to have situations with adparticles on the (111) surface rather than an

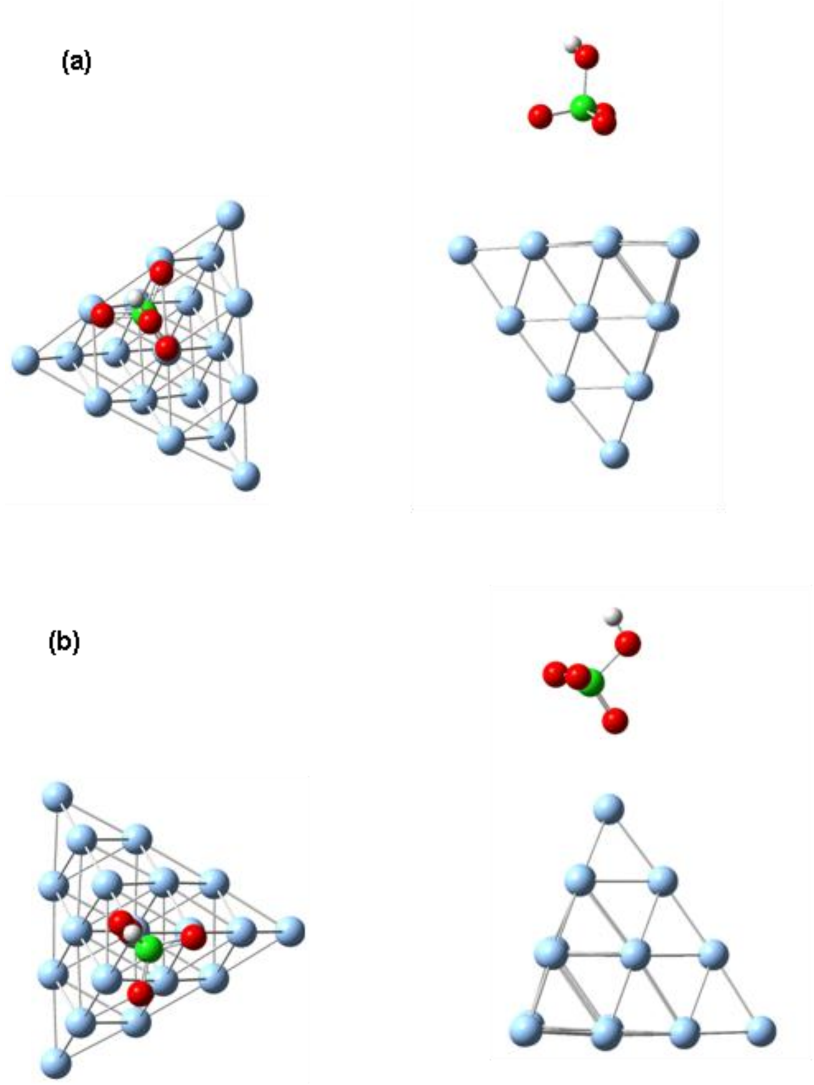

Figure 5.13 Orientation of perchloric acid on (a) surface and (b) vertex configurations of the Ag_{20} cluster.

ideally clean (111) surface as confirmed by TEM images. The Raman intensity of PA with and without the presence of a silver cluster provides a direct measure of CHEM enhancements.

We hence investigate further the Raman enhancement due to these two different binding situations. We find that CHEM enhancement is stronger on a vertex configuration which is also energetically more favorable as its adsorption energy was found to be E^{V}_{ads}=-0.117eV in contrast to E^{S}_{ads}=-0.144eV. As discussed in other relevant work[302,307] CHEM could be attributed to the ground-state interaction of the molecule with the metal. This can be understood firstly by looking at the HOMO and LUMO orbitals of both complexes. We see that while the adsorbate has no contribution on the HOMO of both S and V this is not the case for the LUMO orbital; the LUMO orbital is localized on PA but there is a higher contribution of the metal cluster on the LUMO of the V complex compared to the S complex which implies stronger interaction between metal-adsorbate in the vertex complex in terms of its electronic structure. This also affects the magnitude of the static polarizability which is found to be higher for the V complex. The above arguments are further verified by looking at the Ag-O bond length for the surface and vertex complex which is 0.391nm and 0.279 nm respectively. This difference in bond distance is 0.11 nm and is due to the different binding geometry of the two complexes as seen in Figure 5.13, i.e. the V complex binds via a single oxygen atom to the cluster while the S complex interacts via three oxygen atoms. This difference in bond length is also responsible for the red shift in the Raman intensity from 949 to 932 cm^{-1} observed in Figure 5.14. Overall we observe an enhancement of about 2 orders of magnitude for the vertex compared to the surface complex. Based on the large difference in the Ag-O bond length observed for Ag_{20} surface and vertex complexes, it is reasonable to assume that at the surface complex PA is physisorbed on the cluster while the vertex complex can be considered as weekly chemisorbed on the cluster.[299]

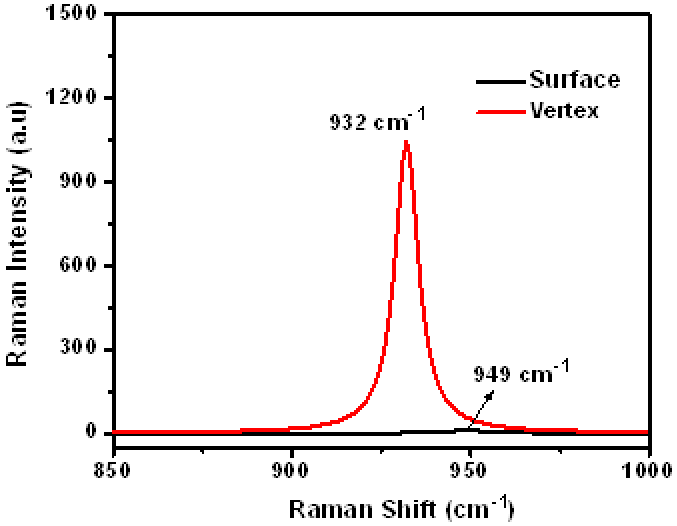

Figure 5.14 Simulated SERS spectra of perchloric acid on Ag_{18} and Ag_{20} clusters with different binding sites.

For BT, the experimental enhancement factor is more than two orders of magnitude higher than that calculated from the electromagnetic simulation. This additional increase can be attributed to the contribution from chemical enhancement (which can reach 10^3) for BT molecules chemisorbed on silver surface.[298] However, the enhancement factor obtained for PA is lower than the theoretically predicted enhancements despite of having reasonable contribution from chemical enhancement mechanism. This may be due to the low surface coverage of PA in the hot spots may be due to low binding affinity of PA to silver nanoparticles. Although the observed enhancement is modest, the enhancement factor is ~2 orders of magnitude better than that obtained for 2D SERS substrates of silver nanoparticles with specific surface functionalization to facilitate adsorption of perchorate ion on the nanoparticles surface. Based on our experimental and simulation studies it is proposed that the transmission of light, deposition of nanoparticles within first 10 µm microns depth of the membranes, binding of analyte molecules on specific binding sites are very important factors in achieving high SERS activity of PAM-based SERS substrates.

This study offers a new strategy to optimize fabrication of PAM-based SERS substrates that show high SERS activity. The electromagnetic simulation of silver nanoparticle dimer inside the alumina membranes of different pore diameters helped us to optimize the fabrication of PAM-based SERS substrates with optimum pore sizes to enhance the SERS activity. As suggested by the simulation, deposition of nanoparticles within the first few microns from the surface is found to be important in achieving enhanced SERS response. Considering both experimental data from the z-distribution of Raman scattering and simulated results on electromagnetic field distribution for PAMs decorated with silver nanoparticles, we believe that the fine optimization of Raman activity for long cylindrical pores can be achieved by choosing the diameter of cylindrical pores around 350-400 nm and a total length of within 10-12 µm. Our DFT simulation provided further insight concerning the favorable orientation and binding site of the PA molecules as they attach to the silver nanoparticles, the Raman band positions and associated Raman active modes, as well as understanding of analyte-metal interaction and its effect on the SERS enhancement. In particular, we have focused on the chemical mechanism which shows higher contribution to the overall SERS enhancement than previously believed.

In this work, we have demonstrated optimization of PAM-based substrates exhibiting high Raman enhancement factors by tuning transmission of light, deposition of nanoparticles on the cylindrical nanopores. Also, the enhancement factor observed for 3D observed is several orders of magnitude higher than that reported for traditional 2D substrates. Overall, the current study provides an example of a comprehensive approach that considers the transmission of light confined in cylindrical pores toward designing highly optimized 3D SERS substrates with enhancement factors of several orders of magnitude higher than traditional planar substrates.

CHAPTER 6

LABLE-FREE RAMAN MAPPING OF SURFACE DISTRIBUTION OF PROTEIN A AND IGG BIOMOLECULES

6.1 Introduction

Biosensing devices are designed to specifically bind selected biomolecules and subsequently convert this local event in to a measurable signal.[1] The mechanism of biomolecular detection is frequently based on measuring specific optical absorption such as that implemented in the enzyme-linked immunosorbent assay (ELISA) method,[45] surface plasmon resonance (SPR) techniques,[53] or fluorescence resonance energy transfer (FRET).[187] These well-known methods, however, do not provide a ready pathway for facile and direct label-free detection of the biomolecular analytes within one measuring cycle. These approaches often require a complex sequence of synthesis of labeled molecules and specimen preparation, which are costly, time-consuming, rely on synthetic routines which might/not might work for selected biomolecules and must be designed specifically for the biomolecular system of interest. This novel, rapid, and simple method for the label-free trace detection of selected proteins has clear advantages such as no complicated sample preparation or multiple intermediate steps which facilitate "user-friendly" and relatively universal biosensing routines. In addition, such a facile routine should improve the range of prospective applications, limiting sensitivity, and accuracy of detection for future biosensing approaches.

Among numerous methods of biodetection, surface-enhanced Raman scattering (SERS) has become an area of intense research as a highly sensitive probe for trace level detection of small molecules since the demonstration of single molecule detection.[20,22,169] The highly sensitive vibrational spectroscopic technique of SERS can potentially provide a method for label-free sensing and analysis of proteins, down to single molecules, which was previously impossible due to the complexity of such biomolecules.[184,185,186] In order to realize potential advantages of this approach, there have been various suggested designs to provide dramatic enhancement for the SERS response. SERS phenomenon is possible due to the large electromagnetic fields that exist in the small gaps between metal nanostructures called hot spots.[308] The design of the substrate on which the SERS phenomenon becomes significant is the most critical aspect of a sensitive biomolecular probe.[158] Most popular designs involved various engineered substrates such as roughened metal nanoparticle films,[159,160] metallic and bimetallic nanostructures,[71,164,165,166] and 3D porous substrates.[60]

Among important biological molecules, IgG is the most abundant immunoglobulin in the blood and is produced in large quantities during secondary immune responses.[121] The binding of the Fc region of IgG, which coats microorganisms in the blood, and the Fc receptors of macrophages and neutrophils allows these phagocytic cells to bind, ingest, and destroy invading bacteria.[130] The accurate and trace detection of IgG is extremely important in an effort to better understand its role in complement responses in the body and other concentration dependent roles it may play, as well as provide a precedent for the label-free detection of other biomolecules. Standard fluorescent-based methods for IgG detection, such as ELISA, are widely used, but these methods have certain drawbacks such as photobleaching, time-consuming sample preparation, and a moderate limit of analyte detection.[72] Previous SERS studies have been performed for IgG,[309,310] leading to a characteristic spectrum of this biomolecule. These studies, however, show a range of peaks which are likely caused by complex enhancement, which depends upon the orientation of the polarizable component of the vibration with respect to the metal surface.[311,312]

In order to facilitate highly sensitive detection of trace amounts of biomolecules and separate numerous secondary contributions, a new substrate must be designed to allow selective adsorption of proteins in active regions, thus increasing the selectivity and level of detection and providing concurrently measured background for non-selectively adsorbed compounds under identical conditions.[313] Micropatterned surfaces are frequently used as SERS substrates due to their high degree of order, simplicity of microstamping fabrication, and reproducible results, which cannot be provided by other surfaces.[314,315] Soft lithography is a simple process that can be adopted to fabricate micropatterned arrays for selective adsorption.[316] Micron-sized, long-range ordered metal nanoparticle arrays extended over cm-scale areas can be fabricated utilizing capillary transfer lithography.[317]

The high degree of order provided by micropatterned surfaces is critically important for separating the SERS-enhanced spectra of the biomolecule of interest and any background from the substrate and non-specifically adsorbed species. These surfaces also provide the researcher with the ability to easily tailor the pattern to the specific system being studied. Other advantages of the micropatterned substrate are the ease of position control when taking measurements and the elimination of common difficulties in background subtraction due to the simultaneous analyte and background measurements. The micropatterned surface allows for more reliable detection of very small concentration of biomolecules due to identical collection conditions for signal and background and thus more accurate subtraction of substrate background, which might reach 50% at the lowest concentrations. Collecting background spectra for surface areas from other specimens in a separate experimental cycle dramatically compromises the quality of the background removal and thus the overall sensitivity of the procedure at the lowest concentrations.

In this study, we report on the rapid, label-free mapping of two selected biomolecules, protein A and IgG, adsorbed on a novel micropatterned SERS substrate down for nanomolar concentrations of solutions. The model system exploited in this study is the well-known binding reaction of protein A to the Fc region of IgG.[318] The substrate design suggested here provides a simple method that is much faster (less than 30 min of total experiment time) than current optical methods.

6.2 Experimental details

Silver nanoparticles were synthesized by the photoreduction technique described in detail in Chapter 3.[230] A micropatterned silver nanoparticle substrate was prepared using capillary transfer lithography over a 5 mm x 5 mm area. A simple diagram illustrating the soft lithography process exploited here is shown in Figure 6.1. Three bilayers of poly (allylamine hydrochloride) (PAH) (M_w=70,000)/ poly (styrene sulfonate) (PSS) (M_w=70,000) and one more layer of PAH were deposited on a silicon substrate according to the standard procedure used in our lab.[319] [100] silicon substrates (Semiconductor Processing) with a native silicon oxide layer with 1.6 nm thickness were cleaned with piranha solution (3:1 concentrated sulfuric acid and hydrogen peroxide mixture, *Caution!*), abundantly rinsed with Nanopure water, and dried with dry nitrogen stream in accordance with usual procedure.[320] They served as hydrophilic substrates for spin-assisted LbL film depositions of pre-layers with uniform coverage over the whole surface area.[321,322]

A 400 nm thick polystyrene (PS) pattern with a periodicity of 10 μm defined by a polydimethylsiloxane (PDMS) stamp was then deposited onto the LbL nanocoating. After patterning, silver nanoparticles were deposited on the patterned surface and the PS pattern was dissolved in toluene leaving striped regions of silver nanoparticles similar to the routine reported earlier.[323,324]

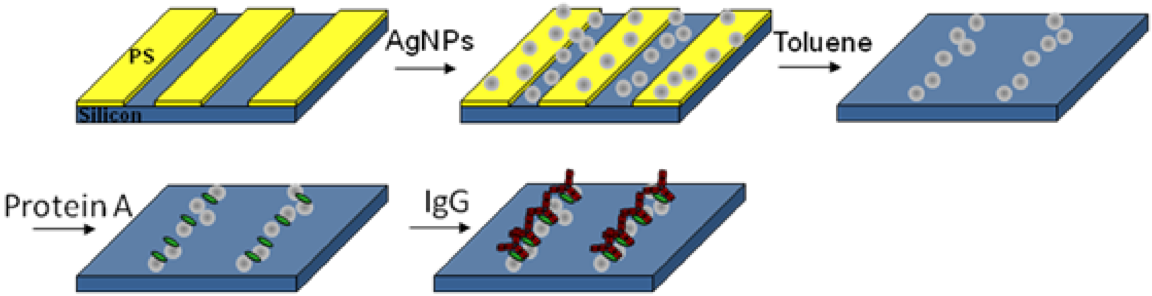

Figure 6.1 Fabrication steps of the micropatterned SERS substrate with silver nanoparticles and subsequent binding of protein A and IgG. The striped pattern of silver nanoparticles was made via the capillary transfer lithography technique.

UV-Vis spectra of the nanoparticles were measured in both the solution state as well as aggregated on the micropatterned substrate using the methods detailed in Chapter 3. Fluorescent spectroscopy and microscopy were performed to determine the presence and binding locations of the proteins. Atomic force microscopy (AFM) of the silver nanoparticle array before and after protein A and IgG deposition was conducted according to usual procedure adapted in our lab.[240,241] High resolution AFM was performed with a Dimension Multimode-Nanoscope IIIa, for scans of 500 nm x 500 nm areas in an enclosed chamber kept at less than 2% relative humidity. The AFM images of several different areas of the sample were collected and representative images were selected.

For the detection of protein A and IgG on the SERS array, confocal Raman microscopy and mapping was used as described in Chapter 3.[243] The image was acquired line by line with an Avalanche photodiode detector (APD) in the single photon counting mode by fast imaging with lateral resolution of ~500 nm and vertical resolution of 1 µm with a 50x objective lens. For detection limit studies, the SERS substrate was exposed to protein solutions with a series of concentrations down to a 10^{-10} M for 30 seconds each and washed thoroughly with Nanopure water before collections of Raman spectra.

6.3 Results and discussion

6.3.1 Nanoparticle and substrate characterization

The soft lithography technique used to fabricate the micropatterned substrate is shown in the schematic in Figure 6.1. The UV-vis absorption spectra of the particles before and after adsorption on the micropatterned surface are shown in Figure 6.2. The silver nanoparticles synthesized here show a strong absorption band at 430 nm which is expected for non-aggregated silver nanoparticles with a citrate shell.[230] The position of the absorption band corresponds to nanoparticles of 35 nm in diameter.[325] Upon adsorption and aggregation on the surface of the micropatterned substrate, the plasmon band shifts to a longer wavelength, which is close to the wavelength of the laser used for the SERS measurements (514 nm), maximizing the SERS enhancement. The red-shift of

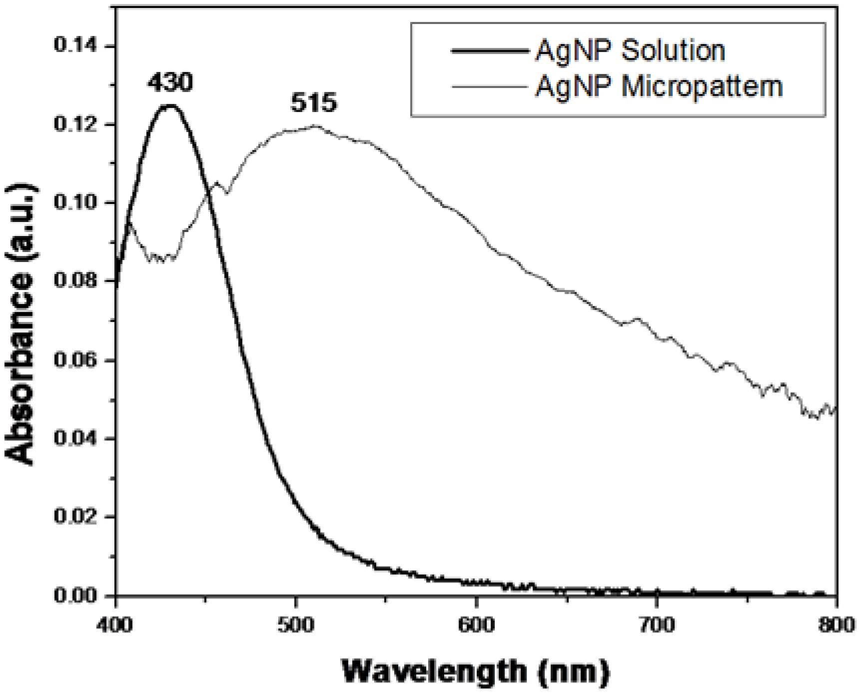

Figure 6.2 UV-vis spectra of the silver nanoparticles in solution and after aggregation on the micropatterned substrate.

the silver nanoparticle plasmon band is a result of the coupling of the surface plasmons of the individual nanoparticles upon aggregation and has been well-documented in previous studies.[326,327,328]

AFM scanning confirmed highly selective adsorption of silver nanoparticles on amine-terminated areas (Figure 6.3a and b). The optimal concentration of AgNPs adsorbed on the patterned substrated was determine by sequential deposition cycles of AgNPs from solution. The maximum SERS intensity was seen at approximately 60% surface coverage. Further deposition cycles of AgNPs resulted in nonuniform multilayers of nanoparticles with no further SERS intensity increase. To further characterize the diameter of silver nanoparticles, high resolution AFM was completed for selected surface areas with uniform nanoparticle distribution within selected striped areas (Figure 6.3c). Cross-sections through individual nanoparticles revealed an average diameter of 33 ± 5 nm, which corresponds closely to that suggested from the position of absorption band in UV-vis spectra (Figure 6.3d).

6.3.2 Patterning of protein A and IgG

As introduced above, the different surface elements of the SERS substrate were designed to allow selective adsorption of protein A on regions of the patterned surface containing silver nanoparticles (Figure 6.4). The robust and uniform amine-terminated LbL nanocoating contributed to the specific adsorption of protein A on the SERS-active silver nanoparticles by preventing non-specific adsorption through electrostatic repulsion. As expected, IgG should subsequently bind to the substrate only on selected surface regions

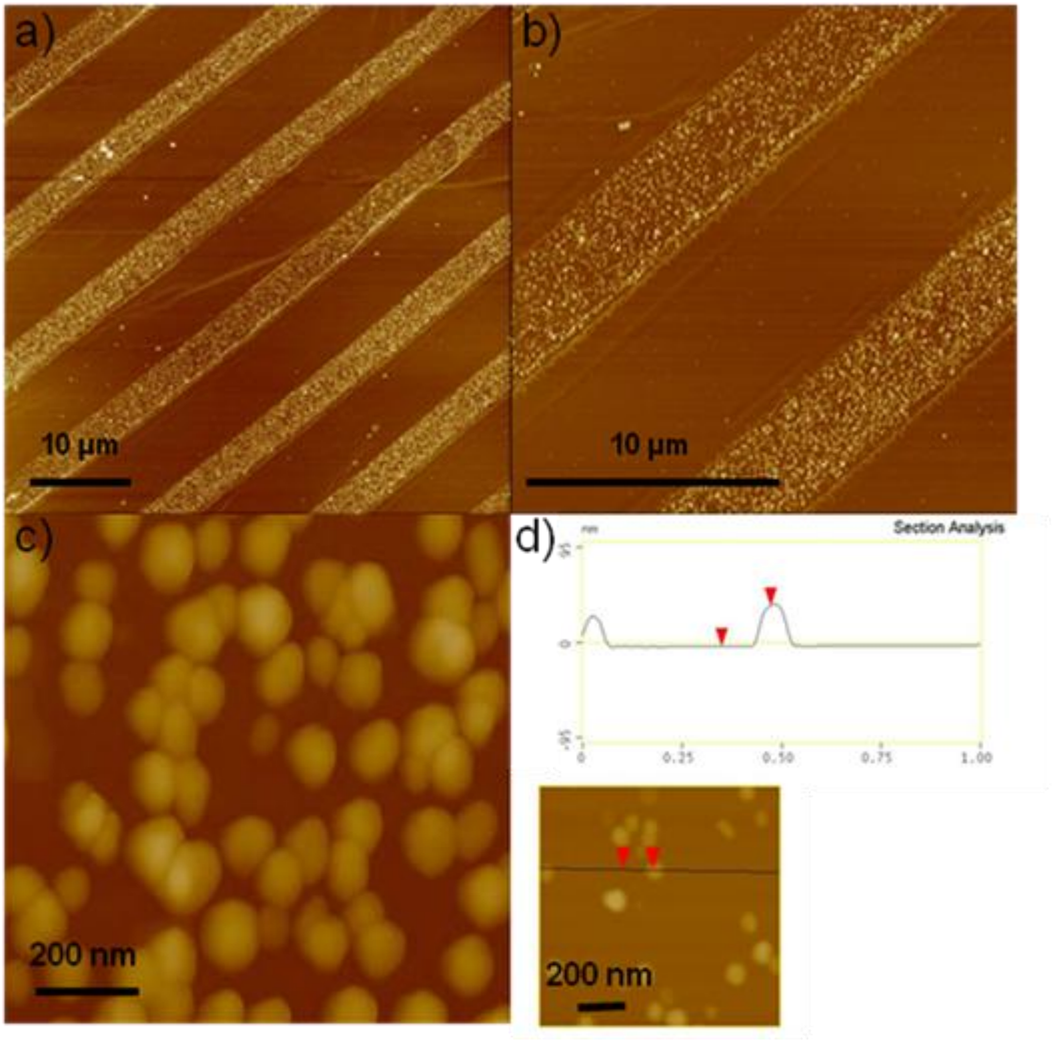

Figure 6.3 AFM topographical images of the micropatterned substrate with (a) 50 µm x 50 µm, (b) 20 µm x 20 µm, and (c) 1 µm x 1 µm scan sizes, and (d) a cross-section of individual nanoparticles. The z-scale of all images is 200 nm.

by the well-documented specific binding of protein A to the Fc region of IgG (Figure 6.4). The adsorption of protein A was conducted at pH 5 where protein A exists as a more positively charged species.[329] The pH for the adsorption of IgG was increased to pH 7 to prevent any electrostatic repulsion between protein A and IgG which can occur at low pH where both molecules are more positively charged. The selective binding of the biomolecules is one of the most critical factors for SERS detection because the analyte must be present near the enhanced electromagnetic field located at metal nanostructure junctions. The electrostatic attraction of protein A to the silver nanoparticles and the biochemical binding of the Fc region of IgG to protein A provides a clear pathway for the specific detection of the biomolecular species via SERS.

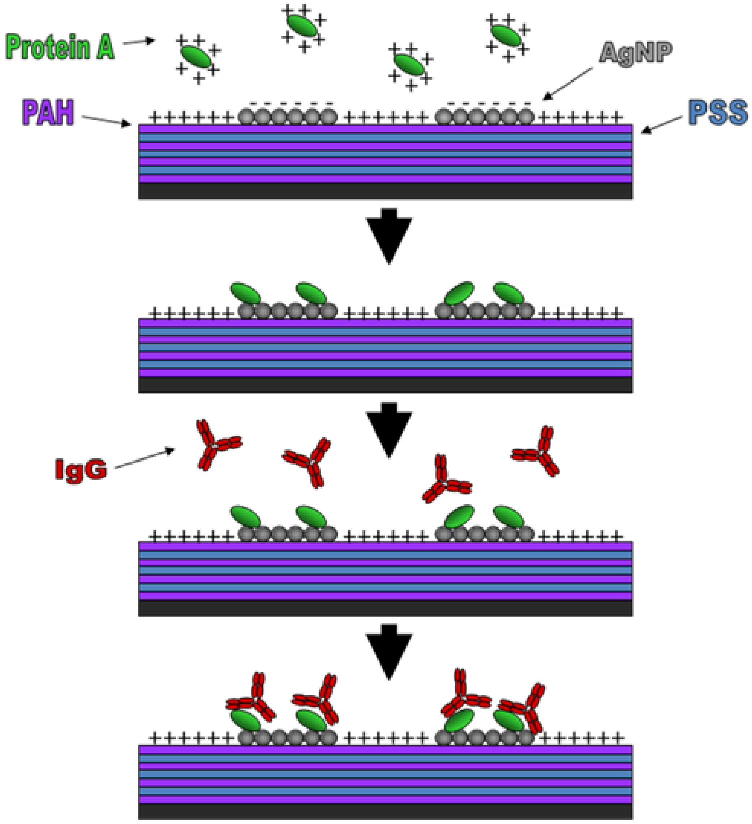

Figure 6.4 Diagram illustrating suggested sequential adsorption of fluorescently-labeled protein A and IgG to the silver nanoparticle micropatterned SERS substrate.

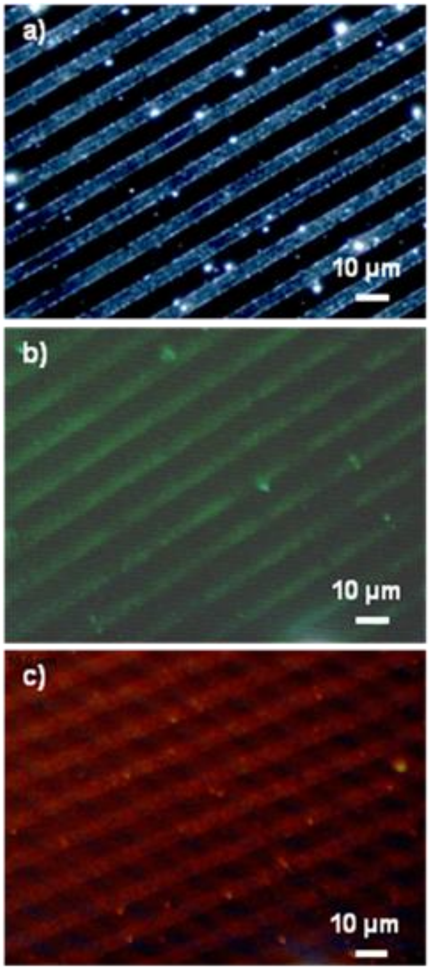

Figure 6.5 Fluorescent microscopy images of the silver nanoparticle micropatterned substrates (a) dark field before protein adsorption, (b) after fluorescein-conjugated protein A adsorption, and (c) after rhodamine-conjugated IgG adsorption.

In fact, by using fluorescein-labeled protein A and rhodamine-labeled IgG, it was possible to determine a sequence of the specific adsorption and binding of the biomolecules in striped regions containing silver nanoparticles by following different fluorescent bands (Figure 6.5). The two different fluorophores selected for proper labeling, fluorescein and rhodamine, have two very different excitation wavelengths and emission wavelengths, which allows for the protein A and IgG adsorption to be separately monitored to verify the presence of each biomolecules. The characteristic emission colors of fluorescein and rhodamine are green and red respectively as can be revealed by excitation with different wavelengths (see discussion below and corresponding fluorescent spectra in Figure 6.6).

The nanoparticle micropatterned surface was first exposed to a solution of fluorescein-labeled protein A. The fluorescent microscope image in Figure 6.5b clearly shows that the fluorescein is present only in regions containing nanoparticles as confirmed by comparison to the dark field image in Figure 6.5a. This detection is possible because an excitation wavelength of 495 nm was used, which is the wavelength associated with fluorescein. This result indicates that protein A is selectively binding to the silver nanoparticles on the substrate. This will subsequently allow for specific adsorption of IgG onto the nanoparticles, resulting in the optimum condition for SERS detection of the

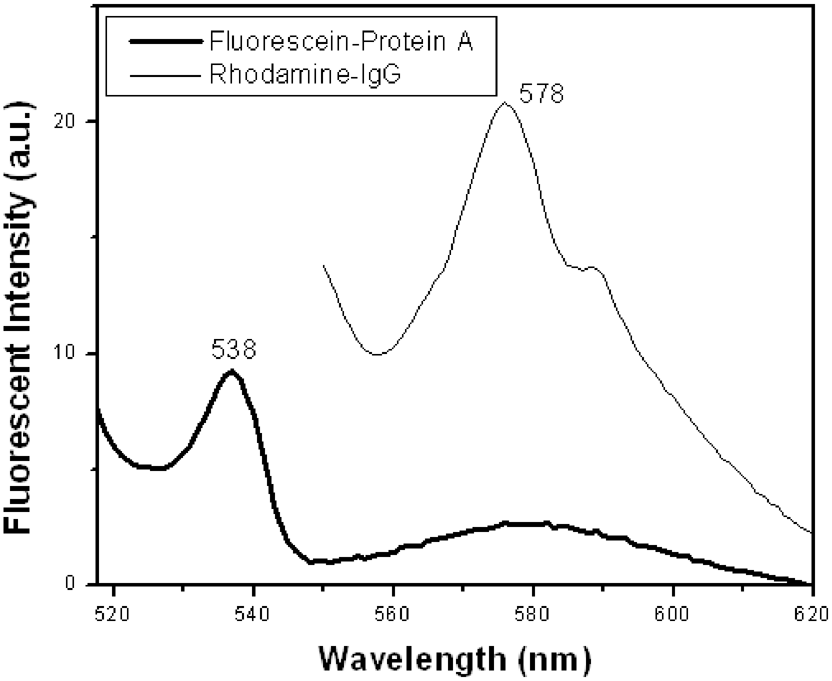

Figure 6.6 Fluorescent spectra after the adsorption of protein A and IgG on the micropatterned substrate indicating the presence of both fluorophores after final adsorption stage. The 538 nm peak indicates the emission of fluorescein-conjugated protein A obtained at an excitation wavelength of 495 nm and the 578 nm peak indicates the emission of rhodamine-conjugated IgG obtained at an excitation wavelength of 550 nm.

biomolecules. The fluorescent emission of rhodamine molecules can also be clearly seen using an excitation wavelength of 550 nm following rhodamine-labeled IgG adsorption to the surface (Figure 6.5c). Both fluorescence images show that the proteins specifically bind in regions containing nanoparticles, meaning that the proteins are in optimal locations on the sample for SERS enhancement.

To assure that IgG was binding to protein A and not replacing it on the surface, additional measurements were performed. In these measurements, fluorescent spectroscopy was conducted to confirm the presence of both fluorophores on the substrate at two different excitation wavelengths (Figure 6.6). The presence of two strong bands (corresponding to fluorescein and rhodamine) on the fluorescent spectra of the final micropatterned substrate containing both fluorescein-labeled protein A and rhodamine-labeled IgG confirms the presence of both biomolecules following the final adsorption step. The characteristic fluorescent emission peaks for fluorescein (538 nm) and rhodamine (578 nm) are both present after sequential adsorption with protein A. This indicates that both proteins retain on the surface due to strong tethering between oppositely charged groups. It is speculated that the shouldering that is present on the rhodamine-IgG curve may be the result of the complex interactions between the fluorophores and proteins present on the substrate. This spectroscopic result shows that both protein A and IgG remained tethered to the silver nanoparticles after the final protein binding sequence and thorough washing cycles (Figure 6.4, bottom panel).

High resolution AFM images of the micropatterned regions were additionally collected to determine the difference before and after adsorption of protein A and IgG on/between silver nanoparticles (Figure 6.7). Figure 6.7a shows the region of the micropatterned substrate before exposure to the biomolecular analytes. Smooth and round silver nanoparticles demonstrate uniform phase response of their surface prior to biomolecule adsorption. Following protein A adsorption on the substrate (Figure 6.7b) there is little apparent change in the surface of the particles in either the height or phase images. This is likely due to the small size of protein A compared to the silver nanoparticles and the possibility that the protein has collapsed on the surface of the particles as a result of strong electrostatic interactions.

Finally, the high resolution AFM images following IgG adsorption show roughened nanoparticles confirming that multiple small globules are bound to the surface of the nanoparticles after adsorption with several patches clearly visible on each nanoparticle (Figure 6.7c). The drastic change in both the height and the phase image indicates that IgG is binding to the surfaces of the silver nanoparticles and not just adsorbed on surrounding surface areas. The binding of the biomolecules in close proximity to or on the surface of the nanoparticles is necessary for SERS enhancement to occur. These images indicate that IgG readily binds to the nanoparticles even with the modest concentration (5×10^{-7} M) and short exposure time (30 s) of the IgG used in these experiments.

When concentration and exposure time were increased, multiple layers and complete coverage of the silver nanoparticles on the substrate was observed which completely masked initial domain morphology. The typical Y-shape of IgG is not always visible using AFM because the biomolecule does not always exists in this state as a bound molecule.[330] Globular conformations of bound IgG on surfaces similar to the bound protein shown in Figure 6.7c have been previously shown.[331] The obvious change in the surface topography of the regions of the micropatterned sample containing nanoparticles combined with the previously discussed fluorescence studies clearly indicates that the biomolecular analytes in this study are bound to silver nanoparticles.

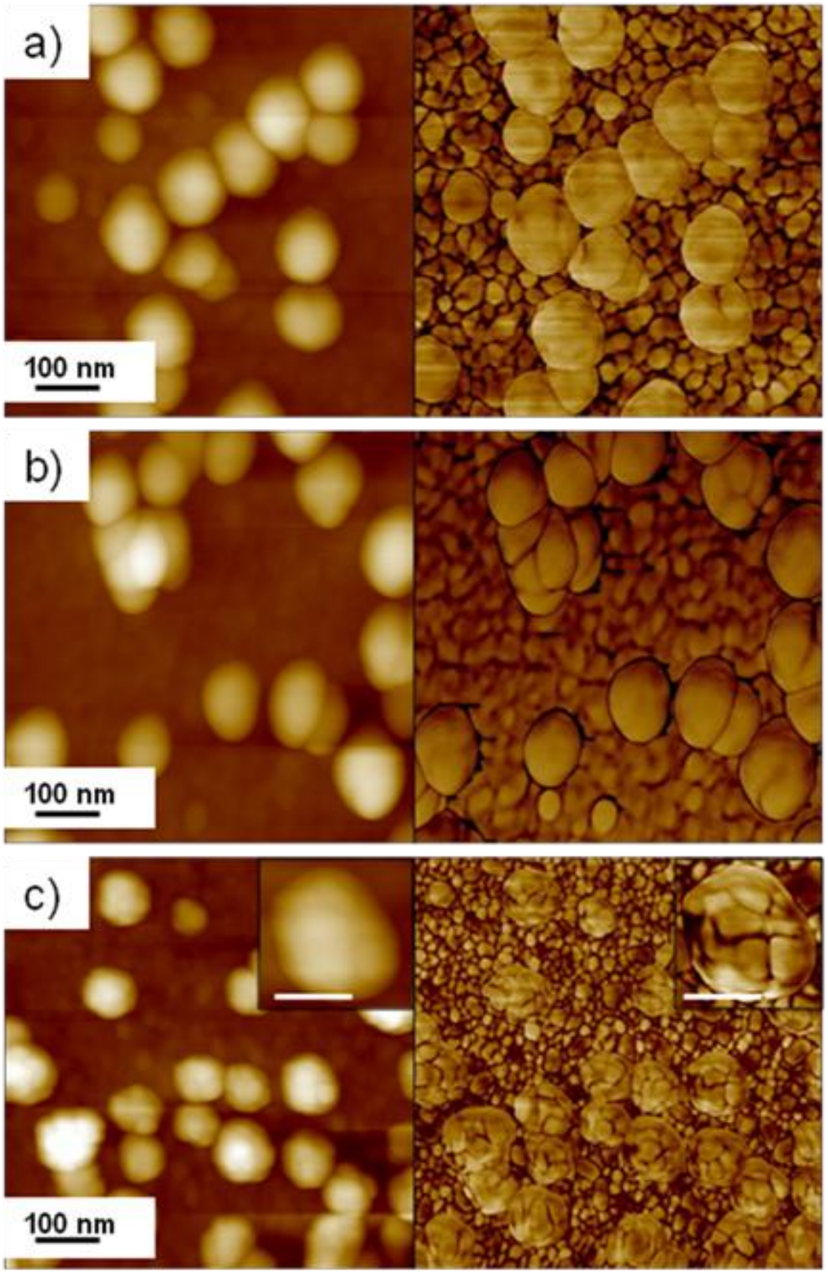

Figure 6.7 High resolution AFM topographical and phase images of the silver nanoparticle regions of the micropatterned substrate (a) before, (b) after protein A adsorption, and (c) after IgG adsorption. The z-scale of all images is 80 nm. The scale bar in the single particle inset is 45 nm.

6.3.3 Raman mapping of adsorbed biomolecules

Raman mapping visualized the selective surface distribution of the adsorbed biomolecules (Figure 6.8). The significant enhancement of the Raman signal of protein A and IgG on SERS substrate is clearly shown in the mapping images. The stripes from the micropatterned substrate can be seen in the mapping images. The peaks of highest intensity in the Raman spectra of the two biomolecules used in this study were mapped across the substrate surface. The peak mapped for protein A (Figure 6.8a) was the 1507 cm^{-1} peak and the peak mapped for IgG (Figure 6.8b) was the 1649 cm^{-1} peak. Figure 6.8c shows an optical microscope image concurrently obtained for the patterned substrate to guide to the location of the striped regions in the Raman maps. The regions of the stripes shown in the figure that do not exhibit a complete and uniform response due to the low concentration of protein A and IgG used in this test.

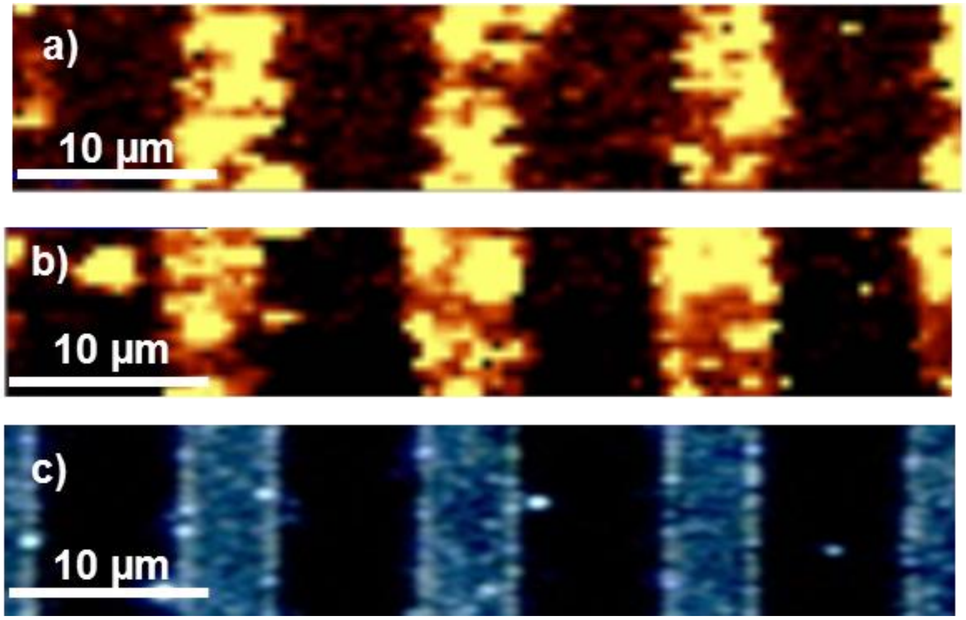

Figure 6.8 SERS mapping of the substrate following (a) protein A and (b) IgG adsorption and (c) an optical image of the substrate to indicate the location of the striped regions in the SERS maps. The peak mapped for protein A was 1507 cm^{-1}, indicative of lysine found in protein A, and the peak mapped for IgG was 1649 cm^{-1}, indicative of the tryptophan ν ring stretching.

The low concentrations of protein solutions used in this study and the very low exposure time (30 s) to the substrate prevented clogging the micropatterned substrate and the formation of relatively thick biofilms with an incomplete monolayer of biomolecules formed on the surface of the nanoparticle-decorated areas. Indeed, cross-sections of AFM images show that the average nanoparticle height increased from 33 ± 4 nm to 38 ± 3 nm following protein A and IgG adsorption, indicating that only about 4 nm of IgG could have adsorbed on the nanoparticle surface, which is less that the diameter of the native biomolecules. Moreover, independent measurements with ellipsometry also confirmed that the increase of the effective thickness associated with adsorbed protein was less than 5 nm thus additionally confirming low surface coverage with biomolecules. When large amounts of IgG were used, the SERS intensity reached a point at which there was no change in intensity on the patterned regions. The substrate was designed for the trace detection of biomolecules so there was limited testing at higher concentrations.

6.3.4 Limit of detection of protein A and IgG

A limit of detection study of protein A and IgG was also conducted using the micropatterned SERS substrate in order to demonstrate that fast, label-free, and trace detection is possible with this substrate (Figure 6.9). The limit of detection of the substrate was determined based on the principle that the peak intensity of the analyte must be greater than background variation by more than a factor of 3.[68] Spectra from the SERS substrate were taken in reflection mode after protein A adsorption and subsequently after IgG adsorption on the surface.

For the IgG limit of detection, the substrate was exposed to a protein A solution of 10^{-8} M in order to prevent the very intense peaks of protein A from interfering with IgG detection. The peak assignment in the SERS spectrum of protein A is proposed based on knowledge of the amino acid sequence of protein A and literature data on characteristic vibrations for different amino acids (Figure 6.9a).[332] The spectral peaks of 1150 and 1507 cm^{-1} can be attributed to lysine and the peak at 1272 cm^{-1} can be assigned to glutamine and asparagine. These three amino acids exist in high concentration in protein A. As a result of the positive charge of lysine, it is thought that this residue of protein A exists in closest proximity to the negatively-charged SERS hot spots leading to a greater contribution to the overall spectrum of protein A from lysine than other residues present.

The characteristic SERS bands of IgG can be also found following IgG adsorption (Figure 6.9b,c). Raman peaks at 1366, 1511, 1574, and 1649 cm^{-1} are indicative of the tryptophan ν ring stretching and the peaks at 1511 and 1574 cm^{-1} also indicate the tyrosine ν ring stretching, which are both the characteristic Raman-active amino acid sequences of IgG.[310] The peak at 1649 cm^{-1} is the most consistent peak seen in the IgG spectra, but seems to be shifted slightly in comparison to literature values. This may be a result of the presence of protein A as an intermediate biding agent, as well as the fact that residues which include α-helical amide I groups from IgG may be bound closed to the silver nanoparticle hot spots than other parts of the IgG molecule.[333] The SERS enhancement of protein A and IgG allows for accurate detection of the presence of these biomolecules while the micropatterned surface provides a platform which specifically binds protein A and IgG in silver nanoparticle hot spot regions. The limit of detection was measured for a stepwise decreasing of protein solutions concentration down to 100 fM (Figure 6.9). For protein A the low limit of detection was determined to be around 5 nM as estimated from peak at 1507 cm^{-1} in accordance with a general procedure described for IgG protein in detail.

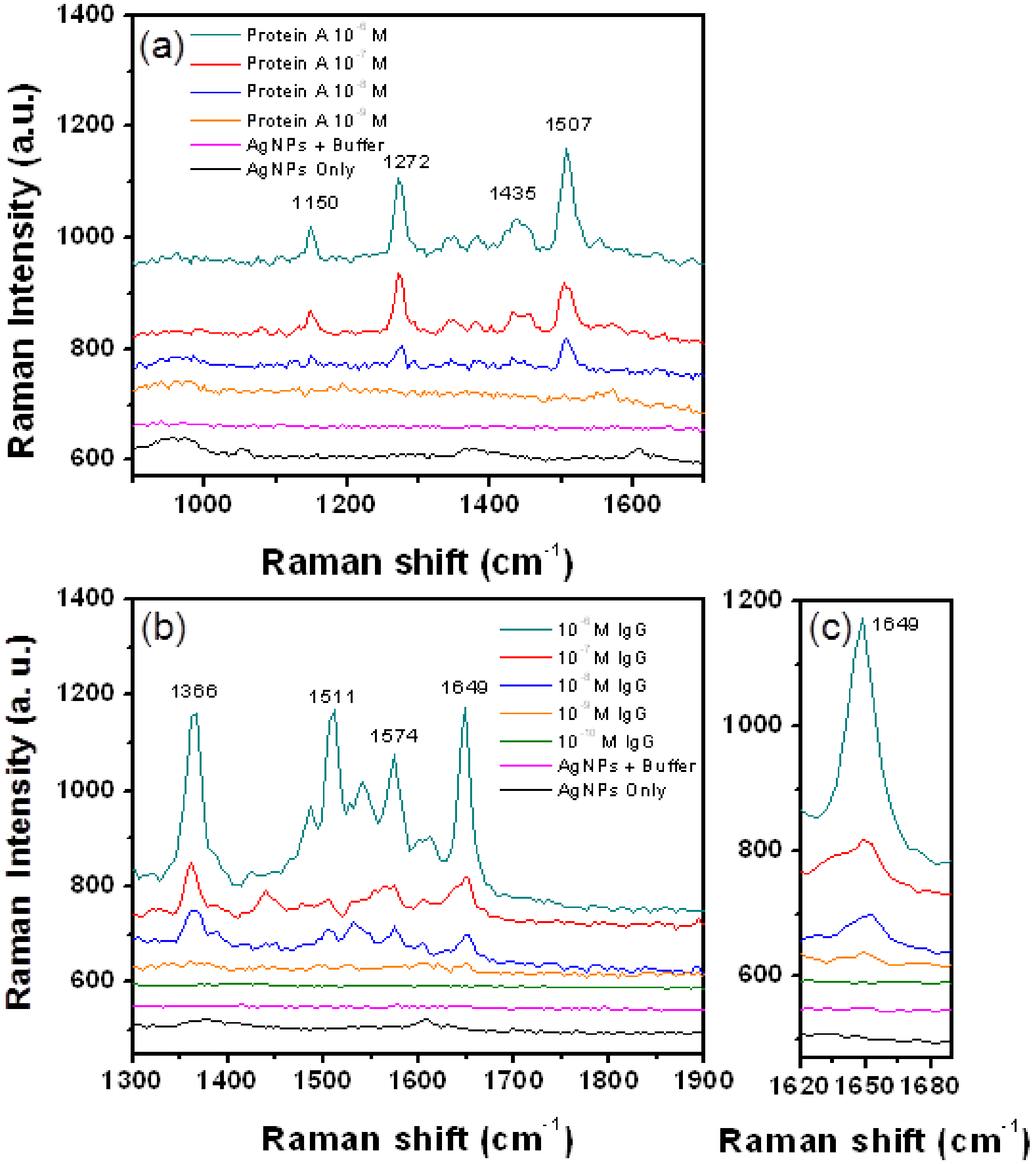

Figure 6.9 SERS spectra of (a) protein A and (b) IgG on the silver nanoparticle substrate compared to references of the neat micropatterned substrate and the substrate following buffer exposure. The characteristic peak of IgG at 1649 cm^{-1} which is used for limit of detection measurements is shown at larger scale (c).

For IgG protein, the Raman peak at 1649 cm^{-1}, was used to follow the adsorption process with a very intense peak observed at 10^{-6} M concentration and only random background observed for 100 fM solution. Increasing the concentration to 10 nM results in the appearance of a strong peak at 1649 cm^{-1}. The peak is less intense, but exceeds the random background level by a factor of 4 at 1 nM and thus gives the evaluation of the lowest detection limit achievable here as well below 1 nM (close to 500 fM). Such a very low limit of detection of non-labeled IgG solution is within common limits of detection of these biomolecules reported in literature with different methods all of which require additional labeling procedure.[334]

This study demonstrates that a nanoengeered substrate composed of micropatterned metal nanoparticles can be exploited for the SERS detection of the important bioanalytes, protein A and immunoglobulin G, at comparably trace levels as can be detected by techniques currently in use.

CHAPTER 7

APTAMER-ASSISTED ASSEMBLY OF GOLD NANOFRAME DIMERS

7.1 Introduction

Gold nanoframes are of particular interest due the wide range of plasmonic tunability in the visible and near infrared range that allows for electromagnetic field enhancement at longer wavelengths which is critical for biological applications.[335,336,337] The use of these aggregated systems has shown particular potential in the field of surface-enhance Raman scattering (SERS) where such assemblies provide well-defined enhanced electromagnetic fields that in turn allow for the possibility of label-free detection of targeted molecules. A well-defined aggregated state of the gold nanoframes is critically important for SERS detection due to the uniform and highly enhanced electromagnetic field located between two particles. Such nanostructures have been previously studied theoretically; however, experimental assemblies have not been shown.[234,338,336]

The controlled aggregation or distance dependent assembly of other nanostructures such as spherical nanoparticles and nanocubes (of either silver or gold) has been realized through lithographic techniques,[204,205] as well as electrostatic,[206] polymer,[70,207] and DNA[208,209] mediated assembly. Many of these techniques are expensive, time-consuming, and require extensive and precise surface modification and ligand exchange procedures, thus limiting their application for large area, high throughput, and easily tailorable substrate fabrication. Current studies frequently lack the high degree of binding selectivity and specific spectral assignments that are possible with label-free SERS sensors.[169] A “planet and satellite” approach has been taken to form hot spots between large central particles and small outer particles,[227,228] however this approach provides limited accessibility of analyte molecules to the hot spot location. A key challenge in the field of SERS detection is to tailor the hot spot region to the analyte of interest to provide a selective and label-free substrate for trace detection. The hot spot design is particularly important in the field of biomolecule detection where many analytes often contain bulky sequences that must be well-understood in order to accurately assign Raman bands and correctly identify the target analyte.

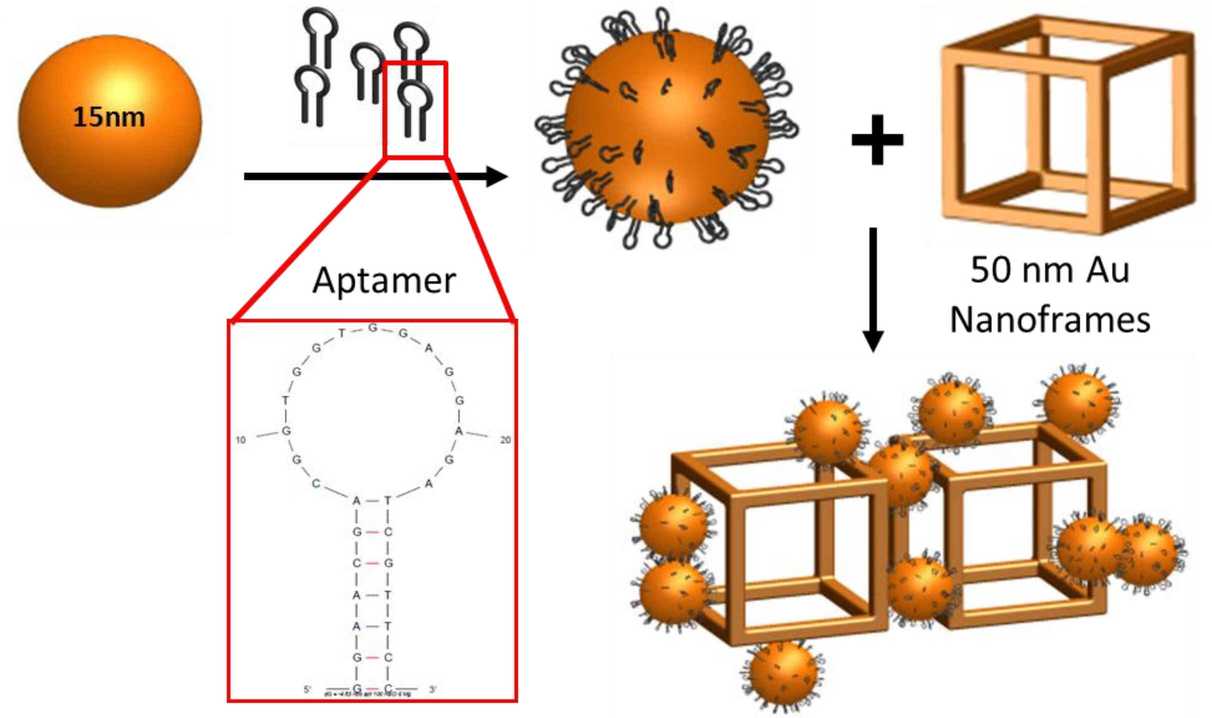

Figure 7.1 Aptamer-assisted hierarchal nanoparticle assembly using nanoparticles and nanoframes with selective binding within SERS hotspots.

In this work, nanoframe dimers are assembled through the electrostatic interaction of oppositely charged nanostructures as mediated by small functionalized nanoparticles (Figure 7.1). A linking spherical nanoparticle provides the critically important and well-controlled binding distance and orientation of nanoframes. The mediating nanoparticles also provide a consistent and specifically targeted binding moiety for biological sensing through aptamer modification. The key feature of the gold nanoframe dimers is the presence of a widened hot spot and coupled plasmonic resonances that allow for a larger region of plasmonic enhancement in which to detect the analyte of interest.

The unique structure and functionality of the aptamer trapped between nanoframes allows it to be used as a capping agent for electrostatic binding of SERS-active gold nanocages while retaining the key selective binding properties needed for targeted detection of specific bioanalytes. Aptamers are relatively short single-stranded DNA or RNA sequences that can bind target molecules with high affinity.[193] These molecules are relatively compact and can be derived chemically, giving them a distinct advantage over antibodies for designing biofunctionalized “hot spots”.[132,133] The target analyte in this study is riboflavin, a representative biomolecule that is a member of the B vitamin group, which can be bound by a selected aptamer.[339,340] The lowest energy folding structure of these single-standed DNA aptamer sequences is determined using the well-developed Mfold software.[144] Also known as vitamin B_2, riboflavin is an important molecule for electron transfer reactions in the body, cell growth, and can even be used as a treatment for some clinical diseases. The riboflavin binding aptamer used in this study was first developed by Lauhon et al.[143] and has been successfully shown to specifically bind riboflavin in previous studies using different detection techniques (Figure 7.1).[15,341]

Indeed, aptamers have also recently been exploited in SERS sensors for the detection of adenosine.[133] This method relies on the controlled nanoparticle junction formed following adenosine binding and shows preliminary detection results for a strong Raman marker, 4-aminobenzenethiol. Huh and Erickson have also demonstrated the use of an aptamer to specifically detect the peptide hormone vasopressin using a fluorescent label as the Raman marker.[135] These studies indicate that nanostructures containing aptamers can provide a powerful tool for biological detection, and thus new designs of such nanostructures with the added advantage of label-free sensing are explored here.

7.2 Experimental details

The riboflavin DNA aptamer used to functionalize the gold nanostructures was obtained from IDT (Coralville, IA) and purified by standard desalting. The riboflavin-binding aptamer sequence is: 5' HS-ACTCATCTGTGAAGAGAG-GAACGACGGTGGTGGA GGAGATCGTTCC 3' (Figure 7.1). Spherical gold nanoparticles were synthesized using the seeded growth approach as has been previously reported and described in Chapter 3.[109] This procedure resulted in spherical gold nanoparticles with diameters of 15 ± 2 nm. A galvanic replacement technique was used to synthesize gold nanoframes from silver nanocube silver nanocube templates, also detailed in Chapter 3.[233] Gold nanoframes were mixed with aptamer-functionalized spherical gold nanoparticles to form controlled aggregate structures for SERS hot spots through electrostatically driven aggregation (Figure 7.1). The electrostatically directed assembly of the nanostructures was promoted by the strong positive charge of the polyallylamine hydrochloride (PAH) capping layer of the gold nanoframes and the strong negative charge of the aptamer-functionalized gold nanoparticles. The nanoframes were functionalized with a PAH layer on top of the polyvinylpyrrolidone (PVP) layer remaining from the fabrication of the gold nanoframes using a process similar to the layer-by-layer assembly technique previously published for silver nanocubes.[342] The PAH layer was necessary to provide a strong positive charge to counter the negative charge of the aptamer capping agent of the spherical gold nanoparticles. The surface density of the apatmer ligand is a critical factor in order to impart functionality to the aptamer rather than just modifying the surface of the nanoparticle. After binding a high density layer of aptamer to the surface of the nanoparticles, 6-mercaptohexanol was then used to displace some of the aptamers to provide the space required for proper selective binding function.

The mixed aggregated solutions of gold nanoframes and aptamer-functionalized gold nanoparticles were then dropcast on the cleaned silicon from dilute solutions in order to minimize drying effects on the aggregate size and composition. Characterization was performed on the nanostructures to monitor dimerization with UV-Vis-NIR spectroscopy and Zeta-potential (Chapter 3). The nanoparticle solution was added to a gold nanoframe solution in 100 µL aliquots for step-wise measurements. Also, 200 µL of 10^{-3} M magnesium sulfate was added to promote aggregation as a passivating ion.

Atomic force microscopy (AFM) scanning (Chapter 3) of the spherical gold nanoparticles before and after aptamer binding was conducted to verify the change in surface ligand size. TEM was performed to determine the gold nanoframe and gold nanoparticles sizes as well as their morphology (including edge rounding) and the degree of aggregation of the final product. The edge rounding factor is defined as the edge radius scaled by the length of the nanocube. For the detection of riboflavin within the Raman active hot spot, confocal Raman microscopy with a 785 nm laser was employed as the incident light beam and a 100x objective lens with 1 second integration time. For sample preparation, the mixed solution of nanoframes and aptamer-nanoparticles was premixed with the riboflavin analyte (from 100 µM to 1 µM) for 1 hour followed by centrifugation. The supernatant containing unbound riboflavin was removed and the pellet was dispersed in water and dropcast on a silicon wafer for Raman analysis.

Simulations of the extinction spectra of gold nanoframes and their dimers were done using commercially available software from Lumerical Solutions Inc. (FDTD Solutions, 8.0.2). For gold permittivity, we used material data from Johnson and Christy.[261] The permittivity was fitted with six coefficients and an RMS error of 0.24. The water permittivity data was taken from Palik[343] and had an RMS error of 0.005. A simulation mesh size of 0.5 nm (single nanoframe simulations) and 1 nm (dimer simulations) was chosen and the second conformal variant mesh refinement was used. For the best simulation stability, the mesh area was chosen to be 120 nm larger than the existing structure in all three principal directions. All simulations reached the auto shut off level of 10^{-5} before reaching 100 fs simulation time. The perfect match layer (PML) method was use for boundary conditions.

7.3 Results and discussion

7.3.1 Nanostructure characterization and functionalization

AFM analysis of spherical nanoparticles before and after aptamer binding showed individual round nanoparticles uniformly dispersed on a substrate that indicated no aggregation in solution (Figure 7.2). The diameter of bare nanoparticles with the organic ligand (CTAB) was 15 ± 2 nm in the dry state. The DNA aptamer for riboflavin was attached to the spherical gold nanoparticles using an adopted procedure from Liu et al.[237] Essentially the aptamer was modified at the 5' end with a thiol group to bind to the gold surface as well as a random 18 nucleotide sequence to provide a spacer between the active portion of the aptamer and the gold surface allowing for proper function. After aptamer grafting, the nanoparticle diameter increased to 19 ± 2 nm thus confirming the presence of the additional shell (see corresponding cross-sections in Figure 7.2e). The UV-Vis spectra (Figure 7.2f) of the spherical gold nanoparticles before and after aptamer adsorption showed no peak shift or broadening indicate that very little aggregation occurred meaning individual nanoparticles were functionalized and can be used for subsequent electrostatic binding.

Zeta-potential measurements additionally confirmed the successful grafting. These measurements showed a change in the surface charge of the spherical nanoparticles with the positively charged CTAB ligand from +46.8 ± 10 mV to -30.3 ± 5 mV after the nanoparticles were modified with the negatively charged DNA aptamer. As discussed previously, the gold nanoframes are additionally coated with a monolayer of PAH in order to impart a positive charge with +13.2 ± 7 mV potential. The opposite charges of the aptamer-gold nanoparticles and the gold nanoframes then facilitate controlled aggregation into predominantly dimer structures due to close to zero charge balance of these nanoparticle-dimer aggregates.

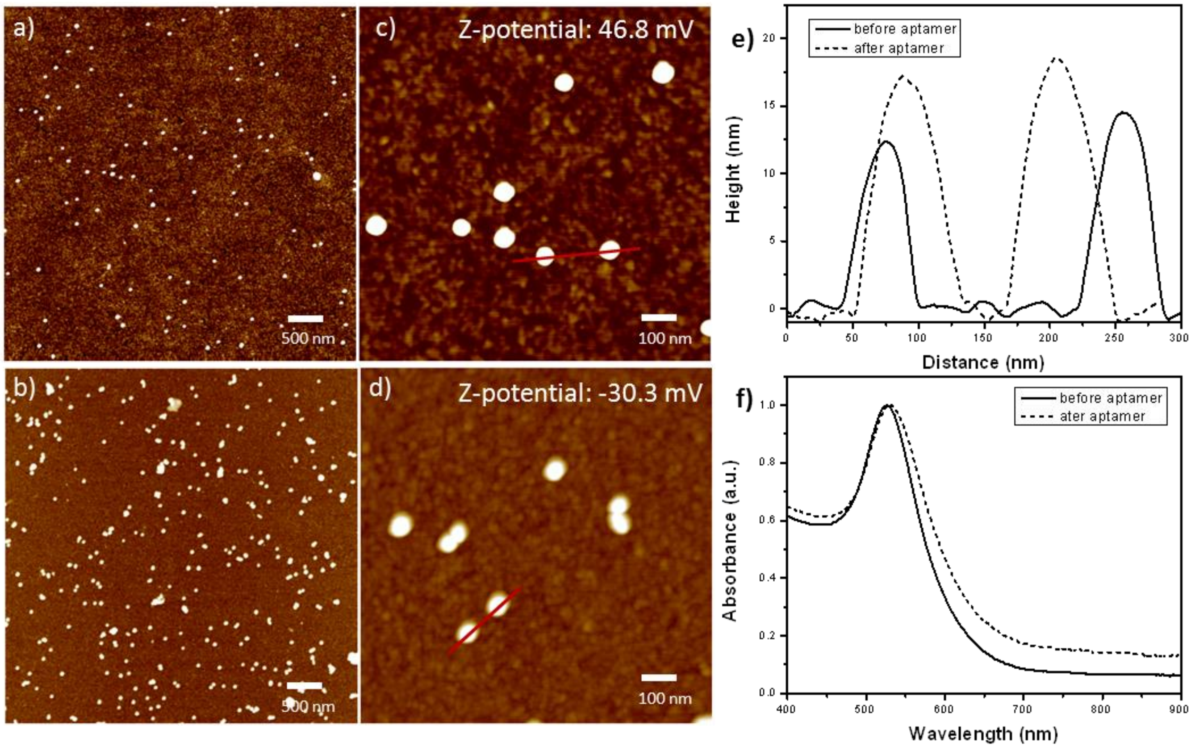

Figure 7.2 AFM topography images of gold nanoparticles before (a,c) and after (b,d) aptamer functionalization, corresponding cross-sections (e), and UV-Vis absorbance (f).

7.3.2 Dimer fabrication and characterization

In order to achieve controlled dimer aggregation, a ratio of 4:1 spherical nanoparticles to nanoframes was used. A small amount of magnesium sulfate was used in the mixing process to provide a passivating ionic solution which will promote aggregation and stabilize nanoframe dimers as has been shown previously.[206] This ratio was found to be advantageous for dimer formation and avoiding aggregation by testing different nanoparticle concentrations. A larger number of aptamer-functionalized nanoparticles compared to nanoframes were likely required because of the much smaller size of the spherical gold nanoparticles and differences in nanostructure solution concentrations. Also, higher target (riboflavin) binding can be promoted through a greater number of aptamer-coated gold nanoparticles within gold nanoframe hot spots.

7.3.2.1 Optical properties of controlled aggregates

UV-Vis-NIR spectroscopy confirmed a dramatic change in the plasmonic behavior of the mixed nanostructure solution as dimer aggregation occurred. In order to monitor the dimerization and gradual aggregation of the nanostructure system, the aptamer-functionalized gold nanoparticles were added in small aliquots (100 µL) while absorbance was measured after each addition, as shown in Figure 7.3a. The broad nature of the absorbance spectra is likely a result of the variable aggregated states, rounding of the corners and edges of the gold nanoframes, and the close proximity of the spherical nanoparticles between and surrounding the nanoframe dimers. There is a visible increase in the peak at 530 nm that corresponds to the addition of spherical gold nanoparticles while there is a broadening and dramatic red shift of the 965 nm nanoframe peak to 1040 nm indicating progressing aggregation of dimer pairs leading to a gradual increase in plasmonic coupling between the gold nanoframes and spherical gold nanoparticles. The evolution of two additional minor peaks at 935 and 1160 nm after the final addition of aptamer-functionalized gold nanoparticles can be attributed to the dimerization of the gold nanoframes in various orientations as concluded from finite-difference time-domain (FDTD) modeling (see below) (Figure 7.3b).

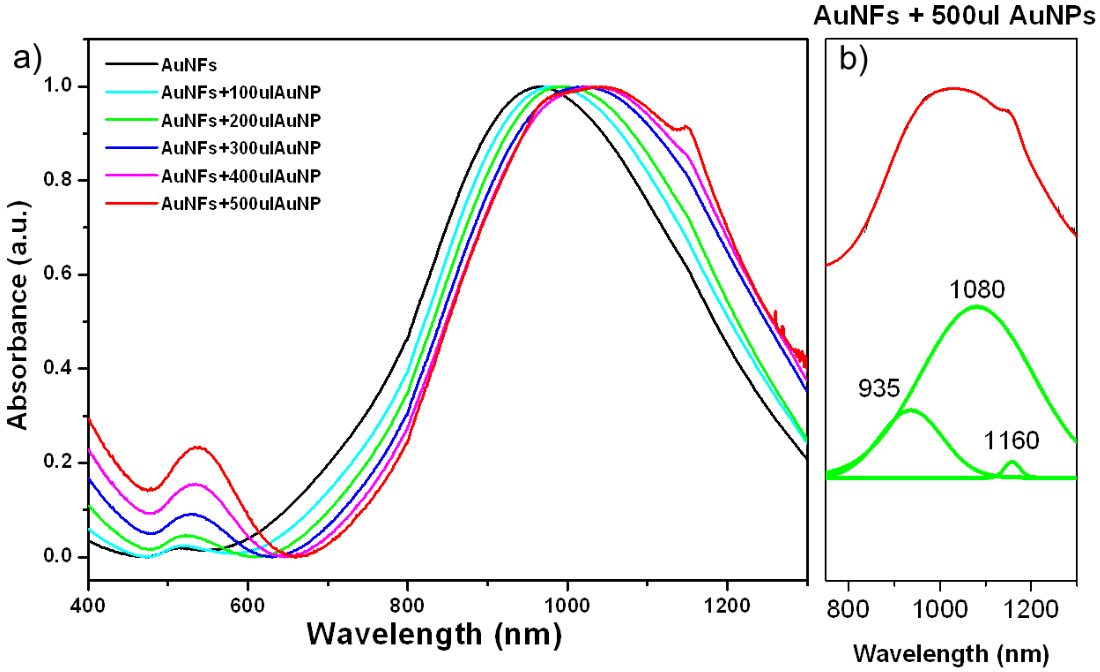

Figure 7.3 (a) UV-Vis-NIR spectra of gold nanoframes with increasing volumes of aptamer functionalized gold nanoparticles and (b) peak deconvolution of the final nanostructure mixture resulting from the dominant edge-to-edge dimer configuration.

7.3.2.2 Electron microscopy and plasmonic modeling of dimers

Transmission electron microscopy (TEM) of the mixed nanostructure solutions of gold nanoframes and aptamer-functionalized gold nanoparticles showed a variety of aggregates with different aggregation numbers, nanoparticles present, gap dimensions, and nanoframe orientations (Figure 7.4). However, statistical analysis of more than 100 aggregates showed that vast majority of aggregates formed dimers. Indeed, more than 50% of all nanostructured aggregates were dimers of gold nanoframes, which indicated a fairly high yield given the use of only electrostatic binding for dimerization. The TEM images show that the spherical nanoparticles have a tendency to bind to the edges and corners of the gold nanoframes, resulting in an average of approximately 2 spherical nanoparticles for each dimer pair that provide a greater number of functional targeting molecules within the widened hot spot. The TEM images also show a very small number of nanoframes that contain impurities within the frame indicating incomplete etching during synthesis; however, these structural impurities are not considered to provide a large contribution to the overall SERS enhancement of the system and are not considered in simulations. Moreover, statistical analysis shows that when the nanoframe dimers form, there are consistently three representative nanoframe arrangements dominating the overall picture: face-to-face, face-to-edge, and edge-to-edge. The majority of dimers (80%) form face-to-edge and edge-to-edge orientations likely as a result of the spherical gold nanoparticles that are bound between the gold nanoframe pairs.

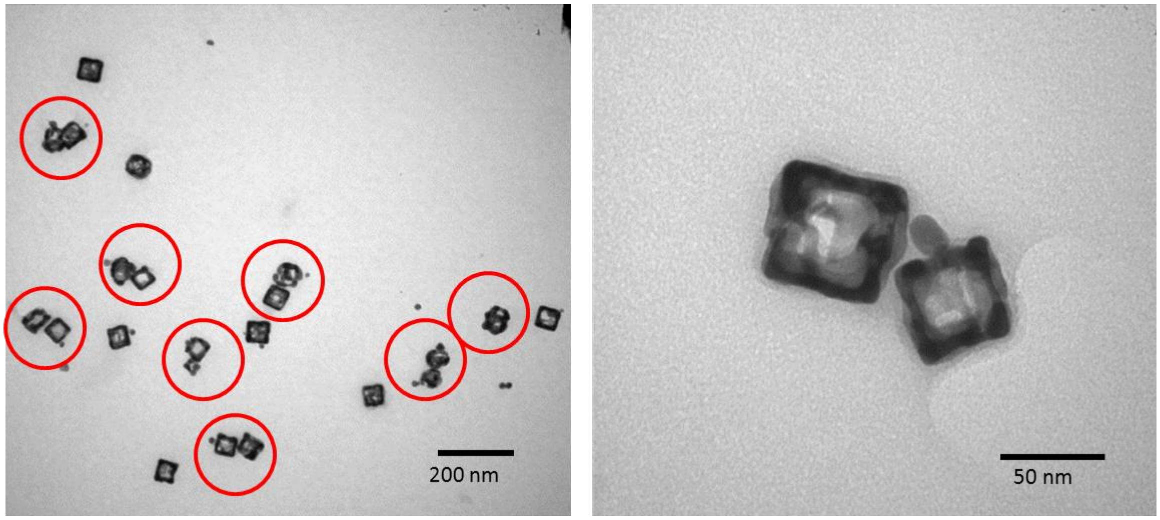

Figure 7.4 TEM images of gold nanoframe dimers electrostatically assembled using aptamer-functionalized gold nanoparticles.

Therefore, these three different nanoframe orientations were used for modeling the plasmonic signature of aggregated nanoframes important for their SERS behavior (Figure 7.5). In comparison with previous publications regarding nanoframes, we improved our simulation by using cylindrical edges and spherical corners instead of rectangle edges and corners to be closer to the real nanostructures.[335,338] The nanoframes were constructed using cylindrical edges and spherical corners for following FDTD simulations to recreate actual morphologies with actual dimensions from the observed TEM images. The gold nanoframe wall thickness was found to be approximately 11 ± 3 nm with some variation in thickness along the edges.

The simulated plasmon resonances for all three orientations show two major peaks which correspond to conventional transversal and longitudinal modes of frame elements and edge-to-edge dimers showing red shifts and broader peaks.[344] The simulated peak for 15 nm spherical gold nanoparticles is also included in the plot for reference. The simulated resonance peaks are much sharper compared to the broad experimental absorption peak with dramatic broadening of the experimental peak caused by the variable wall thickness and edge waviness. Indeed, the simulated results of different wall thicknesses show that even small changes of around 1 nm in wall thickness results in a peak shift between 60 and 95 nm. Consequently, the plasmonic resonances should be

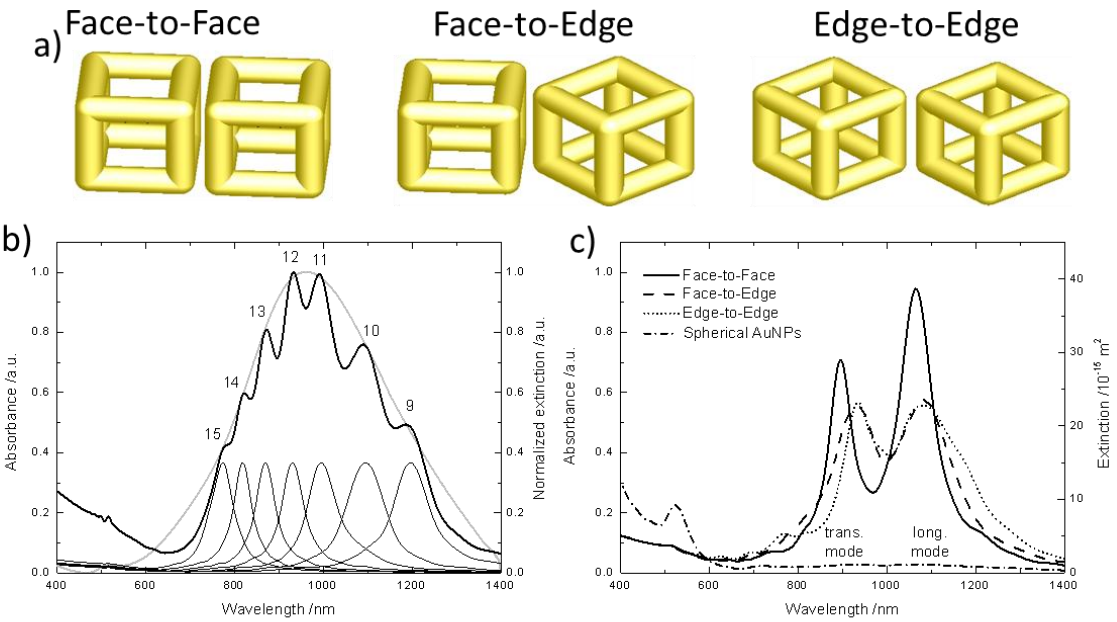

Figure 7.5 (a) Models of gold nanoframe aggregation conditions, (b) FDTD method modeling to describe the characteristic plasmonic behavior of gold nanoframes resulting from wall thickness variation and (c) the evolution of the 935, 1080, and 1160 nm peaks based on the orientation of gold nanoframe dimers and the spherical gold nanoparticle spectrum for reference.

significantly broadened for actual nanoframes due to varying wall thickness. In addition, the peak width is a result of the imaginary part of the dielectric constant (damping) used in the simulation, which is caused by interband transitions for which additional correction could be made by using the Drude model correction[345] or a quantum-corrected model,[346] which is beyond the scope of this study.

In order to accommodate these very sensitive parameters, statistical analysis of TEM images was used to estimate a weighting function to combine different modeled sizes of rounded nanoframes that allows for the accurate description of the experimental peak location. The experimentally measured and modeling weight functions varied slightly likely as a result of uncertainties in measuring the wall thickness; however both the measured and fit curves follow the same trend and the difference in average value was statistically insignificant.

The deconvolution of the final mixed nanostructure solution UV-Vis-NIR spectrum shown in Figure 7.3b shows the presence of three characteristic peaks at 935, 1080, and 1160 nm which are identical to the peak positions shown for the edge-to-edge configuration modeled in Figure 7.5. The broad nature of the experimentally observed spectrum indicates that all configurations of gold nanoframe dimers likely contribute to the overall plasmonic behavior. The modeling shows that upon aggregation into dimers, the experimentally observed coupled plasmonic peak splitting can be qualitatively described by the three configurations used in simulations (Figure 7.5). This indicates that the primary contribution of the experimentally observed extinction spectrum of the aggregated particles is a result of the dimerization of gold nanoframes due to electrostatic interactions with aptamer-coated gold nanoparticles.

7.3.3 Verification of selectivity and specificity using SERS

In order to provide a preliminary test of the SERS properties of the nanoframe dimers, the nanoframe solution was exposed to solutions of riboflavin with concentrations ranging from 100 µM to 1 µM, a specific targeted analyte for the aptamer exploited in this study.[143] The selective binding properties of the aptamer should allow for the direct localization of the analyte of interest in hot spot regions between the nanoframes forming the dimer. Figure 7.6a shows that the reference spectrum of the gold nanoframes combined with the aptamer-coated gold nanoparticles has very little signal interference with the characteristic riboflavin peaks, therefore facilitating trace level detection. The reference spectrum of gold nanoframes alone exposed to 100 µM riboflavin also shows that there is little enhancement from the gold nanoframes alone indicating the necessity for dimerization and the presence of a targeted (aptamer) approach for selective sensing. When the gold nanoframe dimer system was exposed to two different bioanalytes (epinephrine and serotonin) that are also important stress-related biomarkers, there was no detectable signal which demonstrates the inherent specificity of the aptamer targeting agent.

The riboflavin SERS spectrum exhibits a range of peaks that can be attributed to riboflavin using literature values as well as through comparison to the reference bulk riboflavin spectrum. Detailed analysis of the enhanced Raman spectrum of riboflavin from the literature and has been used for riboflavin peak assignments.[347,348] The weak intensity bands located at 748 and 794 cm^{-1} can be attributed to ring breathing and bending of the nitrogen containing rings.

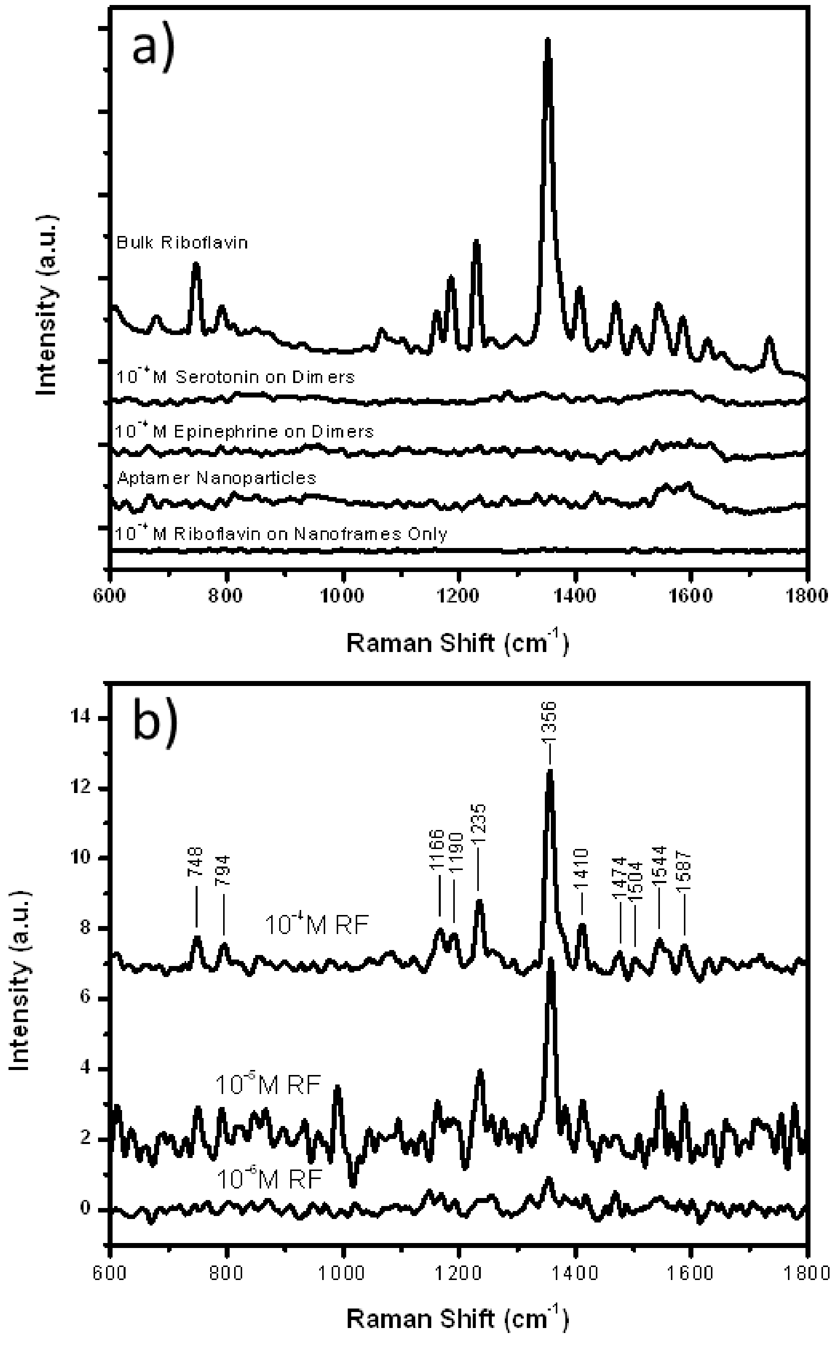

Figure 7.6 (a) Raman spectral comparison of gold nanoframe-gold nanoparticle dimer references with riboflavin on nanoframes only, aptamers on gold nanoparticles reference, epinephrine and serotonin on gold nanoframe-gold nanoparticle dimers, and bulk riboflavin. (b) Limit of detection study of riboflavin on aptamer-functionalized nanostructure dimers with concentrations ranging from 100 µM to 1 µM as well as major peak assignments.

The peaks at 1166 and 1190 cm^{-1} are a result of in-plane aromatic ring bending vibrations. The medium intensity peak at 1235 cm^{-1} is from twist bending vibrations of C-H and O-H groups. The very strong peak at 1356 cm^{-1} as well as the weaker peaks at 1410 and 1474 cm^{-1} can be assigned to carbon-nitrogen and carbon-carbon stretching. Finally, the peaks at 1504, 1544, and 1587 cm^{-1} are due to carbon-nitrogen, carbon-carbon, and carbon-oxygen stretching. Small shifts in peak positions are expected for complex binding situations such as in the different dimer pairs. The intensity and position of the described peaks is highly dependent on the orientation of the bound riboflavin molecules and the nature of substrates. The spectra in Figure 7.6b most closely match the orientation of riboflavin functional groups expected on gold surfaces.[348]

The SERS enhancement factor for this design cannot be estimated easily because of widely varied assumptions such as the exact number of riboflavin molecules located in the hot spots. Therefore, in order to estimate to sensitivity of these nanostructures we rather use the alternative method of the direct experimental measurement of the accessible detection limit by detecting several solutions with diminishing concentration (Figure 7.6b). The intensity change of the characteristic peak at 1356 cm^{-1} with decreasing concentration indicates the viability of this gold nanoframe dimer system as a sensor for trace detection of bioanalytes with a limit of detection of 1 μM for riboflavin as determined by a signal to noise ratio greater than 3:1. This practical ambiguous result indicates that the SERS design proposed is capable of trace detection on a level better than most of alternative methods reported to date.[143] These results indicate that the widened hot spot of the gold nanoframe dimer properly allows for the specific binding of riboflavin molecules to the aptamer targeting molecule grafted to the gold nanoparticles at very low concentration and demonstrate the potential of such dimer nanoframe designs for practical biological sensing applications.

A novel design for biological sensing with potentially high selectivity has been suggested here with aptamer-functionalized gold nanoparticles used as a dual purpose element to both create a widened nanostructure hot spot by electrostatically dimerizing gold nanoframes as well as binding the analyte of interest within a hot spot for trace SERS detection.

CHAPTER 8

GENERAL CONCLUSIONS AND BROADER IMPACT

8.1 General conclusions and discussion

The design of effective and applicable SERS sensors requires that the sensing platform be reliable and consistent, highly selective for the specific analyte of interest, incorporate plasmonic hot spots composed of noble metal nanostructures that are highly enhancing, and be cost effective and easy to use in the field of application. In order to transition this sensing technology into the field of biological and medical diagnostics, these sensing substrates must additionally be biocompatible, effective for the detection of larger molecules (proteins), bind biomolecules in their natural conformation so as not to denature the molecule, and also be able to detect biomolecules across the range of physiologically relevant concentrations. In this study, two specific task were addressed to direct the field of SERS sensing technology in the design of substrates:

1) a detailed analysis of the underlying phenomena that relate to electromagnetic and chemical enhancement mechanisms and how the enhancement can be effected and maximized by tuning the characteristics of the three-dimensional plasmonic substrate including pore dimensions, and particle size, shape, location, and aggregated state,

2) the development of highly controlled SERS sensing platforms that allow for the selective, sensitive, and label-free detection of biomolecules and non-resonant organic molecules.

A detail study of how the physical characteristics of silver nanostructures in porous alumina membrane substrates can affect the electromagnetic enhancement was conducted. This work demonstrated the extremely high enhancement factors that can be achieved using three-dimension SERS substrates even when detecting non-resonant chemical species. This study considered both experimental data from the z-distribution of Raman scattering and simulated results on electromagnetic field distribution for alumina membranes decorated with silver nanoparticles. We can conclude that *one of the significant finds of this study is the optimization of Raman activity for long cylindrical pores can be achieved by choosing a diameter of cylindrical pores around 350-400 nm and a total depth of 10-14 µm.* SERS substrates fabricated from porous alumina membranes with 355 nm pore diameters exhibited enhanced SERS activity by achieving increased transmission of light through the membranes in addition to the inherent waveguiding properties associated with alumina membranes. The Raman enhancement for the substrates with 355 nm pore diameter is ~10^{10} and 10^6 for the common Raman marker benzenethiol and the non-resonant, stealthy molecule perchloric acid, respectively. The enhancement factor observed is several orders of magnitude higher than that reported for traditional two-dimensional substrates and random porous solids.

The approach described here provides an efficient pathway for further development of nanoporous and holey designs, which can allow the detection of trace concentrations of not just known Raman markers, but also practical target molecules with low Raman cross-sections such as explosives, hazardous chemicals and gases, and biomarkers. *This was demonstrated by the record limit of detection for n-methyl-4-nitroaniline, a binder and stabilizing agent in plastic explosives that can easily off-gas during storage, in the vapor phase of 3 ppb.* This work provided specific design criteria regarding substrate characteristics such as pore size, light penetration depth, and nanostructure type as they relate to electromagnetic enhancement; however, it was clear that additional work was required in order to fully understand the binding mechanisms and molecular orientation effects on the chemical enhancement of important analytes.

The bonding interaction of the analyte, in particular non-resonant analytes, can influence the overall SERS enhancement and is a critical factor to consider when developing a sensing device. Chemical enhancement during SERS detection can be described as a combined effect of the charge transfer mechanism, the molecular resonance mechanism, and the non-resonant chemical mechanism. The first two are the most dominant and occur often with resonant molecules, but play a lesser role when detection non-resonant species. In this study, perchloric acid was used as the target analyte and the non-resonant chemical mechanism was found to be the dominant mechanism for chemical enhancement. *The key discovery in this work was the finding that the non-resonant chemical mechanism for chemical enhancement of perchloric acid bound to silver nanoparticles was dependent on the size of the silver cluster, the orientation of the perchloric acid molecule, and the exposed face of the silver nanoparticle.* As the silver nanoparticle cluster size increased, the level of Raman enhancement due to the non-resonant chemical mechanism was found to increase due to a higher degree of particle-analyte interaction which maximized its possible contribution to the overall SERS enhancement.

It was also found that the highest level of enhancement occurred when the perchloric acid bound to the silver surface through oxygen atom on the (111) crystallographic plane of the silver nanostructure. Although other crystal faces have higher energies, they are much less likely to occur on spherical silver nanoparticles as confirmed with HRTEM and likely contribute little to the real experimental enhancement. These results indicate the role of the non-resonant chemical mechanism and how to modify the SERS substrate design to enhance these contributions. Understanding the molecular interaction at different exposed crystal faces will allow for a better understanding of optimal SERS designs for the transition to bulky biomolecules.

Next, we focused on the development of a nanoengineered substrate composed of micropatterned metal nanoparticles that can be exploited for the SERS detection of the known bioanalytes, protein A and human immunoglobulin G (IgG). The amine-terminated nanocoating prevents the surface adsorption of positively charged protein A across the surface except the selective patterned regions containing negatively charged silver nanoparticles. In turn, protein A facilitates subsequent selective adsorption of IgG on predetermined regions. SERS detection was made possible by the high concentration of hot spots, which occurred between the densely packed silver nanoparticles.

This design possesses advantages over current methods such as ELISA, SPR, and FRET, which include label-free and fast detection using a simple and cost effective substrate fabrication technique. *The most critical finding using this approach is the accurate, sensitive, and more selective detection of protein A and IgG than current protein detection methods with the lowest limit of detection for IgG protein solution of below 1 nM, which is comparable to the sensitivity of traditional optical biosensing methods that require much more complicated and time-consuming labeling and indirect detection steps.* An additional clear advantage of this highly sensitive SERS method on an engineered substrate is the speed of detection and simple substrate preparation. Moreover, this method does not require several binding and purification steps as in ELISA which can take hours to complete. Simple exposure of the substrate to the biomolecule solution allows for rapid SERS detection in less than 30 minutes. This method is also cost-effective in that fluorescently-labeled proteins are not required for detection.

The robust and label-free detection of the positively-charged protein A is based on electrostatically-driven selective bounding to regions containing the negatively-charged silver nanoparticle hot spots and thus can be applied to a wide variety of proteins properly (positively, for this design) charged. Micropatterned SERS substrates with defined and functionalized enhanced regions have the potential to provide a simple, fast, label-free, selective, and economical substrate for the Raman mapping of a wide range of adsorbed biomolecules. We suggest that such organized structures with a high density of hot spots could also be utilized for the detection of low concentration protein solutions in clinical, forensic, industrial, and environmental laboratories.

Finally, we developed a biological sensor with a key focus on promoting controlled hot spot fabrication that allows the binding of bulky biological analytes within SERS activated enhanced region. *A novel development in this work was that directed gold nanoframe dimerization resulting in widened enhanced regions for SERS detection of bulky biomolecules was demonstrated experimentally for the first time and described and confirmed through detailed UV-Vis-NIR spectroscopy and TEM analysis combined with finite-difference time-domain modeling*. Gold nanoframe dimers were shown to provide a high SERS enhancement without interfering with the riboflavin spectrum and detection was demonstrated down to 1 μM. The controlled aggregation and highly-specific localization of the targeted analyte in this nanostructure assembly approach provides a much higher degree of target specificity than can be achieved with current bio-SERS sensors with non-specific organic ligands.

The findings in this work related to the electromagnetic and chemical enhancement effects with three-dimensional SERS substrates, the identification of the characteristic properties of the substrate that can be tailored to maximize these enhancement factors, and the application of this knowledge to design biological SERS substrates with high selectivity and specificity may lead to signification impacts in the field of SERS detection and sensor design as described in the following section.

8.2 Significance and broader impact

The further development of sensor technologies will require progress in the implementation of sensing mechanism that are label-free, sensitive, fast, non-invasive, and highly selective for target analytes. One such sensing technique is surface-enhanced Raman scattering, which is highly advantageous due to its inherent signal specificity as a result of the direct identification of chemical functional groups, its portability, and speed of detection. However, due to the low signal intensity cross-section of Raman detection compared to other techniques such as fluorescence, this method has shown little application in current fast-growing fields such as biomedical, environmental, and chemical detection. In order to provide the needed technological developments to establish SERS as a useful sensing platform, the understanding of its underlying enhancement phenomena as well as the integration of novel nanotechnology and biochemistry must be employed in future SERS substrate design. *These goals are accomplished in the present study through a detailed analysis of substrate and nanostructure characteristics that can be manipulated to affect both electromagnetic and chemical enhancement and the design of functionalized widened hot spots for biological detection and arrayed protein sensors.*

Table 8.1 shows a list of issues facing the application of SERS sensors for real-world detection that was compiled from articles by several leading experts[120,349,350] and the specific solutions to these issues that have been described in this work. As is widely accepted, the critical issue for SERS sensor application is the reliability and comparability between different substrate designs and this includes the materials choices for both the substrate platform and the plasmonically-active enhancing element, the fabrication approach for the sensor, the complete characterization of the specific sensor design including the fundamental design parameters needed to maximize enhancement, and the expansion of SERS detection into real-world fields with a variety of target types including chemical, environmental, and biological molecules.

Table 8.1. The critical issues and possible solutions for improved SERS sensor design and application.

Grand Challenges in SERS Sensors	Progress and Novelty in this Work
Materials	> Use of silver and gold nanostructures with spherical, cubic, and frame shapes for expanded plasmonic tunability. > Development of three-dimension porous alumina membranes for optical clarity and waveguiding properties.
New noble metal nanostructures and substrate platforms with unique plasmonic properties.	
Fabrication	> Established specific criteria for control of cluster size and aggregated state for silver nanocubes in PAMs. > Micropatterned silver nanosphere arrays for spacial control of enhanced regions. > Gold nanoframe dimerization for specific widened hot spot design.
New robust techniques for patterning, nanostructure depositon, and analyte exposure.	
Fundamentals	> Developed guidelines to maximize electromagnetic enhancement related to substrate and nanostructure physical properties. > Relate the chemical enhancement mechanisms related to the intentional enhancement of non-resonant molecules.
Deeper understanding of underlying phenomena related to enhancement and how they can be manipulated.	
Targets	> Developed highly enhancing 3D substrate to detect the "invisible" perchloric acid. > Used a protein-A functionalized micropatterned substrate for the nM detection of IgG. > Produced apatamer functionalized gold nanoframe dimer hot spots for μM detection of riboflavin.
Enhance the application of Raman spectroscopy by determining methods for detection of analytes in new fields.	

Materials selection plays an important role in any device fabrication and this holds true for SERS sensing platforms. Historically, the typical SERS substrate has transitioned for roughened silver electrodes, to metal nanostructures randomly deposited on surfaces, to solution-based metal nanoparticle-facilitated detection, and now to more advanced three-dimensional constructions. *The significance of the transition to the third dimension is the ability to excite many noble metal nanostructure hot spots within the laser footprint leading to record enhancement factors and highly consistent measurements over large area substrates for the detection of non-resonant molecules.* The unprecedented level of enhancement (EF=10^{10} for electromagnetic enhancement only) that can be achieved using the porous alumina substrates in this work is a direct result of novel sensor design using the specific advantageous materials properties of the substrate components. This includes the significant waveguiding characteristics of alumina which results in multiple reflections through large (greater than 10 µm) depths of pores and multiple hot spot excitation events. The enhancement is also a direct result of the plasmonic material selection of extremely dense electroless-deposited silver nanoparticles or highly-ordered silver nanocube aggregates throughout the pore depth.

These three-dimensional substrate designs with controlled nanostructure clusters will have a *broad impact in future SERS sensor design and detection technologies as a result of their record high enhancement factor and ability to detect stealthy, non-resonant molecules at low concentrations.* These devices have implications across all detection fields including military monitoring of explosive storage and in-the-field detection, flow sensors for biomedical applications, and continuous environmental monitoring with real-time readout.

The fabrication of SERS substrates must also be advanced in order to become useful in modern detection systems. This includes both the fabrication of the sensing platform as a whole and the assembly of the nanostructured hot spot junctions within substrate while keeping in mind that the ultimate goal for the broad application of SERS is to maximize the overall signal enhancement. For this purpose, the design of controlled hot spots that are tailored to the analyte of interest is a critical development for SERS sensing. *A truly novel approach for hot spot formation was developed that utilized an aptamer ligand not only as the biorecognition element that imparted specificity to the target, but also as the mechanism for widened electrostatic hot spot assembly.* The plasmonically-active material was also significant for the field as the electromagnetically enhanced region of gold nanoframe dimers is much wider (greater than 10 nm) than typical nanostructure aggregates and can allow large biomolecules to bind within this region. This approach provides a unique sensing design that could have a great impact for future biomedical sensors. The interesting assembly mechanism of this approach can provide an extremely high degree of specificity depending on the analyte as well as a high level of signal enhancement and detailed label-free detection.

For simplified biodetection designs, the micropatterned substrate developed with silver nanoparticles with specifically-functionalized detection areas can allow for the simultaneous detection of the analyte and non-specific background adsorption of biomolecules for real-time analysis. This method provides an element of simplicity that makes it an attractive alternative for current point-of-care assessment techniques. The selectivity that can be added by functionalizing the metal nanostructures also demonstrates the unique ability of such a sensing platform to be used in complex physiological fluids. This micropatterned design can be used as a basis for future substrate fabrication as the patterned nature of the detection scheme could allow for multiplex detection of different biotargets simultaneously.

In order to advance the knowledge in the field of SERS detection and sensor design it is imperative that the fundamental enhancement phenomena related to electromagnetic and chemical elements be understood and studied in the context of sensors utilizing the third dimension. The complexity added by multiple laser reflections through vertical pores that allows multiple interactions with nanostructure hot spots was a critical goal for this study and has significant implications in the developing guidelines for SERS sensor design. *The work presented here shows, for the first time, a detailed study of the electromagnetic enhancement of silver nanosphere and silver nanocube clusters through empirical measurement and confirmed through simulation.* The analysis of solely the electromagnetic portion of the enhancement allows this substrate to be compared with other current state-of-the-art designs and proves that the highest overall enhancement can be achieved in three-dimensional substrates as a result of the much larger area of signal collection within the laser excitation footprint. This research also provides a basis for future progress in the field of organized three-dimensional SERS sensor design by describing ideal substrate and nanostructure characteristics for maximized enhancement and substrate-to-substrate consistency.

A second critical factor in substrate design is the understanding of the influence of chemical enhancement in SERS detection. This element of enhancement is largely overlooked as it is generally a target specific behavior. However, *this work has provided a precedent for incorporating specific design criteria, such as exposed crystal faces of the nanostructures and binding orientation manipulation, to impart the addition non-resonant chemical enhancement mechanism for further amplified Raman signal.* This enhancement factor can add to the overall enhancement mechanisms that are typically used to maximize SERS signal. Control or direction of the binding orientation of the target analyte in SERS detection systems is typically not a concern as most systems utilize non-specific binding. However, by using specific biorecognition elements, the target biomolecule can be specifically located within the plasmonic hot spot and still maintain a physiologically-relevant conformation. This fundamental study will add to the foundation of SERS sensor design criteria and provide insight into how researchers can manipulate the nanostructure system to maximize previously untapped mechanisms of chemical enhancement.

The novel three-dimensional design and fundamental understanding of SERS substrate has broad implications in the field. There is a clear application for this technology in the future of sensing if new substrates can be designed with the incorporation of the criteria described here related to improving the electromagnetic and chemical enhancement for higher sensitivity. There is potential for the development of more organized three-dimensional porous structures that may possess improved waveguiding or reflective properties that can use the principles of nanostructure design and alignment as well as pore size matching with the excitation source developed in this work to guide their design and fabrication. The next step in the future development of organized three-dimensional porous substrates could lie in the use of patterning technology to allow multiplexed detection of many analytes at the same time for rapid and thorough detection. The unique cylindrical through-pores of these substrates may also allow for their application in microfluidic and separation devices that can provide non-invasive point-of-care diagnostics for the medical field.

The controlled construction of gold nanoframe widened hot spots has provided a basis for future SERS sensors that can now have application for the detection of bulky biomolecules rather than small organic molecules. These aggregates also possess the extremely high level of specificity that is a result of the use of aptamers for biorecognition. This facile demonstration of aptamer ligands for label-free SERS detection of a biological target could serve as a foundation for future substrate designs that incorporate such highly specific functionality. Based on the two main tasks presented in this work, the next step is to combine the technologies to create a biologically functionalized porous alumina membrane SERS substrate with a high degree of selectivity as a result of the targeting ligand used for detection as well as the controlled hot spot formation that is dictated by electrostatic coupling of oppositely-charge surface chemistries. Through the use of the design criteria for maximizing enhancement in three-dimensional substrates and the predicate biological sensors utilizing widened hot spots and micropatterning described in this work, next generation SERS substrate design will be able to tailor their plasmonic behavior and selective chemistries to the target of choice to provide a reliable, multiplexed, and highly enhanced Raman measurement for label-free detection.

The deeper understanding of the fundamental enhancement mechanisms with a specific focus on novel three-dimensional designs combined with the intentional formation of complex widened hot spots and patterned substrates with unique nanostructure shapes will make a significant impact on the progress of the field of SERS sensing. Substrates utilizing the specific design criteria developed in this work could make a large impact in the fields of point-of-care biological diagnostics, in-the-field chemical sensing and identification, and continuous, real-time environmental monitoring.

ACKNOWLEDGEMENTS

Financial support from the NSF-CBET - 0930781 and from the U.S. Department of Energy, Office of Basic Energy Sciences, Division of Materials Sciences and Engineering under Award # DE-FG02-09ER46604 is gratefully acknowledged. Special thanks is given for the fellowship support under and awarded by the Air Force Office of Scientific Research, National Defense Science and Engineering Graduate (NDSEG) Fellowship, 32 CFR 168a.

DISSEMINATION OF WORK

This work has been conveyed to the scientific community by the following publications and presentations.

Publications

1. **Combs, Z. A.**; Malak, S. T.; König, T.; Mahmoud, M. A.; Chávez, J. L.; Kelley-Loughnane, N.; El-Sayed, M. A.; Tsukruk, V. V. Aptamer-Assisted Formation of Gold Nanoframe Dimers, *Particle* **2013**, DOI: 10.1002/ppsc.201300187.

2. König, T.; Kodiyath, R.; **Combs, Z. A**.; Mahmoud, M. A.; El-Sayed, M. A.; Tsukruk, V. V. Plasmonic Coupling Effect of Silver Nanocube Aggregates in Cylindrical Alumina Pores for Higher Refractive Index Sensing, *Particle* **2013**, DOI: 10.1002/ppsc.201300217.

3. Kodiyath, R.; Malak, S. T.; **Combs, Z. A.**; König, T.; Mahmoud, M. A.; El-Sayed, M. A.; Tsukruk, V. V. Assemblies of Silver Nanocube for Highly Sensitive SERS Chemical Vapor Detection, *Journal of Materials Chemistry A* **2013**, *1*, 2777-2788.

4. Kodiyath, R.; Papadopoulos, T. A.; Wang, J.; **Combs, Z. A.**; Li, H.; Brown, R. J. C., Bredas, J.-L., Tsukruk, V. V. Silver-Decorated Cylindrical Nanopores: Combining the Third Dimension with Chemical Enhancement for Efficient Trace Chemical Detection with SERS, *Journal of Physical Chemistry C* **2012**, *116*, 13917-13927.

5. **Combs, Z. A.**; Chang, S.; Clark, T.; Singamaneni, S.; Anderson, K. D.; Tsukruk, V. V. Label-Free Raman Mapping of Surface Distribution of Protein A and IgG Biomolecules, *Langmuir* **2011**, *27*, 3198-3205.

6. Kodiyath, R.; Wang, J.; **Combs, Z. A.**; Chang, S. Gupta, M. K.; Anderson, K. D.; Brown, R. J. C.; Tsukruk, V. V. SERS Effects in Silver-Decorated Cylindrical Nanopores, *Small* **2011**, *7*, 3452-3457.

The following publications are related to the work in this dissertation:

7. Lisunova, M.; Mahmoud, M. A.; Holland, N.; **Combs, Z. A.**; El-Sayed, M. A.; Tsukruk, V. V. The Unusual Fluorescence Intensity Enhancement of Poly(p-phenyleneethynylene) Polymer Separated from the Plasmonic Silver Nanocube Surface by H-bonded LbL Shells, *Journal of Materials Chemistry* **2012**, *22*, 16745-16753.

8. Chang, S.; **Combs, Z. A.**; Gupta, M. K.; Davis, R.; Tsukruk, V. V. In situ Growth of Silver Nanoparticles in Porous Membranes for Surface-Enhanced Raman Scattering, *ACS Applied Materials and Interfaces* **2010**, *2*, 3333-3339.

Presentations

- **Combs, Z. A.**; Malak, S. T.; Tsukruk, V. V. Aptamer-Assisted Formation of Gold Nanoframe Dimers, ***MSE Research Symposium 2013***, Atlanta, GA.

- **Combs, Z. A.**; Kodiyath, R.; Malak. S. T.; Tsukruk, V. V. Design of Biological-Metallic Interfaces for Seletive Biomarker Trapping and Sensing, ***GTRI Graduate Research Symposium 2013***, Atlanta, GA.

- **Combs, Z. A.**; Tsukruk, V. V. Surface Engineered Molecular Assemblies, ***MSE Research Symposium 2012***, Atlanta, GA.

- Lisunova, M.; Mahmoud, M. A.; Holland, N.; **Combs, Z. A.**; El-Sayed, M. A.; Tsukruk, V. V. The Unusual Fluorescence Intensity Enhancement of Poly(p-phenyleneethynylene) Polymer Separated from the Plasmonic Silver Nanocube Surface by H-bonded LbL Shells, ***MRS Fall Meeting 2012***, Boston, MA.

- Kodiyath, R.; Papadopoulos, T. A.; Wang, J.; **Combs, Z. A.**; Li, H.; Brown, R. J. C., Bredas, J.-L., Tsukruk, V. V. Silver-Decorated Cylindrical Nanopores: Combining the Third Dimension with Chemical Enhancement for Efficient Trace Chemical Detection with SERS, ***MRS Fall Meeting 2012***, Boston, MA.

- **Combs, Z. A.**; Kodiyath, R.; Malak, S. T.; Tsukruk, V. V. Design of Biological-Metallic Interfaces for Seletive Biomarker Trapping and Sensing, ***Gordon Research Conference – Biointerface Science 2012***, Les Diablerets, Switzerland.

- Combs, Z. A.; Kodiyath, R.; **Tsukruk, V. V.** Label-free Raman mapping of surface distribution of protein A and IgG biomolecules and selected biomarkers, ***4th International Conference on Drug Discover and Therapy 2012***, Dubai, United Arab Emirates.

- **Combs, Z. A.**; Chang, S; Anderson, K. D.; Davis, R.; Tsukruk, V. V. Raman mapping of Surface Distribution and Trace Detection of Common Biomolecules and Stress-Related Biomarkers, ***MRS Fall Meeting 2011***, Boston, MA.

- **Combs, Z. A.**; Kodiyath, R.; Chang, S.; Gupta, M. K.; Davis, R.; Tsukruk V. V. Pores Size Dependence of 3D Anodic Alumina SERS Substrates, ***MRS Fall Meeting 2011***, Boston, MA.

- **Combs, Z. A.**; Chang, S.; Tsukruk, V. V. 3D Porous Substrates for Label-Free SERS Detection of Chemical and Biological Analytes, ***DARPA/FDA Expanding In Vivo Biomarker Detection Devices Workshop 2011***, Washington, D.C.

- **Combs, Z. A.**; Chang, S.; Singamaneni, S.; Ko, H.; Tsukruk, V. V. Nanoporous Substrate with Mixed Nanoclusters for Surface-enhanced Raman Scattering, ***Nanotechnology for Defense Conference 2010***, Atlanta, GA.

REFERENCES

(1) Siqueira, J. R.; Caseli, L.; Crespilho, F. N.; Zucolotto, V.; Oliveira, O. N. *Biosensors and Bioelectronics* **2009**, *25*, 1254-1263.

(2) Kaliyaperumal, A.; Jing, S. *Curr. Pharm. Biotechno.* **2009**, *10*, 352-358.

(3) Tripp, R. A.; Dluhy, R. A.; Zhao, Y. *Nanotoday* **2008**, *3*, 31-37.

(4) Le Ru, E. C.; Etchegoin, P. G. *Principles of Surface-Enhanced Raman Spectroscopy and Related Plasmonic Effects,* Elsevier: New York, **2009**.

(5) Sperling, L. H. *Introduction to Physical Polymer Science*, John Wiley & Sons, Inc., New York, **2001**.

(6) Wüthrich, K. *NMR Studies of Structure and Function of Biological Macromolecules*, Nobel Lecture, December 8, **2002**.

(7) Wüthrich, K. *Nature Structural Biology* **2001**, *8*, 923-925.

(8) Koenig, J. L. *Spectroscopy of Polymers*, 2nd ed., Elsevier, Amsterdam, **1999**.

(9) Baker, M. *Nature Methods* **2010**, *7*, 157-161.

(10) Jackson, M.; Mantsch, H. H. *Critical Reviews in Biochemistry Molecular Biology* **1995**, *30*, 95-120.

(11) Movasaghi, Z.; Rehman, S.; ur Rehman, I. *Applied Spectroscopic Reviews* **2008**, *43*, 134-179.

(12) Liu, J.; Lu. Y. *Journal of Fluorescence* **2004**, *14*, 343-354.

(13) Chávez, J. L.; Lyon, W.; Kelley-Loughnane, N.; Stone, M. O. *Biosensors and Bioelectronics* **2010**, *26*, 23-28.

(14) Miao, P.; Liu, T.; Li, X.; Ning, L.; Yin, J.; Han, K. *Biosensors and Bioelectronics* **2013**, 20-24.

(15) Chávez, J. L.; MacCuspie, R. I.; Stone, M. O.; Kelley-Loughnane, N. *J. Nanopart. Res.* **2012**, *14*, 1166.

(16) Jia, M.; Belyavskaya, E.; Deuster, P.; Sternberg, E. M. *Anal. Chem.* **2012**, *84*, 6508-6514.

(17) Xiang, X.; Luo, M.; Shi, L.; Ji, X.; He, Z. *Analytica Chimica Acta* **2012**, *751*, 155-160.

(18) Spiro, T. G. *Biological applications of Raman Spectroscopy*, John Wiley & Sons: New York, **1987**.

(19) McCreery, R. L. *Raman Spectroscopy for Chemical Analysis*; John Wiley & Sons: New York, V. 157, **2000**.

(20) Nie, S.; Emory, S. R. *Science* **1997**, *275*, 1102-1106.

(21) Fleischmann, M.; Hendra, P. J.; McQuillan, A. J. *Chem. Phys. Lett.* **1974**, *26*, 163-166.

(22) Kneipp, K.; Wang, Y.; Kneipp, H.; Perelman, L. V.; Itzkan, I.; Dasari, R. R.; Feld, M. S. *Phys. Rev. Lett.* **1997**, *78*, 1667-1670.

(23) Stewart, M. E.; Anderton, C. R.; Thompson, L. B.; Maria, J.; Gray, S. K.; Rogers, J. A.; Nuzzo, R. G.; *Chem. Rev.* **2008**, *108*, 494-521.

(24) Xu, H.; Aizpurua, J.; Kall, M.; Apell, P. *Phys. Rev. E.* **2000**, *62*, 4318-4324.

(25) Xu, H.; Kall, M. *ChemPhysChem.* **2003**, *4*, 1001-1005.

(26) Campion, A.; Kambhampati, P. *Chem. Soc. Rev.* **1998**, 27, 241-250.

(27) Moskovits, M.; DiLella, D. P.; Maynard, K. *Langmuir* **1988**, *4*, 67-76.

(28) Su, K. H.; Wei, Q.-H.; Zhang, X.; Mock, J. J.; Smith, D. R.; Schultz, S. *Nano Lett.* **2003**, *3*, 1087-1090.

(29) Gunnarsson, L.; Rindzevicius, T.; Prikulis, J.; Kasemo, B.; Käll, M.; Zou, S.; Schatz, G. C. *J. Phys. Chem. B* **2005**, *109*, 1079-1087.

(30) Jain, P. K.; Huang, W.; El-Sayed, M. A. *Nano Lett.* **2007**, *7*, 2080-2088.

(31) Maier, S. A.; Brongersma, M. L.; Kik, P. G.; Atwater, H. A. *Phys. Rev. B* **2002**, *65*, 193408-193408-4.

(32) Huang, W.; Qian, W.; Jain, P. K.; El-Sayed, M. A. *Nano Lett.* **2007**, *7*, 3227-3234.

(33) Sundaramurthy, A.; Crozier, K. B.; Kino, G. S.; Fromm, D. P.; Schuck, P. J.; Moerner, W. E. *Phys. Rev. B* **2005**, *72*, 165409-165409-6.

(34) Sweatlock, L. A.; Maier, S. A.; Atwater, H. A.; Penninkhof, J. J.; Polman, A. *Phys. Rev. B* **2005**, *71*, 235408-235408-7.

(35) Fang, Y.; Seong, N. H.; Dlott, D. D. *Science* **2008**, *321*, 388-392.

(36) Haynes,C. L.; Van Duyne,R. P. *J. Phys. Chem. B* **2003**, *107*, 7426-7433.

(37) Campion, A.; Ivanecky, J. E., III; Child, C. M.; Foster, M. C. *J. Am. Chem. Soc.* **1995**, *117*, 11807-11808.

(38) Nikoobakht, B.; Wang, J.; El-Sayed, M. A. *Chem. Phys. Lett.* **2002**, *366*, 17-23.

(39) Fromm, D. P.; Sundaramurthy, A.; Kinkhabwala, A.; Schuck, P. J.; Kino, G. S.; Moerne, W. E. *J. Chem. Phys.* **2006**, *124*, 061101-061101-4.

(40) Zhao, L. L.; Jensen, L.; Schatz, G. C. *Nano Lett.* **2006**, *6*, 1229-1234.

(41) Morton, S. M.; Silverstein, D. W.; Jensen, L. *Chem. Rev.* **2011**, *111*, 3962-3994.

(42) Otto, A.; Futamata, M. *Electronic Mechanisms of SERS*; Kneipp, K.; Moskovits, M.; Kneipp, H., Eds.; Springer-Verlag: Berlin, Heidelberg, Germany, **2006**; Vol. 103, Chapter 8, 147-184.

(43) Jensen, L.; Schatz, G. C. *J. Phys. Chem. A* **2006**, *110*, 5973-5977

(44) Jensen, L.; Aikens, C. M.; Schatz, G. C. *Chem. Soc. Rev.* **2008**, *37*, 1061-1073.

(45) Engvall, E.; Perlman, P. *Immunochemistry* **1971**, *8*, 871-874.

(46) Voller, A.; Bartlett, A.; Bidwell, D. E. *J. Clin. Pathol.* **1978**, *31*, 507-520.

(47) MacBeath, G. *Nature Genetics* **2002**, *32*, 526-532.

(48) Karp, G. *Cell and Molecular Biology Concepts and Experiments*, John, Wiley & Sons, Inc. USA, **2005**, Chapter 18, 755-756.

(49) Dorfman, K. D.; King, S. B.; Olson, D. W.; Thomas, J. D. P.; Tree, D. R. *Chem. Rev.* **2013**, *113*, 2584-2667.
(50) Nylander, C.; Liedberg, B.; Lind, T. *Sensors and Actuators* **1982**, *3*, 79-88.
(51) Liedberg, B.; Nylander, C.; Lundström, I. *Sensors and Actuators* **1983**, *4*, 299-304.
(52) Homola, J.; Yee, S. S.; Gauglitz, G. *Sensors and Actuators B* **1999**, *54*, 3-15.
(53) Homola, J. *Anal. Bioanal. Chem.* **2003**, *377*, 528-539.
(54) Hoa, X. D.; Kirk, A. G.; Tabrizian, M. *Biosensors and Bioelectronics* **2007**, *23*, 151-160.
(55) Chen, G.; Song, F.; Xiong, X.; Peng, X. *Ind. Eng. Chem. Res.* **2013**, *52*, 11228-11245.
(56) Yuan, L.; Lin, W.; Zheng, K.; Zhu, S. *Acc. Chem. Res.* **2013**, *46*, 1462-1473.
(57) Guerrini, L.; Graham, D. *Chem. Soc. Rev.* **2012**, *41*, 7085-7107.
(58) Alvarez-Puebla, R. A.; Liz-Marzán, L. M. *Small* **2010**, *6*, 604-610.
(59) Jones, M. R.; Osberg, K. D.; Macfarlane, R. J.; Langille, M. R.; Mirkin, C. A. *Chem. Rev.*, **2011**, *111*, 3736-3827.
(60) Ko, H.; Tsukruk, V. V. *Small* **2008**, *4*, 1980-1984.
(61) Larmour, I. A.; Graham, D. *Analyst* **2011**, *136*, 3831-3853.
(62) Dougan, J. A.; Faulds, K. *Analyst* **2012**, *137*, 545-554.
(63) Combs, Z. A.; Chang, S.; Clark, T.; Singamaneni, S.; Anderson, K. D.; Tsukruk, V. V. *Langmuir* **2011**, *6*, 3198-3205.
(64) Chang, S.; Ko, H.; Singamaneni, S.; Gunawidjaja, R.; Tsukruk, V. V. *Anal. Chem.* **2009**, *81*, 5740-5748.
(65) Kodiyath, R.; Malak, S. T.; Combs, Z. A.; König, T.; Mahmoud, M. A.; El-Sayed, M. A.; Tsukruk, V. V. *J. Mater. Chem. A*, **2013**, *1*, 2777-2788.
(66) Hu, X.; Meng, G.; Huang, Q.; Xu, W.; Han, F.; Sun, K.; Xu, Q.; Wang, Z. *Nanotechnology* **2012**, *23*, 385705.
(67) Chang, S.; Combs, Z. A.; Gupta, M. K.; Davis, R.; Tsukruk, V. V. *ACS Appl. Mater. Interfaces* **2010**, *2*, 3333-3339.
(68) Ko, H.; Chang, S.; Tsukruk, V. V. *ACS Nano* **2009**, *3*, 181-188.
(69) Kodiyath, R.; Papadopoulos, T. A.; Wang, J.; Combs, Z. A.; Li, H.; Brown, R. J. C.; J.-L. Brédas, Tsukruk, V. V. *J. Phys. Chem. C* **2012**, *116*, 13917-13927.
(70) Gao, B.; Arya, G.; Tao, A. R. *Nature Nanotechnology* **2012**, *7*, 433-437.
(71) Gunawidjaja, R.; Peleshanko, S.; Ko, H.; Tsukruk, V. V. *Adv. Mater.* **2008**, *20*, 1544-1549.
(72) Rosi, N. L.; Mirkin, C. A. *Chem. Rev.* **2005**, *105*, 1547-1562.
(73) Wang, G.; Wang, Y.; Chen, L.; Choo, J. *Biosensors and Bioelectronics* **2010**, *25*, 1859-1868.
(74) Mieszawska, A. J.; Mulder, W. J. M.; Fayad, Z. A.; Cormode, D. P. *Mol. Pharmaceutics* **2013**, *10*, 831-846.
(75) Xia, Y.; Li, W.; Cobley, C. M.; Chen, J.; Xia, X.; Zhang, Q.; Yang, M.; Cho, E. C.; Brown, P. K. *Acc. Chem. Res.* **2011**, *44*, 914-924.

(76) Murphy, C. J.; Gole, A. M.; Stone, J. W.; Sisco, P. N.; Alkilany, A. M.; Goldsmith, E. C.; Baxter, S. C. *Acc. Chem. Res.* **2008**, *41*, 1721-1730.
(77) Wiley, B. J.; Wang, Z.; Wei, J.; Yin, Y.; Cobden, D. H.; Xia, Y. *Nano Lett.* **2006**, *6*, 2273-2278.
(78) Shen, L.; Ji, J.; Shen, J. *Langmuir* **2008**, *24*, 9962-9965.
(79) Rogach, A. L.; Shevchenko, G. P.; Afanaseva, Z. M.; Sviridov, V. V. *J. Phys. Chem. B* **1997**, *101*, 8129-8132.
(80) Kumar, A.; Vemula, P. K.; Ajayan, P. M.; John, G. *Nat. Mater.* **2008**, *7*, 236-241.
(81) Batarseh, I. K.; *J. Antimicrob. Chemother.* **2004**, *54*, 546-548.
(82) He, J.; Ichinose, I.; Kunitaki, T.; Nakao, A.l Shiraishi, Y.; Toshima, N. *J. Am. Chem. Soc.* **2003**, *125*, 11034-11040.
(83) Wu, Y.; Li, Y.; Ong, B. S. *J. Am. Chem. Soc.* **2007**, *129*, 1862-1863.
(84) Schrand, A. M.; Braydich-Stolle, L. K.; Schlager, J. J.; Dai, L.; Hussain, S. M. *Nanotechnology* **2008**, *19*, 235104.
(85) Peng, H.-I.; Strohsahl, C. M.; Leach, K. E.; Krauss, T. D.; Miller, B. L. *ACS Nano* **2009**, *3*, 2265-2273.
(86) Cañamares, M. V.; Garcia-Ramos, J. V.; Gómez-Varga, J. D. ; Domingo, C.; Sanchez-Cortes, S. *Langmuir* **2005**, *21*, 8546.
(87) Chou, K. S.; Ren, C. Y. *Mater. Chem. Phys.* **2000**, *64*, 241.
(88) Velikov, K. P.; Zegers, G. E.; van Blaaderen, A. *Langmuir* **2003**, *19*, 1384.
(89) Xia, Y.; Xiong, Y.; Lim. B.; Skrabalak, S. E. *Angew. Chem. Int. Ed.* **2009**, *48*, 60-103.
(90) Wiley, B. J.; Herricks, T.; Sun, Y.; Xia, Y. *Nano Lett.* **2004**, *4*, 1733-1739.
(91) Jin, R.; Cao, Y. C.; Hao, E.; Métraux, G. S.; Schatz, G. C.; Mirkin, C. A. *Nature*, **2003**, *425*, 487-490.
(92) Sun, Y.; Xia, Y. *Science* **2002**, *298*, 2176-2179.
(93) Wiley, B. J.; Xiong, Y.; Li, Z.-Y.; Yin, Y.; Xia, Y. *Nano Lett.* **2006**, *6*, 765-768.
(94) Wiley, B. J.; Chen, Y.; McLellan, J. M.; Xiong, Y.; Li, Z.-Y.; Ginger, D.; Xia, Y. *Nano Lett.* **2007**, *7*, 1032-1036.
(95) Gao, Y.; Jiang, P.; Song, L.; Wang, J. X.; Liu, L. F.; Liu, D. F.; Xiang, Y. J.; Zhang, Z. X.; Zhao, X. W.; Dou, X. Y.; Luo, S. D.; Zhou, W. Y.; Xie, S. S. *J. Cryst. Growth* **2006**, *289*, 376-380.
(96) Hu, J.-Q.; Chen, Q.; Xie, Z.-X.; Han, G.-B.; Wang, R.-H.; Ren, B.; Zhang, Y.; Yang, Z.-L.; Tian, Z.-Q. *Adv. Funct. Mater.* **2004**, *14*, 183-189.
(97) Pustovit, V. N.; Shahbazyan, T. V. *J. Opt. Soc. Am. A* **2006**, *23*, 1369-1374.
(98) Mahmoud, M. A.; Tabor, C. E.; El-Sayed, M. A. *J. Phys. Chem. C* **2009**, *113*, 5493-5501.
(99) Dreaden, E. C.; Alkilany, A. M.; Huang, X.; Murphy, C. J.; El-Sayed, M. A. *Chem. Soc. Rev.* **2012**, *41*, 2740-2779.
(100) Chen, M. S.; Goodman, D. W. *Science* **2004**, *306*, 252-255.
(101) Green, I. X.; Tang, W.; Neurock, M.; Yates, J. T. *Science* **2011**, *333*, 736-739.
(102) Shaw, C. F. *Chem. Rev.* **1999**, *99*, 2589-2600.

(103) Dreaden, E. C.; Mackey, M. A.; Huang, X.; Kang, B.; El-Sayed, M. A. *Chem. Soc. Rev.* **2011**, *40*, 3391-3404.

(104) Jain, P. K.; Huang, X.; El-Sayed, I. H.; El-Sayed, M. A. *Acc. Chem. Res.* **2008**, *41*, 1578-1586.

(105) Eustis, S.; El-Sayed, M. A. *Chem. Soc. Rev.* **2006**, *35*, 209-217.

(106) Lohse, S. E.; Murphy, C. J. *Chem. Mater.* **2013**, *25*, 1250-1261.

(107) Faraday, M. *Philos. Trans. R. Soc. London* **1857**, *147*, 145-181.

(108) Turkevich, J.; Stevenson, P. C.; Hiller, J. *Discuss. Faraday Soc.* **1951**, *11*, 55-75.

(109) Jana, N. R.; Gearheart, L.; Murphy, C. J. *Langmuir*, **2001**, *17*, 6782-6786.

(110) El-Sayed, I. H.; Huang, X.; El-Sayed, M. A. *Nano Lett.* **2005**, *5*, 829-834.

(111) Alivisatos, A. P. *Nat. Biotechnol.* **2004**, *22*, 47-52.

(112) Prasad, P. N. *Nanophotonics*, John Wiley & Sons, Inc., **2004**.

(113) Jana, N. R.; Gearheart, L.; Murphy, C. J. *Adv. Mater.* **2001**, *13*, 1389.

(114) Chen, J.; McLellan, J. M.; Siekkinen, A.; Xiong, Y.; Xia, Y. *J. Am. Chem. Soc.***2006**, *128*, 14776-14777.

(115) Kim, F.; Connor, S.; Song, H.; Kuykendall, T.; Yang, P. *Angew. Chem., Int. Ed.* **2004**, *43*, 3673-3677.

(116) Tonucci, R. J.; Justus, B. L.; Campillo, A. J.; Ford, C. E. *Science* **1992**, *258*, 783.

(117) Whitney, T. W.; Jiang, J. S.; Searson, P. C.; Chien, C. L. *Science* **1993**, *261*, 1361.

(118) Masuda, H.; Fukuda, K. *Science* **1995**, *268*, 1466.

(119) Li, A. P.; Müller, F.; Birner, A.; Nielsch, K.; Gösele U. *J. Appl. Phys.* **1998**, *84*, 6023.

(120) Sharma, B.; Fernanda Cardinal, M.; Kleinman, S. L.; Greeneltch, N. G.; Frontiera, R. R.; Blaber, M. G.; Schatz, G. C.; Van Duyne, R. P. *MRS Bulletin* **2013**, *38*, 615-624.

(121) Campbell, N. A.; Reece, J. B.; Mitchell, L. G. *Biology*; Fifth Edition, Benjamin/Cummings: New York, **1999**, 907-908.

(122) Lee, N.-S.; Hsieh, Y.-Z.; Paisley, R. F.; Morris, M. D. *Anal. Chem.* **1988**, *60*, 442-446.

(123) Volkan, M; Stokes, D. L.; Vo-Dinh, T. *Appl. Spectrosc.* **2000**, *54*, 1842-1848.

(124) Monks, S. A., Karagianis, G., Howlett, G. J., Norton, R. S. *J. Biomol. NMR* **1996**, *8*, 379-390.

(125) Kim, H. Y.; Hong, E.; Kim, J. I.; Lee, W. *J. Biochem. Mol. Biol.* **2004**, *37*, 565-573.

(126) Veerapandian, B.; Gilliland, G. L.; Raag, R.; Svensson, A. L.; Masui, Y.; Hirai, Y.; Poulos, T. L. *Proteins* **1992**, *12*, 10-23.

(127) Deadwyler, S. A.; Porrino, L.; Siegel, J. M.; Hampson, R. E. *The Journal of Neuroscience* **2007**, *27*, 14239-14247.

(128) Erickson, J. C.; Clegg, K. E.; Palmiter, R. D. *Nature* **1996**, *381*, 415-418.

(129) Clark, B. D.; Collins, K. L; Gandy, M. S.; Webb, A. C.; Auron, P. E. *Nucleic Acids Research* **1986**, *14*, 7897-7914.
(130) Alberts, B.; Johnson, A.; Lewis, J.; Raff, M.; Roberts, K.; Walter, P. *Molecular Biology of the Cell, 4th ed.*, Garland Science, New York, **2003**, 1376.
(131) Kim, N. H.; Lee, S. J; Moskovits, M. *Adv. Mater.* **2011**, *23*, 4152-4156.
(132) Neumann, O.; Zhang, D.; Tam, F; Lal, S.; Stafshede, P. W.; Halas, N. J. *Anal. Chem.* **2009,** *81*, 10002-10006.
(133) Kim, N. H.; Lee, S. J.; Moskovits, M. *NanoLett.* **2010,** *10*, 4181-4185.
(134) Ravindranath, S. P.; Wang, Y.; Irudayaraj, J. *Sensors and Actuators B: Chemical* **2011,** *152*, 183-190.
(135) Huh, Y. S.; Erickson, D. *Biosensors and Bioelectronics* **2010**, *25*, 1240-1243.
(136) Li, M.; Zhang, J.; Suri, S.; Sooter, L. J.; Ma, D.; Wu, N. *Anal. Chem.* **2012,** *84*, 2837-2842.
(137) Pagba, C. V.; Lane, S. M.; Wachsmann-Hogiu, S. *J. Raman Spectrosc.* **2010,** *41*, 241-247.
(138) Tomizaki, K.; Usui, K.; Mihara, H. *ChemBioChem* **2005**, *6*, 782-799.
(139) Joungmok, K.; Park, H-Y.; Choi, K-J.; Jung, H.; Han, S-H.; Lee, J-S.; Park, J-S.; Yoon, M-Y. *J. Microbiol. Biotechnol.* **2006,** *16 (11)*, 1784–1790.
(140) Nakanishi, K.; Sakiyama, T.; Imamura, K. *Journal of Bioscience and Bioengineering* **2001,** *91* (3), 233-244.
(141) Saerens, D.; Huang, L.; Bonroy, K.; Muyldermans, S. *Sensors* **2008,** *8*, 4669-4686.
(142) Manníroni, C.; Di Nardo, A.; Fruscoloni, P.; Tocchini-Valentini, G. P. *Biochemistry* **1997**, *36*, 9726-9734.
(143) Lauhon, C.; Szostak, J. *J. Am. Chem. Soc.* **1995**, *117*, 1246-1257.
(144) Zuker, M. *Nucleic Acids Res.* **2003**, *31*, 3406-3415.
(145) Walsh, R; DeRosa, M. C. *Biochemical and Biophysical Research Communications* **2009**, *388*, 732-735.
(146) Mendosa, S. D.; Bowser, M. T. *J. Am. Chem. Soc.* **2005**, *127*, 9382-9383.
(147) Camden, J. P.; Dieringer, J. A.; Wang, Y.; Masiello, D. J.; Marks, L. D.; Schatz, G. C.; Van Duyne, R. P. *J. Am. Chem. Soc*. **2008**, *130*, 12616.
(148) Kneipp, K.; Kneipp, H.; Deinum, G.; Itzkan, I.; Dasari, R. R.; Feld, M. S. *Appl. Spectrosc.* **1998**, *52*, 175.
(149) Kleinman, S. L.; Ringe, E.; Valley, N.; Wustholz, K. L.; Phillips, E.; Scheidt, K. A.; Schatz, G. C.; Van Duyne, R. P. *J. Am. Chem. Soc.* **2011**, *133*, 4115.
(150) Kneipp, K.; Moskovits, M.; Kneipp, H.(Eds) *Surface-Enhanced Raman Scattering Physics and Application.* Springer: New York, **2006**.
(151) Schlucker, S. *Surface Enhanced Raman Spectroscopy: Analytical, Biophysical and Life Science Applications.* Wiley-VCH: GmbH, **2011**.
(152) Baker, G. A.; Moore, D. S. *Anal. Bioanal. Chem*. **2005**, *382*, 1751.
(153) Lee, S. J.; Moskovits, M. *Nano Lett.* **2011**, *11*, 145.

(154) Kneipp, K.; Kneipp, H.; Itzkan, I.; Dasari, R. R.; Feld, M. S. *Chem. Rev*. **1999**, *99*, 2957.

(155) Jiang, C.; Lio, W. Y.; Tsukruk, V. V. *Phys. Rev. Lett.* **2005,** *95*, 115503.

(156) Kharlampieva, E.; Tsukruk, T.; Slocik, J. M.; Ko, H.; Poulsen, N.; Naik, R. R.; Kröger, N.; Tsukruk, V. V. *Adv. Mater.* **2008,** *20*, 3279.

(157) Singamaneni, S.; Kharlampieva, E.; Jang, J.-H.; McConney, M. E.; Jiang, H.; Bunning, T. J.; Thomas, E. L.; Tsukruk, V. V. *Adv. Mater*. **2010,** *22*, 1369.

(158) Thaxton, C. S.; Elghanian R.; Thomas, A. D.; Stoeva, S. I.; Lee, J. S.; Smith, N. D.; Schaeffer, A. J.; Klocker, H.; Horninger, W.; Bartsch, G.; Mirkin, C.A. *Proc. Natl. Acad. Sci. USA.* **2009**, *106*, *44*, 18437.

(159) Freeman, R. G.; Grabar, K. C.; Allison, K. J.; Bright, R. M.; Davis, J. A.; Guthrie, A. P.; Hommer, M. B.; Jackson, M. A.; Smith, P. C.; Walter, D. G.; Natan, M. J. *Science* **1995**, *267*, 1629.

(160) Wang, Z.; Pan, S.; Krauss, T. D.; Du, H.; Rothberg, L. J. *Proc. Natl. Acad. Sci. USA* **2003**, *100*, 8638.

(161) Lee, C. H.; Tian, L.; Singamaneni, S. *ACS Appl. Mater. Interfaces* **2010**, *2*, 3429.

(162) Chang, S.; Ko, H.; Gunawidjaja, R.; Tsukruk, V. V. *J. Phys. Chem. C* **2011,** *115*, 4387.

(163) Banholzer, M. J.; Millstone, J. E.; Qin, L. D.; Mirkin, C. A. C*hem. Soc. Rev.* **2008**, *37*, 885.

(164) Hulteen, J. C.; Treichel, D. A.; Smith, M. T.; Duval, M. L.; Jensen, T. R.; Van Duyne, R. P. *J. Phys. Chem. B* **1999**, *103*, 3854.

(165) Qin, L.; Zhou, S.; Xue, C.; Atkinson, A.; Schatz, G. C.; Mirkin, C. A. *Proc. Natl. Acad. Sci. USA* **2006**, *103*, 13300.

(166) Gobin, A. M.; Lee, M. H.; Halas, N. J.; James, W. D.; Drezek, R. A.; West, J. L. *Nano Lett.* **2007**, *7*, 1929.

(167) Gupta, M. K.; Chang, S.; Singamaneni, S.; Drummy, L. F.; Gunawidjaja, R.; Naik, R. R.; Tsukruk, V. V. *Small* **2011**, *7*, 1192.

(168) Chan, S.; Kwon, S.; Koo, T.; Lee, L.; Berlin, A. A. *Adv. Mater*. **2003**, *15*, 1595.

(169) Ko, H.; Singamaneni, S.; Tsukruk, V.V. *Small* **2008**, *4*, 1576-1599.

(170) Qian, L. H.; Ding, Y.; Fujita, T.; Chen, M. W. *Langmuir* **2008**, *24*, 4427.

(171) He, H.; Cai, W.; Lin, Y.; Chen, B. *Chem. Commun*. **2010**, *46*, 7223.

(172) Quinten, M.; Leitner, A.; Krenn, J. R.; Aussenegg, F. R. *Opt. Lett.* **1998**, *23*, 1331-1333.

(173) Maier, S. A.;Brongersma, M. L.; Kik, P. G.; Meltzer,S.; Requicha, A. A. G.; Atwater,H. A. *Adv. Mater.* **2001**, *13*, 1501-1505.

(174) Krenn, J. R.; Dereux, A.; Weeber, J. C.; Bourillot, E.; Lacroute, Y.; Goudonnet, J. P.; Schider, G.; Gotschy, W.; Leitner, A.; Aussenegg, F. R.; Girard, C. *Phys. Rev. Lett.* **1999**, *82*, 2590-2593.

---

(175) Maier, S. A.; Kik, P. G.; Atwater, H. A. *Appl. Phys. Lett.* **2002**, *81*, 1714-1716.

(176) Wei, Q.-H.; Su, K.-H.; Durant, S.; Zhang, X. *Nano Lett.* **2004**, *4*, 1067-1071.

(177) de Waele, R.; Koenderink, A. F.; Polman, A. *Nano Lett.* **2007**, 7, 2004-2008.

(178) Lee, S.J.; Morrill, A.R.; Moskovits, M. *J. Am. Chem. Soc.* **2006**, *128*, 2200-2201.

(179) Schierhorn, M.; Lee,S.J.; Boettcher, S.W.; Stucky, G.D.; Moskovits, M. *Adv. Mater.* **2006**, *18*, 2829-2832.

(180) Duan, G.; Cai, W.; Luo, Y.; Li, Y.; Lei, Y. *Appl. Phys. Lett.* **2006**, *89*, 181918-181918-3.

(181) Wang, H.-H.; Liu, C.-Y.; Wu, S.-B.; Liu, N.-W.; Peng, C.-Y.; Chan, T.-H.; Hsu, C.-F.; Wang, J.-K.; Wang, Y.-L. *Adv. Mater.* **2006**, *18*, 491-495.

(182) Saito, M.; Shibasaki, M.; Nakamura, S.; Miyagi, M. *Opt. Lett.* **1994**, *19*, 710-712.

(183) Lau, K. H. A.; Tan, S.; Tamada, K.; Sander, M. S.; Knoll, W. *J. Phys. Chem. B* **2004**, *108*, 10812-10818.

(184) Larsson, M.; Lindgren, J. *J. Raman Spectrosc.* **2005**, *36*, 394-399.

(185) Pavel, I.; McCarney, E.; Elkhaled, A.; Morrill, A. Plaxco, K.; Moskovits, M. *J. Phys. Chem. C* **2008**, *112*, 4880-4883.

(186) Cho, H.; Lee, B.; Liu, G. L.; Agarwal, A.; Lee, L. P. *Lab on Chip* **2009**, 9, 3360-3363.

(187) Weiss, S. *Science* **1999**, *283*, 1676-1683.

(188) Tombelli, S.; Minunni, M.; Luzi, F.; Mascini, M. *Bioelectrochemistry* **2005**, *67*, 135-141.

(189) Ruan, W.; Ji, W.; Xue, X.; Cui, Y.; Chen, L.; Zhou, T.; Niu, L.; Li, X.; Zhang, J.; Zhao, B. *J. Raman Spectrosc.* **2011**, *42*, 1492-1496.

(190) Lee, D.; Choe, Y.-J.; Lee, M.; Jeong, D. H.; Paik, S. R. *Langmuir* **2011**, *27*, 12782-12787.

(191) Papadopoulou, E.; Bell, S. E. J. *Chem. Commun.* **2011**, *47*, 10966-10968.

(192) Wang, H.-N.; Vo-Dinh, T. *Nanotechnology*. **2009**, *20*, 065101.

(193) Syed, M. A.; Pervaiz, S. *Oligonucleotides* **2010**. *20*, 215-224.

(194) Jeanmaire, D. L.; Van Duyne, R. P. *J. Electroanal. Chem.* **1977**, *84*, 1.

(195) Albrecht, M. G.; Creighton, J. A. *J. Am. Chem. Soc.* **1977**, *99*, 5215.

(196) Creighton, J. A.; Blatchford C. G.; Albrecht, M. G. *J. Chem. Soc., Faraday Trans. II* **1979**, *75*, 790.

(197) Lee, P. C.; Meisel, D. *J. Phys. Chem.* **1982**, *86*, 3391.

(198) Chen, S.-Y.; Mock, J. J.; Hill, R. T.; Chilkoti, A.; Smith, D. R.; Lazarides, A. A. *ACS Nano* **2010**, *4*, 6535-6546.

(199) Ciracì, C.; Hill. R. T.; Mock. J. J.; Urzhumov, Y.; Fernández-Domínguez, A. I.; Maier, S. A.; Pendry, J. P.; Chilkoti, A.; Smith, D. R. *Science* **2012**, *337*, 1072-1074.

(200) Kleinman, S. L.; Frontiera, R. R.; Henry, A.-I.; Dieringer, J. A.; Van Duyne, R. P. *Phys. Chem. Chem. Phys.* **2013**, *15*, 21-36.
(201) Yang, K.-H.; Liu, Y.-C.; Hsu, T.-C.; Juang, M.-Y. *J. Mater. Chem.* **2010**, *20*, 7530-7535.
(202) Greenletch, N. G.; Blaber, M. G.; Henry, A.-I.; Schatz, G. C.; Van Duyne, R. P. *Anal. Chem.* **2013**, *85*, 2297-2303.
(203) Alvarez-Puebla, R. A.; Liz-Marzán, L. M. *Chem. Soc. Rev.* **2012**, *41*, 43-51.
(204) Near, R.; Tabor, C.; Duan, J. S.; Pachter, R.; El-Sayed, M. A. *Nano Lett.* **2012**, *12*, 2158-2164.
(205) Banaee, M. G.; Crozier, K. B. *Optics Letters* **2010**, *35*, 760-762.
(206) Larmour, I. A.; Faulds, K.; Graham, D. *J. Phys. Chem. C*, **2010**, *114*, 13249-13254.
(207) Shenhar, R.; Norsten, T. B.; Rotello, V. M. *Adv. Mater.* **2005**, *17*, 657-669.
(208) Park, S. Y.; Lytton-Jean, A. K. R.; Lee, B.; Weigand, S.; Schatz, G. C.; Mirkin, C. A. *Nature*, **2008**, *451*, 553-556.
(209) Graham, D.; Thompson, D. G.; Smith, W. E.; Faulds, K. *Nat. Nanotechnol.* **2008**, *3*, 548-551.
(210) Tseng, A. A.; Chen, K.; Chen, C. D.; Ma, K. J. *IEEE Trans. Electron. Packag. Manuf.* **2003**, *26*, 141-149.
(211) Khoury, M.; Ferry, D. K. *J. Vac. Sci. Technol. B* **1996**, *14*, 75-79.
(212) Duan, H. G.; Fernandez-Dominguez, A. I.; Bosman, M.; Maier, S. A.; Yang, J. K. W. *Nano Lett.* **2012,** *12* (3), 1683-1689.
(213) Gopinath, A.; Boriskina, S. V.; Premasiri, W. R.; Ziegler, L.; Reinhard, B. M.; Dal Negro, L. *Nano Lett.* **2009,** 9, 3922-3929.
(214) McCord, M. A.; Rooks, M. J. *Handbook of Microlithography, Micromachining ,and Microfabrication*, Rai-Choudhury, P. Ed. Bellingham, WA: SPIE Optical Engineering, **1997,** ch. 2, pp. 139–249.
(215) Gomez-Medina, R.; Yamamoto, N.; Nakano, M.; Abajo, F. J. G. *New J. Phys.* **2008,** *10*.
(216) Kuttge, M.; de Abajo, F. J. G.; Polman, A. *Nano Lett.* **2010,** *10* (5), 1537-1541.
(217) Gibson, K. F.; Correia-Ledo, D.; Couture, M.; Graham, D.; Masson, J. F. *Chem. Commun.* **2011,** *47* (12), 3404-3406.
(218) Ahn, H. J.; Thiyagarajan, P.; Jia, L.; Kim, S. I.; Yoon, J. C.; Thomas, E. L.; Jang, J. H. *Nanoscale* **2013,** 5, 1836-1842.
(219) Yue, W. S.; Wang, Z. H.; Yang, Y.; Chen, L. Q.; Syed, A.; Wong, K.; Wang, X. B. *J. Micromech. Microeng.* **2012,** 22.
(220) Combs, Z. A.; Malak, S. T.; König, T.; Mahmoud, M. A.; Chávez, J. L.; El-Sayed, M. A.; Kelley-Loughnane, N.; Tsukruk, V. V. *Part. Part. Syst. Charact.* **2013**, DOI: 10.1002/ppsc.2013001.
(221) Tan, S. J.; Campolonga, M. J.; Luo, D.; Wenlong, C. *Nature Nanotechnology* **2011**, *6*, 268-276.
(222) Loweth, D. J.; Caldwell, W. B.; Peng, X.; Alivisatos, A. P.; Schultz, P. G. *Angew. Chem. Int. Ed.* **1999**, *38*, 1808-1812.

(223) Wei, Y.; Cao, C.; Jin, R. Mirkin, C. A. *Science* **2002**, *297*, 1536-1540.
(224) Lim, D.-K.; Jeon, K.-S.; Kim, H. M.; Nam, J.-M.; Suh, Y. D. *Nature Materials* **2010**, *9*, 60-67.
(225) Mulvaney, S. P.; Musick, M. D.; Keating, C. D.; Natan, M. J. *Langmuir* **2003**, *19*, 4784.
(226) Wustholz, K. L.; Henry, A.-I.; McMahon, J. M.; Freeman, R. G.; Valley, N.; Piotti, N. E.; Natan, M. J.; Schatz, G. C.; Van Duyne, R. P. *J. Am. Chem. Soc.* **2010**, *132*, 10903-10910.
(227) Gunawidjaja, R.; Kharlampieva, E.; Choi, I.; Tsukruk, V. V. *Small* **2009,** *5*, 2460-2466.
(228) Gandra, N.; Abbas, A.; Tian, L.; Singamaneni, S. *Nano Lett.* **2012**, *12*, 2645-2651.
(229) Abbas, A.; Brimer, A.; Slocik, J. M.; Tian, L.; Naik, R. R.; Singamaneni, S. *Anal. Chem.* **2013**, *85*, 3977-3983.
(230) Sato-Berrú, R.; Redón, R.; Vázquez-Olmos, A.; Saniger, J. M. *J. Raman Spectrosc.* **2009**, *40*, 376-380.
(231) Siekkinen, A. R.; McLellan, J. R.; Chen, J.; Xia, Y. *Chem. Phys. Lett.* **2006**, *432*, 491-496.
(232) Yen, C. W.; Mahmoud, M. A.; El-Sayed, M. A. *J. Phys. Chem. A* **2009**, *113*, 4340-4345.
(233) Chen, J.; Wiley, B.; Li, Z.-Y.; Campbell, D.; Saeki, F.; Cang, H.; Au, L.; Lee, J.; Li, X.; Xia, Y. *Adv. Mater.* **2005**, *17*, 2255-2261.
(234) Mahmoud, M. A.; El-Sayed, M. A. *J. Phys. Chem. C* **2008**, *112*, 14618-14625.
(235) Wu, H.-L.; Kuo, C.-H.; Huang, M. H. *Langmuir*, **2010**, *26*, 12307-12313.
(236) Li, A. P.; Müller, F.; Birner, A.; Nielsch, K.; Gösele, U. *Adv. Mater.* **1999,***11*, *483.*
(237) Liu, J.; Lu, Y. *Nature Protocols* **2006**, *1*, 246-252.
(238) Hurst, S. J.; Lytton-Jean, A. K. R.; Mirkin, C. A. *Anal. Chem.* **2006**, *78*, 8313-8318.
(239) www.veeco.com.
(240) Tsukruk, V. V. *Rubber Chem. Technol.***1997**, *70*, 430.
(241) McConney, M. E.; Singamaneni, S.; Tsukruk, V. V. *Polymer Review*s **2010,** *50*, 235-286.
(242) Kuptsov, A. H.; Zhizhin, G.N. *Handbook of Fourier Transform Raman and Infrared Spectra of Polymers;* Elsevier, 1998.
(243) Singamaneni, S.; Gupta, M. K.; Yang, R.; Tomczak, M.; Naik, R. R.; Wang, Z. L.; Tsukruk, V. V. *ACS Nano* **2009**, *3*, 2593.
(244) Anderson, K. D.; Slocik, J. M.; McConney, M. E.; Enlow, J. O.; Jakubiak, R.; Bunning, T. J.; Naik, R. R.; Tsukruk, V. V. S*mall* **2009**, *5*, 741-749.
(245) Tessier, P. M.; Velev, O. D.; Kalambur, A. T.; Lenhoff, A. M.; Rabolt, J. F.; Kaler, E. W. *Adv. Mater.*, **2001**, *13*, 396.
(246) Tessier, P. M.; Velev, O. D.; Kalambur, A. T.; Rabolt, J. F.; Lennhoff, A. M.; Kaler, E. M. *J. Am. Chem. Soc.*, **2000**, *122*, 9554.
(247) Xu, P.; Mack, N. H.; Jeon, S. H.; Doorn, S. K.; Han, X.; Wang, H. L. *Langmuir*, **2010**, *26*, 8882.

(248) Amezcua-Correra, A.; Yang, J.; Finlayson, C. E.; Peacock, A. C.; Hayes, J. R.; Sazio, P. J. A.; Baumberg, J. J.; Howdle, S. M. *Adv. Funct. Mater*., **2007**, *17*, 2024.

(249) Williamson, T. L.; Guo, X.; Zukoski, A.; Sood, A.; Diaz, D. J.; Bohn, P. W. *J. Phys. Chem. B,* **2005**,*109,* 20186.

(250) Brolo, A. G.; Arctander, E.; Gordon, R.; Leathem, B.; Kavanagh, K. L. *Nano. Lett.* **2004**, *4*, 2015.

(251) Luo, L. B. Chen, Li. M. Zhang, M. L. He, Z. B. Zhang, W. F. Yuan, G. D. Zhang, W. J. Lee, S. T. *J. Phys. Chem. C* **2009**, *113*, 9191.

(252) Kahl, M.; Voges, E.; Kostrewa, S.; Viets, C.; Hill, W.; *Sensor Actuat. A-Phys*. **1998**, *51*, 285.

(253) Fan, M.; Andrade, G. F. S.; Brolo, A. G. *Anal. Chim. Acta*, **2011**, *693*, 7.

(254) Du, Y.; Shi, L.; He, T.; Sun, X.; Mo, Y. *Applied Surface Science*, **2008**, *255*, 1901.

(255) Walsh, R. J.; Chumanov, G. *Appl. Spectrosc*. **2001**, *55,* 1695.

(256) Mondal, B.; Saha, S. K. *Chem. Phys. Lett*. **2010**, *497*, 89.

(257) Ji, N.; Ruan, W.; Wang, C.; Lu, Z.; Zhao, B. *Langmuir*, **2009**, *25*, 11869.

(258) Aggarwal, R. L.; Farrar, L. W.; Diebold, E. D.; Polla, L. *J. Raman Spectrosc*. **2009**, *40*, 1331.

(259) Zamuner, B. M.; Talaga, D.; Deiss, F.; Guieu, V.; Kuhn. A.; Ugo, P.; Sojic, N. *Adv. Funct. Mater.* **2009**, *19*, 3129.

(260) Sun, C. H.; Linn, N. C.; Jiang, P. *Chem. Mater*. **2007**, *19*, 4551.

(261) Johnson, P. B.; Christy, R. W. *Phys. Rev. B*, **1972**, *6*, 4370.

(262) http://www.comsol.com/products/multiphysics/

(263) Micic, M.; Klymyshyn, M.; Lu, H. P. *J. Phys. Chem. B*, **2004**, *108*, 2939.

(264) Kottmann, J. P.; Martin, O. J. F.; Smith, D. R.; Shultz, S. *Optics Express*, **2000**, *6*, 213.

(265) Jin, J. *The Finite Element Method in Electromagnetics*, John Wiley and Sons, New York, 2nd Edition., **2002**.

(266) Otto, A. *Top. Appl. Phy*., **1984**, *54,* 289.

(267) Garcia-Vidal, F. J.; Pendry, J. P. *Phys. Rev. Lett*., **1996**, *77*, 1163.

(268) Brown, R. J. C.; Wang, J.; Milton, M. J. T. *J. Nanomaterials*, **2007**, *Volume 2007*, Article ID 12086, 10 pages, doi:10.1155/2007/12086

(269)Evanoff Jr., D. D.; Chumanov, G. *Chem Phys Chem* **2005**, *6*, 1221.

(270) Whelan, C. M.; Smyth, M. R.; Barnes, C. J. *Langmuir* **1999**,*15,* 116.

(271) Whelan, C. M.; Barnes, C. J.; Walker, C. G. H.; Brown N. M. D. *Surface Science* **1999**, *425*, 195.

(272) Brown, R. J. C.; Wang, J.; Tantra, R.; Yardley, R. E.; Milton, M. J. T. *Faraday Discussions* **2006**, *132*, 201.

(273) Tian, Z.-Q.; Ren, B. *J. Phys. Chem. B* **2002**, *106*, 9463.

(274) Im, H.; Bantz, K. C.; Lindquist, N. C.; Hynes, C. L.; Oh, S. H. *Nano Lett*. **2010**, *10*, 2231.

(275) Wells, S. M.; Retterer, S. D.; Oran, J. M.; Sepaniak, M. J. *ACS Nano* **2009**, *3*, 3845.

(276) Saikin, S. K.; Amaya, R. O.; Rappoport, D.; Stopa, M.; Guzik, A. A. *Phys. Chem. Chem. Phys.* **2009**, *11*, 9401.

(277) Kodiyath, R.; Wang, J.; Combs, Z. A.; Chang, S.; Gupta, M. K.; Anderson, K. D.; Brown, R. J. C.; Tsukruk, V. V. *Small* **2011**, *7*, 3452-3457.

(278) Aizenberg, J.; Braun, P. V.; Wiltzius, P. *Phys. Rev. Lett.*, **2000**, *84*, 2997-3000.

(279) Bell, G. M.; Levine, S.; McCartney, L. N. *J. Colloid Interface Sci.*, **1970**, *33*, 335-359.

(280) Toghiani, R. K.; Toghiani, H.; Maloney, S. W.; Boddu, V. M. Prediction of Physicochemical Properties of Energetic Materials. *In Energetic Materials: Thermophysical Properties, Predictions, and Experimental Measurements.* Boddy, V.; Redner, P. Taylor and Francis Group, LLC., **2011;** p. 171-195.

(281) Fang, X.; Ahmad, S. R. *Appl Phys B.*, **2009**, *97*, 723-726.

(282) Lee, H.; You, S.; Pikhitsa, P. V.; Kim, J.; Kwon, S.; Woo, C. G.; Choi, M. *Nano Lett.* **2011**, *11*, 119.

(283) Han, Y.: Oo, M. K.; Zhu, Y., Sukhishvili, S.; Xiao, L.; Demohan, M. S.; Jinc, W.; Du, H. *Proc. SPIE* **2007**, 6767, 67670G.

(284) Yu, J.; Bai, X.; Suh, J.; Lee, S. B.; Son, S. J. *J. Am. Chem. Soc*. **2009**, *131*, 15574.

(285) Foss Jr, C. A.; Hornyak, G. L.; Stockert, J. A.; Martin, C. R. *J. Phys. Chem*. **1994**, *98*, 2963.

(286) The Cambridge Cluster Database, Wales, D. J.; Doye, J. P. K.; Dullweber, A.; Hodges, M. P.; Naumkin F. Y.; Calvo, F.; Hernández-Rojas J.; Middleton, T. F. URL http://www-wales.ch.cam.ac.uk/CCD.html

(287) Gaussian 09, Frisch, M. J.; Trucks, G. W.; Schlegel H. B. et al., Gaussian, Inc., Wallingford CT, 2009.

(288) Lee, W.; Scholz, R.; Nielsch, K.; Gosele, U. *Angew. Chem. Int. Ed*. **2005**, *44*, 6050.

(289) Zhang, J.; Li, X.; Sun, X.; Li, Y. *J. Phys. Chem. B* **2005**, *109*, 12544.

(290) Brolo, A. G.; Gordon, R.; Leathem, B.; Kavanagh, K. L. *Langmuir* **2004**, *20*, 4813.

(291) Yao, Z.; Zheng, M.; Ma, Li.; Shen, W. *Nanotechnology* **2008**, *19*, 2008.

(292) McFarland, A. D.; Young, M. A.; Dieringer, J. A.; Van Duyne, R. P. *J. Phys. Chem. B* **2005**, *109*, 11279.

(293) Jackson, J. B.; Halas, N. J.; *Proc. Natl. Acad. Sci. U.S.A.* **2004**, *101*, 17930.

(294) Wang, W.; Raun, C.; Gu, B. *Anal. Chim. Acta* **2006**, *567*, 121.

(295) Wang, W.; Gu, B. *Appl. Spectrosc*.**2005**, *12*, 1509.

(296) Moskovits, M. *J. Raman Spectrosc*. **2005**, *36*, 485.

(297) McCall, S.; Platzman, P.; Wolff, P. *Phys. Lett. A* **1980**, *77*, 381.

(298) Saikin, S.K.; Chu, Y.; Rappoport, D.; Crozier, K. B.; Guzik, A. A. *J. Phys. Chem. Lett*. **2010**, *1*, 2740.

(299) Zhao, L.; Jensen, L.; Schatz, G. C. *J. Am. Chem. Soc*. **2006**, *128*, 2911.

(300) Sun, M.; Liu, S.; Chen, M.; Xu, H. *J. Raman Spectrosc*. **2009**, *40*, 137.

(301) Jensen, L.; Zhao, L. L.; Schatz, G. C. *J. Phys. Chem. C* **2007**, *111*, 4756.
(302) Gilman, J. J. *The Art and science of growing crystals*; Wiley: New York, **1963**, 270.
(303) Brice, J. C. *J. Cryst. Growth* **1970**, *6*, 205.
(304) Billmann, J.; Kovacs, G.; Otto, A. *Surf. Sci*. **1980**, *92*, 153-173.
(305) Dick, L. A.; McFarland, A. D.; Haynes, C. L.; Van Duyne, R. P. *J. Phys. Chem. B* **2002**, *106*, 853-860.
(306) Vivoni, A.; Birke, R. L.; Foucault, R.; Lombardi, J. R. *J. Phys. Chem. B* **2003**, *107*, 5547-5557.
(307) Morton, S. M.; Jensen, L. *J. Am. Chem. Soc.* **2009**, *131*, 4090.
(308) Kneipp, K.; Kneipp, H.; Kneipp, J. *Acc. Chem. Rev.* **2006**, *39*, 443-450.
(309) Stewart, S.; Fredericks, P. M. *Spectrochim. Acta, Part A* **1999**, *55*, 1615-1640.
(310) Grabbe, E. S.; Buck, R. P. *J. Am. Chem. Soc.* **1989**, *111*, 8362-8366.
(311) Moskovits, M.; Suh, J. S. *J. Phys. Chem.* **1984**, *88*, 5526-5530.
(312) Moskovits, M. *Rev. Mod. Phys.* **1985**, *57*, 783-826.
(313) Kneipp, K. *Physics Today*. **2007**, *16*, 40-46.
(314) Camden, J. P.; Dieringer, J. A.; Zhao, J.; Van Duyne, R. P. *Accounts of Chemical Research.* **2008**, *41*, 12, 1653-1661.
(315) Ko, H.; Tsukruk, V. V. *Nano Lett.* **2006,** *6*, 1443-1448.
(316) Xia, Y.; Whitesides, G. M. *Annu. Rev. of Mater. Sci.* **1998**, *28*, 153-184.
(317) Ko, H.; Jiang, C.; Tsukruk, V. V. *Chem. Mater.* **2005**, *17*, 5489-5497. C. Jiang, S. Markutsya, H. Shulha, V. V. Tsukruk, *Adv. Mater.* **2005,** *17*, 1669-1673
(318) Muramatsu, H.; Dicks, J.M.; Tamiya, E.; Karube, I. *Anal. Chem.* **1987**, *59*, 2760-2763.
(319) Kharlampieva, E.; Kozlovskaya, V.; Chan, J.; Ankner, J. F.; Tsukruk, V. V. *Langmuir* ***2009***, *25*, 14017-14024.
(320) Tsukruk, V. V.; Bliznyuk, V. N. *Langmuir,* **1998,** *14*, 446.
(321) Jiang, C.; Markutsya, S.; Pikus, Y.; Tsukruk, V. V. *Nature Mater.* **2004,** *3*, 721-728.
(322) Jiang, C.; Markutsya, S.; Tsukruk, V. V. *Adv. Mater*. **2004,** *16*, 157-161.
(323) Jiang, C.; Markutsya, S.; Shulha, H.; Tsukruk, V. V. *Adv. Mater*. **2005**, *17*, 1669-1673.
(324) Jiang, C.; Tsukruk, V. V. *Soft Matter.* **2005**, *1*, 334-337.
(325) Van Hoonacker, A.; Englebienne, P. *Current Nanoscience*. **2006**, *2*, 359-371.
(326) Ghosh, S.K.; Pal, T. *Chem. Rev.* **2007**, *107*, 4797-4862.
(327) Jain, P. K.; El-Sayed, M. A. *Nano Lett*. **2007**, *7*, 2854-2858.
(328) Jiang, C.; Markutsya, S.; Tsukruk, V.V. *Langmuir* **2004**, *20*, 882-890.
(329) Wrosek, K.; Gramblicka, M.; Tothova, D.; Antosova, M.; Polakovic, M. *Chemical Papers* **2010**, *64*, 461-468.
(330) Han, W.; Mou, J.; Sheng, J.; Yang, J.; Shao, Z. *Biochemistry* **1995**, *34*, 8215-8220.
(331) San Paulo, A.; Garcia, R. *Biophysical Journal* **2000**, *78*, 1599-1605.
(332) Guss, B.; Leander, K.; Hellman, U.; Uhlén, M.; Sjöquist, J.; Lindberg, M. *Eur. J. Biochem.* **1985**, *153*, 579-585.

(333) Dou, X.; Yamaguchi, Y.; Yamamoto, H.; Doi, S.; Ozaki, Y. *J. Raman Spectrosc.* **1998**, *29*, 739-742.
(334) Chon, H.; Lim, C.; Ha, S. M.; Ahn, Y.; Lee, E. K.; Chang, S. I.; Seong, G. H.; Choo, J. *Anal. Chem.* **2010**, *82*, 5290-5295.
(335) Mahmoud, M. A.; El-Sayed, M. A. *J. Am. Chem. Soc.* **2010**, *132*, 12704-12710.
(336) Mahmoud, M. A.; Snyder, B.; El-Sayed, M. A. *J. Phys. Chem. C* **2010**, *114*, 7436-7443.
(337) Au, L.; Chen, Y.; Zhou, F.; Camargo, P. H. C.; Lim, B.; Li, Z.-Y.; Ginger, D. S.; Xia, Y. *Nano Res.* **2008**, *1*, 441-449.
(338) Mahmoud, M. A.; El-Sayed, M. A. *Nano Lett.* **2009**, *9*, 3025-3031.
(339) Horton, H.; Moran, L.; Ochs, R.; Rawn, J.; Scrimgeour, K. *Principles of Biochemistry*, Prentice Hall, **1996**.
(340) Witte, A. B.; Timmer, C. M.; Gam, J. J.; Choi, S. K.; Holl, M. M. B.; Orr, B. G.; Baker, J. R.; Sinniah, K. *Biomacromolecules* **2012**, *13*, 507-516.
(341) Hagen, J. A.; Kim, S. N.; Bayraktaroglu, B.; Leedy, K.; Chávez, J. L.; Kelley-Loughnane, N.; Naik, R. R.; Stone, M. O. *Sensors* **2011**, *11*, 6645-6655.
(342) Lisunova, M.; Mahmoud, M. A.; Holland, N.; Combs, Z. A.; El-Sayed, M. A.; Tsukruk, V. V. *J. Mater. Chem.* **2012**, *22*, 16745-16753.
(343) Palik, E. *Handbook of Optical Constants of Solids I – III* Elsiever Inc., USA **1997**.
(344) Rycenga, M.; Cobley, C. M.; Zeng, J.; Li, W.; Moran, C. H.; Zhang, Q.; Qin, D.; Xia, Y. *Chem. Rev.* **2011**, *111*, 3669-3712.
(345) Zhang, S.; Bao, K.; Halas, N. J.; Xu, H.; Nordlander, P. *Nano Lett.* **2011**, *11*, 1657-1663.
(346) Esteban, R.; Borisov, A. G.; Nordlander, P.; Aizpurua, J. *Nature Communications* **2012**, *3*, 825, DOI: 10.1038/ncomms1806.
(347) Liu, F.; Gu, H.; Qi, Y.; Dong, X.; Gao, J.; Cai, T. *Spectrochimica Acta Part A* **2012**, *85*, 111-119.
(348) Dendisová-Vyškovská, M.; Kokaislová, A.; Oncˇák, M.; Mateˇjka, P. *J. Mol. Struct.* **2013**, *1038*, 19-28.
(349) Le Ru, E. C.; Etchegoin, P. G. *MRS Bulletin* **2013**, *38*, 631-640.
(350) Halas, N. J.; Moskovits, M. *MRS Bulletin* **2013**, *38*, 607-611.

VITA

Zachary A. Combs

Zachary Allen Combs was born in Mills River, North Carolina on June 23, 1987 to Allen and Pamela Combs. He attended Mills River Elementary School, Rugby Middle School, and West Henderson High School where he graduated as Valedictorian in 2005. He earned his Bachelor of Science degree with honors in Polymer and Fiber Chemistry with a minor in Bioengineering from Clemson University where he graduated Summa Cum Laude in 2009. He pursued a Ph.D. in Materials Science and Engineering at Georgia Institute of Technology with Professor Vladimir V. Tsukruk. After graduating, Zachary will begin his career as a New Product Development Scientist at the Aditya Birla Carbon Group facility in Marietta, Georgia.